A Computational Characterization of Nanoscale Interactions of Biological Systems

by

Chloe Luyet

A dissertation submitted in partial fulfillment
of the requirements for the degree of
Doctor of Philosophy
(Chemical Engineering)
in The University of Michigan
2024

Doctoral Committee:

Professor Angela Violi, Chair
Associate Research Scientist Paolo Elvati
Professor Nicholas Kotov
Associate Professor J. Scott VanEpps
Professor Robert Ziff

Chloe Leigh Luyet

cluyet@umich.edu

ORCID iD: 0000-0002-1772-8618

For my loved ones (you know who you are)!

ACKNOWLEDGEMENTS

First and foremost, I would like to thank my advisor, Dr. Angela Violi, and my mentor, Dr. Paolo Elvati, for their constant support and validation. I have learned so much from the two of you, and I am forever grateful for the time and energy you've exhausted for me over the past four years, molding me into the inquisitive and always skeptical researcher I am today and intend to continue to emulate. I could not have asked to work for two people more understanding and respectful of my time and energy limits, a luxury not many Ph.D. students are fortunate to receive. Our relationship does not end here. To my committee members (Drs. Nicholas Kotov, Scott VanEpps, and Bob Ziff), thank you for taking the time to lend advice and diverse expertise for the success of this research. It was a pleasure to collaborate with Drs. Nicholas Kotov and Scott VanEpps on multiple projects over the course of my studies, which resulted in outstanding publications with Drs. Misché Hubbard and Yichun Wang. I would, also, like to express my gratitude to Susan Hamlin for her patience and for always being ready to calm my anxiety about deadlines and details via email, and Susan Montgomery for her kindness and encouragement.

Thank you, still, to my graduate school accomplices for helping me through difficult problems and for helping me learn how to better communicate my work. In particular, thank you to Anna Nelson, Jacob Saldinger, Misché Hubbard, Alex Adams, Samuel Young, Raymond Asare, and Matt Raymond for their friendship, collaboration, and emotional support. Special thanks to Dr. Changjiang Liu and Dr. Yichun Wang (Associate Professor at the University of Notre Dame) for welcoming me to the group and introducing me to the projects. Much of their research inspired my own. I'd also like to extend a shout-out to one

of the undergraduate students who worked with me, Jordan Vinh (perhaps, a future Ph.D.)! To all my pre-graduate school friends - Tayler Bruni, Ella Mucci, Zaina Azam (DDS), Nikki Legel, Amanda Noakes (PT), and Markiesha Baines (future MD), Aida Amini (PhD), and Ayad Nacy (PhD) - I love you guys so much!

My who-knows-how-many years of education have been blessed with the best teachers: Mrs. Wolf (4th grade, math), Mr. Arnould (6th grade, history), Ms. Miller (8th grade, English), Maestra Maturen (10-12th grade, Spanish), Mr. Perkins (11th grade, Chemistry), Mr. Blakeslee (11th grade, English), and Mr. Guinta (12th grade, Calculus). Each of you made me believe that I could do anything I put my mind to; you inspired my love of learning. I'd be remiss if I didn't also acknowledge a few of my Wayne State University professors. Dr. Plaumann, thank you for believing in me and advocating for me. Dr. Nikolla, thank you for being the best Kinetics instructor ever - you made the grad school level class a breeze - and for following my progress into grad school. Dr. Potoff, thank you for investing in me; that's honestly the best way to describe all you've done for me. You've gone above and beyond for me in so many ways. You have worn many hats in my life: teacher, mentor, research advisor, confidant, and dear friend.

Last, but certainly not least, I'd like to thank my family. No one understood why I wanted to do this, but you all supported me and you continued to support me throughout my graduate studies. To my parents, Leigh and Linda Luyet: There are no two people I owe more in my life than the two of you. Thank you for instilling in me the value of hard work and dedication. The apple doesn't fall far from the tree. To my siblings, Lauren and Matthew Luyet: Thank you for keeping life interesting and entertaining. You are my source of levity. To my partner in all things for the past 7 years, Dr. Mohammad Soroush Barhaghi: Thank you for lifting me up when I'm down and lifting me higher when I'm already up. I'm so lucky to have found someone who not only has similar passions, but who is, also, so kind. To my Aunt Leslie and Uncle Bob: Thank you for letting me live with you during the Winter of 2019 and for being my home away from home. To my grandparents, Fran and Gene Cislo:

Grandma, thank you for keeping me excited about what the future holds and for not only listening to me talk about my research, but also asking about it. Grandpa, thank you for telling me to live my life the way I want and to not care what anyone thinks. It meant a lot coming from you and, I think, you knew it would.

This project, and my ambition, would be nothing without the guidance of these wonderful people. Indubitably, I am the luckiest person on Earth to have so many wonderful people in my life. Here is written proof that this accomplishment is not mine, alone; it's shared, and just as much the fruitful efforts of all these wonderful people I mentioned as it is my own accomplishment.

TABLE OF CONTENTS

LIST OF FIGURES

Figure

LIST OF TABLES

Table

LIST OF APPENDICES

Appendix

LIST OF ABBREVIATIONS

CHL cholesterol

CL cardiolipin

CNPs carbon nanoparticles

DAG diacylglycerol

ECM extracellular matrix

eDNA extracellular DNA

ERG ergosterol

FA free fatty acid

HPLC high performance liquid chromatography

LPG lysophosphatidylglycerol

MD Molecular Dynamics

NPs nanoparticles

PG phosphatidylglycerol

PE phosphatidylethanolamine

PC phosphatidylcholine

PI phosphatidylinositol

PS phosphatidylserine

PSM sphingomyelin

PSMs phenol soluble modulins

ABSTRACT

Treatment of biofilm infections is difficult, in part, due to the bacteria's pathogenicity and, in part, due to biofilm's structural resilience. Not only does a drug have to traverse the extracellular matrix, but it also has to cross membranes to be delivered to the bacterial cell. Each pathway presents a unique set of challenges. In the extracellular matrix, drugs are inhibited by networks of functional amyloid fibers, among other things. At the cellular level, drug permeation has been linked to cell membrane vibrations, which inherently depend on the composition of the membrane. Nanoparticles are a promising route for controlling biofilm growth and preventing resistance because they offer a myriad of sizes, shapes, and functional groups. In this thesis, I use molecular dynamics simulations and novel analysis methods to computationally explore the nanoscale interactions of (1) proteins, (2) membranes, and (3) nanoparticles. I characterize the structure of staphylococcal PSMα1 amyloid nanofibers, identify membrane vibrations from both eukaryotic and prokaryotic organisms, and propose interactions of chiral carbon nanoparticles with teicoplanin and phenol-soluble modulins that could be responsible for their separation by high-performance liquid chromatography and anti-biofilm capabilities, respectively. The efforts of this research have increased our understanding of nanofibers through the development of *in-silico* models with atomistic resolution and have helped us to screen for potential nanoparticulate candidates that could serve as biofilm manipulators.

CHAPTER 1

Introduction

1.1 Motivation for this Research

For such small microorganisms, bacteria are causing *big* health problems. In 2014, 1 in 25 patients in United States hospitals contracted at least one bacterial infection[1]. Of these hospital-acquired infections, approximately 60% were associated with biofilm formation, and another 60% of these were attributed to methicillin-resistant *Staphylococcus aureus* (MRSA)[2]. MRSA kills more people in the U.S. each year than HIV/AIDS, emphysema, Parkinson's disease, and homicide, combined[3]. The implications of this work reach far beyond the clinical envelope. Biofilm flourishes in soil and leaches into the water supply. It is everywhere. Consequently, understanding the mechanisms by which biofilms derive resilience against treatment and their pathogenicity is essential to making progress in combating biofilm infections.

1.2 What is Biofilm?

Biofilms are colonies of unicellular bacteria that congregate into a multicellular network of bacteria. Bacteria in biofilm are enveloped in a highly impermeable extracellular matrix (ECM) of proteins, polysaccharides, and extracellular DNA (eDNA)[4]. The ECM, and nanostructures within the ECM, complicate anti-biofilm treatments and drug delivery. Like-

wise, biofilm formation has contributed to nearly a 1,000-fold increase in drug tolerance than the same bacterium would have unicellularly[5], among other factors, like reduced cell metabolism and small molecule degrading enzymes that reduce the efficacy of the drug. Even if a drug is able to elude the ECM, it has to, then, permeate cellular membranes to be delivered to the appropriate target inside the cell.

1.3 Combating Biofilm at the Extracellular Level

1.3.1 What are Phenol Soluble Modulins (PSMs)?

As it turns out, phenol soluble modulins (PSMs) are amphipathic proteins that significantly contribute to *both* the resilience and pathogenicity of *S. aureus*, depending on their state of aggregation[4,6–11]. There are seven PSMs, categorized by where they are encoded in the *S. aureus* genome[12]. There are four α-PSMs (*i.e.*, PSMα1-4), two β-PSMs (*i.e.*, PSMβ1-2), and the δ-toxin[13]. *S. aureus* uses a specialized exportation system to export PSMs from the cytoplasm because the monomeric peptides are toxic virulence factors that not only attack host membranes, but also exhibit antimicrobial/anti-biofilm activity[6–9,11]. It has been observed that small clusters of the peptides (oligomers) are even more toxic than their monomeric counterparts[14], which is a typical trend of bacterial toxins, like the *S. aureus* α-toxin[8,15].

1.3.2 What are Functional Amyloid Fibers?

While the toxicity of monomeric PSMs is indisputable, some PSMs (PSMα1 and PSMα4) in the ECM have the tendency to adopt another configuration, with a corresponding function that is not unequivocally pathogenic: They aggregate into fibers, called functional amyloids[7,16–19]. It should be noted that functional amyloid fibers are not unique to *S. aureus* biofilms and form from the aggregation of other proteinaceous subunits in many other bacterial species; however, Figure 1.1 provides visualization for the hierarchical position of

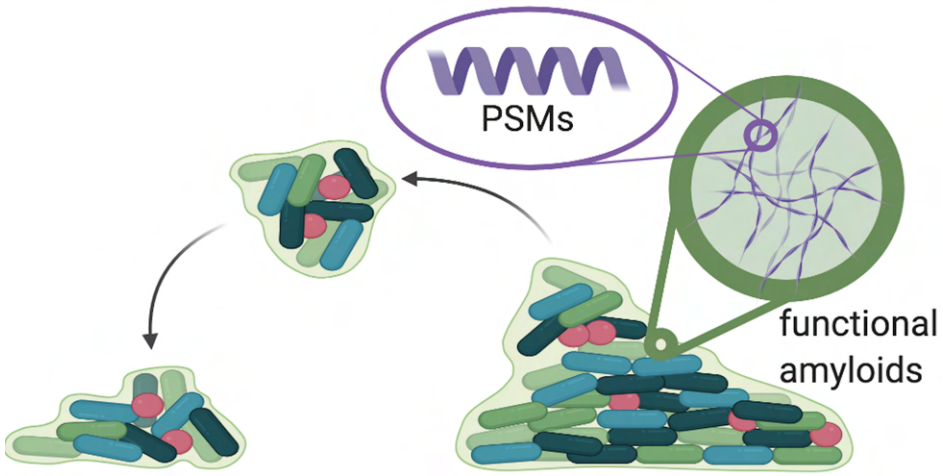

Figure 1.1: PSM-Derived Functional Amyloid Demonstration in biofilm extracellular matrix. Image created using BioRender.

PSM aggregates in biofilm. In *in-vitro* biofilm cultures, PSM aggregation is bolstered by the presence of extracellular DNA (eDNA); however, in acellular aqueous solutions, they self-assemble at high concentrations, without any external direction, promotion, or catalytic induction[4,9,11,20]. The spontaneity with which the fibers form in water demonstrates that their formation is thermodynamically favorable[16,21].

From previous studies, we know with great certainty that the amyloid fibers formed from PSMα1 and PSMα4 have a characteristic cross-β structure[1,11,18,22]. This cross-β structure has parallel β-sheet strands that run perpendicular to the cross-section of the fiber axis, and formation is driven by hydrogen bonding, hydrophobic interactions, and steric zippers[18,23]. The β-sheet strands associate into protofilaments, which can associate laterally[21,22]. In regard to biological function, it appears that PSM functional amyloids seem to resist antimicrobial drugs and promote biofilm stability by preventing ECM disassembly from enzymes and mechanical stress[11,18]. Importantly, PSM amyloids are present in human *S. aureus* infections[24–27]. They are, therefore, a critical target for anti-biofilm compounds and should be studied further.

1.3.3 What has this Thesis Uncovered and How?

My research has discovered that the chirality of fibers is a determinant of their lateral aggregation and that model fibers adopt a helicity representative of experimental fibers that form in solution[28], evidence that molecular dynamics simulations are a useful tool in the study of protein aggregation. This was accomplished through Molecular Dynamics (MD) simulations, which provided a level of detail that is not available from experiments. For example, an experimental study on the amyloids formed in Alzheimer's disease used six different techniques to acquire an atomistic resolution structure[22]. As has been successfully demonstrated by publications in this field[29], publications characterizing other amyloid fibers[7,30], and the research results in this thesis, using computational simulations can significantly expedite the process of investigation and lead to interesting, informative results.

1.4 Combating Biofilm at the Cellular Level

1.4.1 What are Cell Membranes?

In biofilm, extracellular functional amyloid fibers are anchored to cell (or plasma) membranes, which are lipid bilayers that envelop the cell's cytoplasm. Cell membranes act as barriers that separate the cytoplasm of the cell from its extracellular environment, and all molecules imported or exported from the cell must traverse its lipid bilayer. To complicate matters, Gram-negative bacterial cells have two cell membranes. Thus, cell membranes are an important factor to consider in drug delivery because, ultimately, in order to deliver a drug to its target inside a cell, the drug will have to permeate at least one membrane, often more. Furthermore, amyloid fibers and cell membranes vibrate, as do all animate and inanimate things. In the case of cell membranes, there exists a link between membranes' vibrations and the transport of small molecules across membranes[31–34].

1.4.2 Why are Membrane Vibrations Important?

The internal motions of biological membranes provide a connection between membrane composition and many biological processes[35], including membrane permeability. Not only do membrane vibrations influence membrane permeability, but, because membranes have different compositions, membrane vibrations are also unique, bacterium-specific tags. Cellular membranes' lipid composition, asymmetry, and membrane-adjacent structures (*e.g.*, anchored functional amyloids) are all factors that contribute to the unique nature of cellular membranes and subsequent colonies, which is why cellular membrane vibrations have long been suggested as a means of distinguishing among microorganisms[36]. In fact, this approach has been used in the identification of amyloid-induced diseases (*e.g.*, Alzheimer's[37]).

1.4.3 What has this Thesis Uncovered and How?

My research uses the Kolmogrov-Smirnov statistic to quantitatively distinguish among unique low-THz vibrational spectra for mammalian and bacterial membranes, demonstrating that vibrational spectra could be used in the identification of different organisms[38]. Our method can easily be extended to fingerprint other biological structures (*e.g.*, amyloid fibers, polysaccharides, and protein-ligand structures). This was accomplished using MD simulations, advanced statistical analyses, and graph theory.

1.5 Combating Biofilm with Carbon Nanoparticles (CNPs)

1.5.1 What are Carbon Nanoparticles?

We have, now, reported the critical role that amyloid fibers play in the virulence of biofilms, as well as the intricacies of membrane dynamics and permeation. To discover how to disrupt or manipulate biofilm would be a major development in the quest to curb the consequences of biofilm pathogenicity. Promisingly, nanoparticles (NPs) have been shown to have antimicrobial properties, both at the extracellular level[39–42] and the cellular level[43–45].

Of particular interest for their anti-biofilm properties are carbon nanoparticles (CNPs) because they have demonstrated relatively higher biocompatibility, as compared to other NPs[41,46,47]. There are many ways to design CNPs to have different charges, functional groups, sizes, *etc.*. Investigating how these properties impact fiber formation would allow us to tune these properties to achieve maximal dispersal of biofilms. Because of the diversity of CNP compounds, studies have suggested that using CNPs in the rational design of new treatments will withstand the threat of antibiotic resistance[48], and offer a more tailored approach to treating different diseases.

1.5.2 What about Chirality Makes it an Important Property in the Design of Carbon Nanoparticles?

One property we can tune, in conjunction with the functional group of the CNP, is the functional group's chirality and, by extension, the chirality of the nanoparticle. Chiral antibiotics hold substantial promise when combating proteins and other macromolecules possessing intrinsic chirality due to their targeted and selective interaction[49,50]. In the intricate landscape of biochemistry, the three-dimensional structure and handedness of macromolecules play a pivotal role in their functions. Chirality in these biomolecules affects their specific interactions and binding with other molecules, influencing their overall biological activity. For example, there appears to be a generally hierarchical nature to the chirality of the building blocks of macromolecules into higher order structures[51].

Given this, chiral antibiotics, designed with a specific handedness, could potentially exhibit selective interactions with these chiral macromolecules. By aligning with the complementary geometry and chirality of target biomolecules, chiral antibiotics could disrupt their functions or pathways, potentially inhibiting or altering their activity.

In fact, chiral CNPs have demonstrated their potential in interfering with the self-assembly process of biomolecules within the ECM[52,53]. These nanoparticles have been observed to interact selectively with amyloid peptides[54], potentially leading to the dispersal of

biofilms. Moreover, their resistance to degradation and significant molecular weight counteracts the limitations of current anti-biofilm platforms, making them a promising candidate for combating bacterial biofilms[39]. The unique property of chirality in CNPs represents a promising avenue in combating biofilms, especially in targeting the intricate structure of ECM components and amyloid-rich peptides crucial in biofilm formation.

1.5.3 What has this Thesis Uncovered and How?

My research shows that the chirality of CNP functional groups plays an important role in interactions with nanosystems, including PSMs, and can be enantiomerically separated due to a difference in affinity of the teicoplanin stationary phase in an high performance liquid chromatography (HPLC) column.[55] This was accomplished using a combination of well-tempered Metadynamics molecular dynamics simulations, unbiased MD simulations, and data analysis with Python.

CHAPTER 2

Methodology

2.1 Molecular Dynamics Simulations

2.1.1 Molecular Dynamics Simulations of PSMα1 Fibers

The initial structure was constructed from the PSMα1 IIKVIK segment crystal structure reported in Salinas *et al.* (6FG4); IIKVIK segments were replaced with the complete PSMα1 sequence (5KHB). These structures have Class 1 steric zippers, as reported in Salinas *et al.*. All simulations were performed with a combination of Nanoscale Molecular Dynamics (NAMD)[56,57] and PLUMED[58,59] software, using explicit TIP3P water[60] and the all-atom force field CHARMM, version 36[61]. A time step of 1 fs or 2 fs was employed to integrate the equations of motion and hydrogen atoms are kept rigid via the SHAKE algorithm. Non-bonded short-range interactions smoothly approached 0 using an X-PLOR switching function between 1 nm and 1.2 nm, in conjunction with the particle mesh Ewald algorithm, to evaluate long-range Coulombic forces. A Langevin thermostat, with a time constant of 1 ps, was used to keep the temperature constant at 310 K. The systems were minimized for 1000 steps before the equilibration runs and equilibrated using a PLUMED harmonic restraint between peptides. Equilibration simulations were performed, first, in the canonical ensemble with and without restraints, during which time the harmonic restraints between peptides were gradually set to zero, followed by simulations in the anisotropic isothermal-isobaric (NPT)

ensemble. Finally, unrestrained β-sheet nanofibers were run in the canonical ensemble until the root mean squared deviation of the nanofibers plateaued for at least 40 ns, at least 5 ns for α-helical sheet fibers, and 1 ns for fibers in vacuum (see Appendix A for a summary of RMSDs for converged simulations, Figures A.8 through A.11). Although previous studies have confirmed that PSMα1 nanofibers are composed of parallel β-sheets[18,19] and our results also confirm this (Figure 3.2h), we ran two antiparallel, 40-peptide-long, single protofilament systems (one with Class 7 steric zipper and one antiparallel Class 1 steric zipper)[62] for the sake of thoroughness; however, the systems we tested show unstable structures, prone to fragmentation. Visual Molecular Dynamics[63] and the MDAnalysis[64] Python library were used for visualization and data analysis, respectively. For the *in vacuo* simulations, the N- and C-termini and charged amino acid groups (*i.e.*, LYS and GLU) were neutralized by adding or removing proton atoms. Simulations of nanofibers with a chirality (Flipped and Mirror) different from the one spontaneously assumed during simulation (Reference), were prepared in two ways: (1) inverting the chirality of the nanofiber but leaving the chirality of each peptide untouched (Flipped), and (2) taking the mirror image of the nanofiber, such that the nanofiber chirality and the chirality of each peptide are inverted (Mirror). These simulations were generated from the configuration equilibrated as described above; however, after the chirality was changed, an additional NPT relaxation was performed by applying harmonic constraints that restrained the alpha carbons and hydrogens that were gradually tapered off over 15 ns.

2.1.2 Molecular Dynamics Simulations of Membranes in Vibrations Study

All the systems were prepared using the Membrane Builder in CHARMM GUI[65] and, then, post-processed when cropped systems were needed. Nanoscale Molecular Dynamics[56] software was used to perform Molecular Dynamics simulations, and a time step of 2 fs was employed to integrate the equations of motion, while hydrogen atoms were kept rigid via the SHAKE algorithm. Membranes were fully solvated in a 0.15 M NaCl solution using TIP3P

for water[60] and CHARMM, version 36[61], to model atomic interactions. Non-bonded short-range interactions smoothly approached 0 using an X-PLOR switching function between 1 nm and 1.2 nm, in conjunction with the particle mesh Ewald algorithm, to evaluate long-range Coulomb forces.

The systems were equilibrated using constrained canonical simulations, followed by isothermal-isobaric ensemble simulations with vanishing restraint, as per CHARMM GUI protocol. This preliminary equilibration was followed by 100 ns simulation in an NPsT ensemble, an isothermal-isobaric ensemble where changes in dimensions in the direction of the membrane's plane are coupled. Starting from the equilibrated systems, spectra were computed from 50 ns microcanonical ensemble simulations, while Langmuir isotherms were computed from canonical simulations 20 ns long. In all cases, the temperature was kept constant at 310 K by using a Langevin thermostat with a period of 1 ps, and pressure was imposed by using a Nosé-Hoover Langevin piston method, with a period of 200 fs and 50 fs decay. Processing and preparation of trajectories and structures were performed with the help of Visual Molecular Dynamics (VMD) software[63], as well as the MDAnalysis and Scipy Python libraries[64,66,67].

2.1.3 Molecular Dynamics Simulations of Teicoplanin-CNP Interactions

Using the CHARMM force field, version 36, and explicit TIP3P water, biased all-atom simulations were performed to compute the affinity of *L*- and *D*-CNPs with teicoplanin .[60,61] The systems were first minimized and equilibrated in the isothermal-isobaric ensemble for at least 150 ns, employing a Langevin piston Nose-Hoover method to maintain a pressure of 100 kPa and a Langevin thermostat to keep the temperature constant. A time step of 2 fs was used to integrate the equations of motion, and non-bonded short-range interactions were smoothly approached 0 using an X-PLOR switching function between 1 and 1.2 nm, in conjunction with the particle mesh Ewald algorithm to evaluate long-range Coulombic forces. The simulations were run using Nanoscale Molecular Dynamics (NAMD) software.[56]

Free energy surfaces were reconstructed using well-tempered Metadynamics simulations in the canonical ensemble over 630 ns or more, using Gaussian-shaped bias with a pace of 0.4 ps and a bias factor of 10.[68,69] The simulations were biased on the distance between teicoplanin's center of mass and the center of mass of each chiral CNP, and a harmonic wall was placed at 5 nm. The free energy was calculated as the average probability difference between the bound state (distance ≤ 2.5 nm) and the unbound state (distance ≥ 3 nm). The simulations were performed using PLUMED 2[58,59], and data visualization was done using Visual Molecular Dynamics (VMD)[63], while data analysis and plotting were performed using the MDAnalysis and Matplotlib Python libraries.[64,67,70]

2.1.4 Molecular Dynamics Simulations of PSM-CNP Interaction

All-atom forces were computed using CHARMM, version 36[61], and TIP3P water[60]. Nanoscale Molecular Dynamics software was used for running the simulations[56]. First, systems were minimized and then equilibrated in the isothermal-isobaric ensemble until the root-mean-square deviation of the aggregate converged (between 60 and 200 ns). A global system pressure of 100 kPa was maintained using a Langevin piston Nose-Hoover method (with a period of 200 fs and 50 fs decay)[71,72], and a Langevin thermostat[73] (with a characteristic time of 5 ps) was used to keep the system temperature at 300 K. A time step of 2 fs was employed to integrate the equations of motion, and all hydrogen bonds were kept rigid via the SHAKE algorithm[74]. Non-bonded short-range interactions smoothly approached 0 using an X-PLOR switching function[75] between 1 nm and the cutoff (1.2 nm), while long-range Coulombic forces were included using the particle mesh Ewald method[76] (with a tolerance of $1e-5$).

2.2 PSMα1 Fiber Simulation Post-Processing

The diameter was computed by (1) determining the nanofiber direction (*i.e.*, nanofiber main axis), (2) dividing the nanofiber with planes perpendicular to the nanofiber axis (*i.e.*,

slices), (3) dividing each slice in an even number of equal sectors, and (4) using the distance of the farthest atom from the nanofiber's axis of opposite sectors to sample the diameter. The nanofiber axis (step 1) was determined by linear regression of atomic spatial coordinates. Then, the atoms were grouped in wedges (steps 2 and 3) by using slices that are 1-4 nm wide and 8-20 sectors (each sector wedge covers 18° to 45° on the plane), where the selected parameters for each nanofiber (*i.e.*, slice height and number of sectors) are different, depending on which combination yielded the smallest standard deviation. Slice height and number of sector parameters do not impact the final diameter distribution, as demonstrated in Figure A.4. To minimize edge effects, we discarded any slice that did not have at least one atom in each sector. The final diameter distribution is obtained by collecting the sum of the distances of the atoms that were farthest from the nanofiber axis in opposite sectors.

The periodicity of the PSMα1 helical structure was determined from the average layer-to-layer angle and average layer-to-layer distance projected along the nanofiber axis, determined by linear regression of all atomic coordinates. For each layer (see Figure 3.1), first the center of mass and the principal axes of inertia were computed, followed by the layer-to-layer distance (*i.e.*, distance between the center of mass of consecutive layers) and by the layer-to-layer angle (dihedral angle from the largest principal axis of each layer and the center of mass of two consecutive layers).

In Chapter 3, we report the results obtained for the longest simulated fiber in each class, while data of shorter fibers were used to test the convergence of the results, as they generally show a somewhat monotonic trend with aggregate length. This effect becomes small when at least 20 layers are present, even for the quantities that have the strongest dependence from the nanofiber length (see Figures A.5 and A.6).

2.3 TEM image processing

The nanofiber diameter distribution from TEM data was obtained with in-house code. The images were processed using kernel filtering to determine the direction of the nanofiber

in the frame of the image; we used 180 100×100 kernels for an angular resolution of 1° after filtering the images to maximize the contrast between the edges and center of the nanofibers. Then, we searched each filtered image in the direction perpendicular to the applied filter angle and estimated the diameter from the distance between two consecutive high-contrast peaks.

2.4 AFM image processing

The nanofiber periodicity and diameter distribution from AFM data was obtained with in-house code. The periodicity of the PSMα1 structure was determined from AFM images by computing the distance between the highest-intensity nanofiber peaks. The AFM images were initially split into multiple images, each containing a single nanofiber, to obtain relatively consistent intensity ranges. The highest point in the nanofibers was, then, identified using the Otsu threshold method, and the distance between the center of closest peaks was collected. As the distance is dependent upon the Otsu threshold parameter, which in turn depends on the intensity of the pixel, the threshold parameter for each image was determined to be the value, between 1.1 and 3.1, that minimizes the standard deviation for the values of the distances between the regions of highest intensity. Diameters were obtained by first segmenting images in order to separate the fiber from the background. 3000 to 5000 points in the fiber were then randomly chosen and, for each of them, the diameter was set equal to the shortest distance to opposite edges, which was found by sampling all the directions with a 1° resolution.

2.5 Vibration Spectra

Absorption cross-section α_{cs} as a function of the frequency ω were calculated from trajectories, using the relation:

$$\alpha_{cs}(\omega) = \frac{4\pi^2}{3\hbar c\epsilon n(\omega)}\omega(1 - e^{-\beta\hbar\omega})Q(\omega)I_{cl}(\omega) \tag{2.1}$$

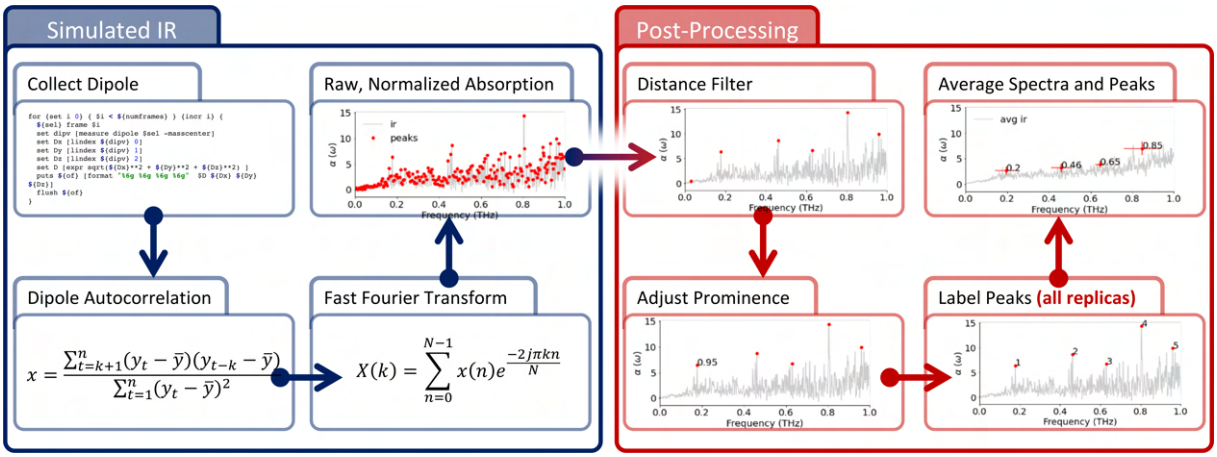

Figure 2.1: Spectra Calculation and Signal Analysis. Infrared spectra are computed from MD trajectories (blue panel) and, then, post-processed to find local maxima. Spectra are computed from MD trajectories as Fourier transform of the membrane total dipole autocorrelation; then, the spectra are normalized before peaks are identified using a distance and prominence filter (Figures B.3 through B.6). For more details, see the Methodology Section.

where $\hbar$ is the reduced Plank constant, c is the speed of light in vacuum, ϵ the vacuum permittivity, $n(\omega)$ the refractive index of the solution, $\beta(= 1/k_B T)$ is the inverse of the Boltzmann constant times the temperature, $Q(\omega)$ is the harmonic quantum correction[77],

$$Q_{harm}(\omega) = \frac{\beta\hbar\omega}{1 - e^{-\beta\hbar\omega}} \tag{2.2}$$

and $I_{cl}(\omega)$ is the classical spectral density,

$$I_{cl}(\omega) = \frac{1}{2\pi} \int_{-\infty}^{\infty} dt\, e^{-i\omega t} \langle \boldsymbol{M}(0)\boldsymbol{M}(t) \rangle \tag{2.3}$$

where angular brackets indicate ensemble averaging and $\boldsymbol{M}$ is the membrane's total dipole moment. For practical reasons, we assumed $n(\omega) = 1$ as, in this range, the correction is almost linear[78]. Finally, numerical noise was reduced by using Blackman windowing when computing the Fourier transform and by applying a Savitsky-Golay filter (polynomial order of 6 over 21 windows, Figure B.1) on $\alpha_{cs}(\omega)$.

Since different membranes are represented by periodic systems of different sizes, to compare different spectra and obtain size-independent quantities, we divided each spectrum by the average value of the signal in our interval

$$N = \int d\omega \; \alpha_{cs}(\omega) \tag{2.4}$$

and used $\alpha(\omega) = \alpha_{cs}(\omega)/N$ in all the comparisons.

2.6 Signal Analysis

Peaks were identified from the spectra by tuning the (1) prominence (vertical distance between the peak and its lowest contour line) and the (2) minimum distance between peaks. Prominence, alone, is not used as a peak-finding metric because doing so would only select the highest-intensity peaks, which are located on the right side of the spectra in this case. Instead, after setting the minimum peak-to-peak distance (125 GHz for the rat liver cells, and 142 GHz for bacterial membranes), we computed the prominence distribution for different prominence thresholds. A demonstration of how prominence and distance between peaks are tuned is available in the Appendix B (Figure B.3 through Figure B.6). We then identified the range of values that were closer to the average number of peaks (computed over all the prominence values) and selected the highest value. For each membrane, we compute the average frequency and intensity of each peak using the peaks computed over replicas (3 replicas for $S476^{A}_{51}$, $S476_{33}$, *B. Subtilis*, and rat liver; 4 replicas for $S476^{A}_{33}$, see a more detailed discussion in the Results section).

To quantify the similarity between two spectra, we used a two-sample Kolmogorov-Smirnov (KS) test [79]. As replicas of the same membrane are (or should be, see the discussion in the results) statistically equivalent, variation between replicas of the same system can be assumed to originate from the computational method. As such, when comparing different membranes, we used the mean KS (and the corresponding standard error) of the replicas of a

membrane as a baseline for the comparison with other systems. Of note, all the comparisons were performed by computing the KS value for all the possible pairs of replicas of one system with another, and not by comparing the average spectra.

2.7 Root-Mean-Squared Fluctuations (RMSF)

RMSF, that is the mean deviation from the average position of an atom, was calculated from the microcanonical simulations, using the Python MDAnalysis module[64,67]. Due to a systematic numerical bias in the RMSF value for molecules that are close to the periodic boundaries, all the contributions from these molecules were removed. To allow a meaningful comparison with other membranes, we only computed the RMSF of the atoms that are not part of sterol molecules.

2.8 Hydrogen Bond Lifetimes

Hydrogen bond lifetimes were calculated using MDAnalysis[67], where (1) tau_max (input trajectory time over which to search for a hydrogen bond) was set to 5 ns, (2) intermittency (max number of frames a hydrogen bond can be broken and still count as present if it is still observed in the following frame) was set to 1, and the default values of 0.3 nm and 150 degrees were used for both the (3) d_h_cutoff (hydrogen bond distance) and (4) d_h_a_cutoff (hydrogen bond angle), respectively.

CHAPTER 3

Combating Biofilm at the Extracellular Level

3.1 PSMα1 Fibers

3.1.1 Introduction

Bacterial biofilms are communities of single or multiple species of microorganisms, attached to a surface and organized into a complex three-dimensional structure[80]. To form a functional structure, biofilm cells produce polymers that constitute the extracellular matrix (ECM), which facilitates binding between cells and to the surface. The most extensively studied components of biofilm ECM are polysaccharides, nucleic acids, and proteins[81,82], but the relative amounts of these compounds vary depending on the species[83,84]. Some of the protein components in the ECM are peptides that can self-aggregate to form nanoscale amyloid fibrils.

Unlike in human diseases (*e.g.*, Parkinson's and Alzheimer's), where amyloid formation represents damage or misfolding of peptides[85], many of these bacterial amyloids are

The information in this chapter is available in the following cited publication. Paolo Elvati, Chloe Luyet, YichunWang, Changjiang Liu, J Scott VanEpps, Nicholas A Kotov, and Angela Violi. Molecular architecture and helicity of bacterial amyloid nanofibers: Implications for the design of nanoscale antibiotics. ACS Applied Nano Materials, 6:6594–6604, 2023. Experimental methodologies performed by Yichun Wang have been omitted; however, in-text references to experiments performed by Yichun Wang are denoted appropriately.

functional, in that they contribute to physiological activities: aggregation of toxic peptides modulates their activity, or they can operate as a physical barrier in biofilms, increasing resilience and resistance to antimicrobial drugs and immune mediators[86–91]. The presence of these nanofibers is extremely common in bacterial biofilms. They have been identified in *Chloroflexi, Actinobacteria, Bacteroidetes, Firmicutes*, and *Proteobacteria*[92]. Within the Firmicutes phylum, *S. aureus* is a well-known pathogenic, Gram-positive bacterium that generates extensive biofilm structures. In the United States, infections associated with *S. aureus* have an estimated mortality rate of 25% (higher in the case of drug-resistant strains), causing a high number of hospitalizations and significant medical costs[93]. Mortality caused by methicillin-resistant *S. aureus* (MRSA) remains the highest for any antibiotic-resistant pathogen, reported by the CDC to be at ∼20,000 in 2018[94], exacerbated by the COVID-19 pandemic due to bacterial superinfections[95].

Staphylococcal species possess a specific set of peptides known as phenol soluble modulins (PSMs) that serve as key virulence factors, stimulate inflammatory responses, alter the host cell cycle and lyse human cells. Remarkably, PSMs can also self-assemble into highly-ordered amyloid structures, which may contribute to the establishment, integrity, and maturation of the biofilm.[17,96,97]. PSMs, α-helical amphiphatic peptides, are classified depending on their length. The smallest peptides (21 amino acids in length) are α-type, PSMα1-4 and δ-toxin. The longer peptides, which are 44 amino acids in length, are PSMβ1 and PSMβ2. Despite their sequence similarity, not all PSMs form ordered amyloid structures and not all of them follow the same structural motifs. As such, PSMα3, the most toxic member, forms cross-α nanofibrils[20,98–100], while PSMα1 and PSMα4 form canonical cross-β amyloid nanofibers. These functional amyloids are known for their stability, which is attributed to their cross-β structure, β-sheet strands that run parallel to the nanofiber axis and peptide pairs that aggregate perpendicular to the nanofiber axis[18,19,82,86,90,101–103].

To date, open questions remain about the formation and characteristics of PSM-derived amyloid nanofibers. Some studies have identified the crystal structures of functional amyloids

reporting a consistent nanofiber diameter of approximately 10-12 nm[1,11,21,104], but a specific reason for the fibers' lateral growth mechanism has not been deciphered. Similarly, the chirality and helical structure of the nanofibers remains an open question[18,19]. From an experimental perspective, a critical issue is that large insoluble biological complexes, like PSM nanofibers, reaching microns in length[21,22], are difficult to crystallize[23]. Moreover, structures obtained from crystals are not necessarily accurate representations of the nanofibers in dispersion, as the conditions that promote crystallization may differ substantially from typical *in vivo* and *in vitro* experimental environments, and even in solution. The formation of amyloid nanofibers is a relatively slow process that can take a few days *in vitro*[4,11] to a week or more in solution[1,19]. Most aspects of this transition are still unclear and are further complicated *in vitro* by the interactions with other bio-macromolecules present in the ECM, like extracellular DNA[4] and other peptides (*e.g.*, the *N*-terminus of the quorum sensing signal peptide AgrD)[105,106]. The slow and gradual transition from single peptide to amyloid nanofibers suggests a process that involves configurational and conformational transformations with several relatively stable intermediates, which are unlikely to be captured by crystallographic experiments[7]. Finally, the presence of randomly-coiled, amorphous-like regions at the interface of nanofibers and water and between fibers further support the importance of molecular simulations, as rigid crystal structures would fail to capture the entropic and imperfect features of disordered regions of otherwise highly-ordered nanofibers[107]. After all, amorphous aggregates are a ubiquitous facet in the formation of amyloid nanofibers, characteristic of those in Alzheimer's disease[19,108,109], Parkinson's disease, prion misfolding[110], and *E. coli* curli[111–113], to name a few. Consequently, other amyloid nanofibers should be subject to similar scrutiny by MD simulations of different types[30,107,114].

There is, therefore, a clear need to gain additional insights on the structures of PSM functional amyloid nanofibers. In the present study, we report on the molecular structure of PSMα1 nanofibers and their characteristics, such as diameter, chirality and periodicity, and advance hypotheses on the role of chirality on the mechanisms of nanofiber assembly.

Leveraging a combination of fully-atomistic molecular dynamics (MD) simulations and experimental data obtained via mass spectroscopy and microscopy techniques, we probe the characteristics of several *in silico* candidate structures for the amyloid nanofibers. We find compelling evidence that a cross-β-sheet two-protofilament (2β) structure is the most plausible structural model for PSMα1 nanofibers in solution, that matches the experimental values of chirality, diameter, and helical periodicity (pitch) of mature PSMα1 nanofibers in solution. The 2β PSMα1 amyloid nanofiber model can be used to study nanofiber-antimicrobial interactions to elucidate a mechanism for biofilm manipulation, using man-made anti-amyloid biomimetic nanostructures[39,46]. In addition to machine learning techniques recently developed by our team[115], this study provides a structural understanding of amyloid fibers that can inform a set of MD-based design principles, and can usher in an era of tailor-made NPs as nanobiotics and high-efficacy antibacterial agents.

3.1.2 Results and Discussion

3.1.2.1 Nanofiber Formation and Evolution

Confounding factors (*e.g.*, extracellular DNA) complicate the analysis of PSMα1 aggregates when formed in *in vitro* biofilm cultures. For this reason, we chose to study the formation of amyloid nanofibers from PSMα1 aqueous solution in this work. Even without any external direction, promotion, or catalytic induction, PSMα1 self-assembles into amyloid nanofibers at high concentrations[4,9,11,20]. Similar to results reported in the literature[4,11,18,39], PSMα1 nanofibers are detected as early as day 4, *via* β-sheets signal in circular dichroism (CD) spectroscopy, and visualized at day 9 *via* transmission electron microscopy (TEM). Both CD spectra and TEM images are performed by experimental collaborator, Yichun Wang, and results can be seen in the supplementary information of the cited paper[28]. The formation of a consistent nanofiber took longer than previously reported, with changes in both the CD spectra and TEM images. The CD spectra taken for samples older than 14 days are characterized by strong β-sheets and disordered structures signals, while diameters

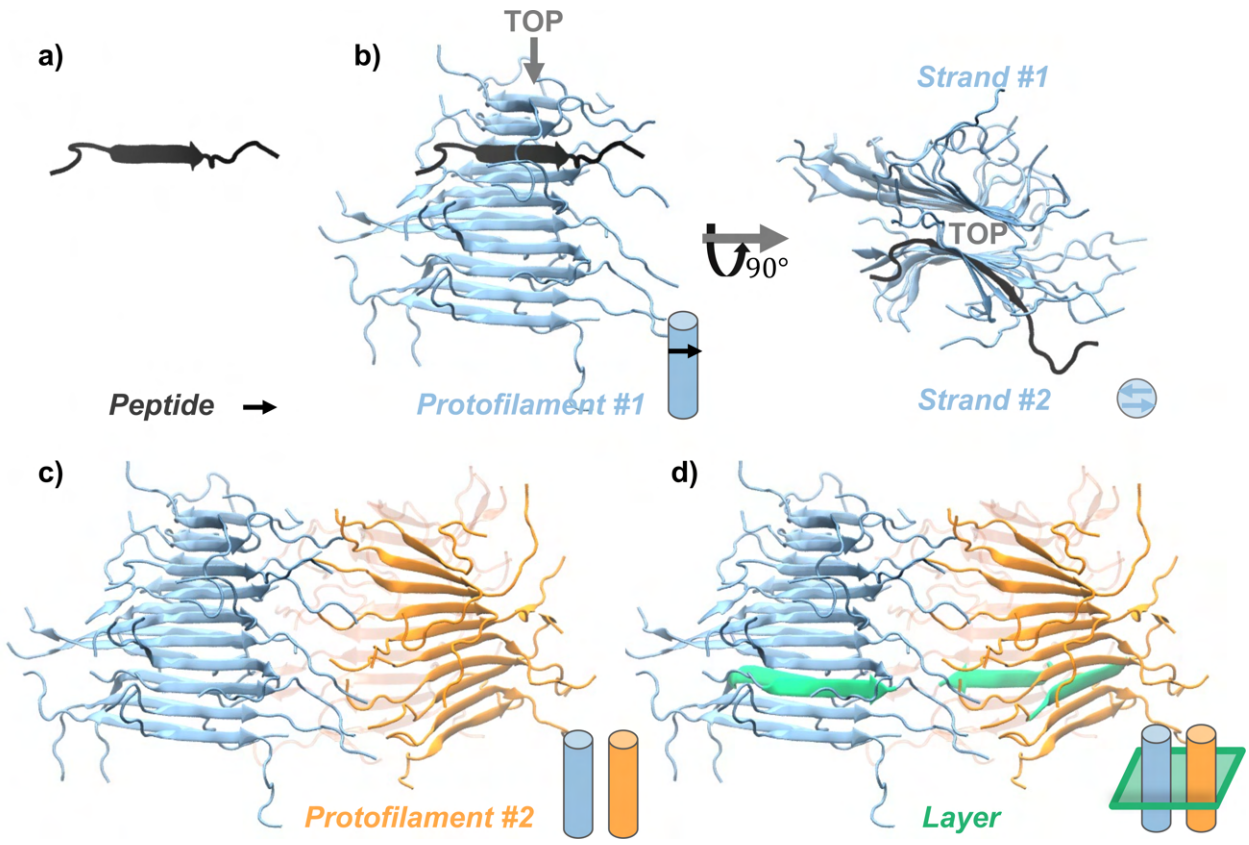

Figure 3.1: **Computational Models' Nomenclature for a 2β Nanofiber**, with colors and text illustrating the terminology and labels used in this work. (a) Individual PSMα1 peptides (black) form (b, right) long parallel β-strands that pair to form (b, left) protofilaments (blue). Protofilaments can, then, laterally aggregate to form (c) multi-protofilament nanofibers. When computing properties, it is convenient to define a (d) layer (green), which is composed of PSMα1 from different strands and different protofilaments, approximately on a plane perpendicular to the nanofiber axis of elongation. The first character in each nanofiber name (1, 2, 3) represents the number of protofilaments in the structure; the second term (α or β) describes the main structural motif of each peptide molecule within the nanofiber. For a demonstration of the α-helical sheet motif, see Fig. A.12.

measured from TEM images show a significant decrease in the standard error of the mean diameters (Fig. A.1 and Tab. A.1) for samples taken at day 21 and later.

The mature PSMα1 amyloid nanofibers are stable when subjected to thermal and mechanical (*i.e.*, sonication) stress (see Methodology for details), with no discernible change in TEM morphology following these treatments (see SI of cited paper[28]). This stability, however, is not the result of a polymerization mechanism, in which covalent bonds are formed between peptides, since mass spectroscopy never detects the presence of anything but individual PSMα1 peptides (see SI of cited paper[28]), and the nanofibers can be dissolved with hexafluoroisopropanol (HFIP) and trifluoroacetic acid (TFA) (Fig. 3.2g).

Based on these data and the information available in existing literature, we selected six classes of deformylated-PSMα1 aggregates as plausible candidates for the amyloid nanofibers or their precursors (see Tab. 3.1). Namely, we simulated aggregates formed by one, two, or three laterally-aggregated protofilaments of PSMα1 in either α-helical or parallel[18,19] β-sheet configuration (Fig. 3.1 for clarifications regarding terminology), and estimated their characteristics by performing classical all-atom MD simulations. This approach is more time-consuming than starting from an experimentally-estimated structure, which is what is generally done for non-bacterial amyloids, but it avoids introducing any bias due to measurement limitations (*e.g.*, crystallization). The α-helical secondary structure was chosen because single PSMα1 peptides in solution adopt this configuration, while β-sheet structure is the one generally observed for PSMα1 amyloid nanofibers. Furthermore, other PSMs have demonstrated motif polymorphism[100], and motif influences the pathology of amyloid diseases[85]. For each class, we considered different systems, varying the length of the fiber to account for the size limitation of the simulations, under conditions close to the experiments in solution (310 K, NaCl 0.15 M solution). A complete list of the simulated nanofibers can be found in Fig. A.2.

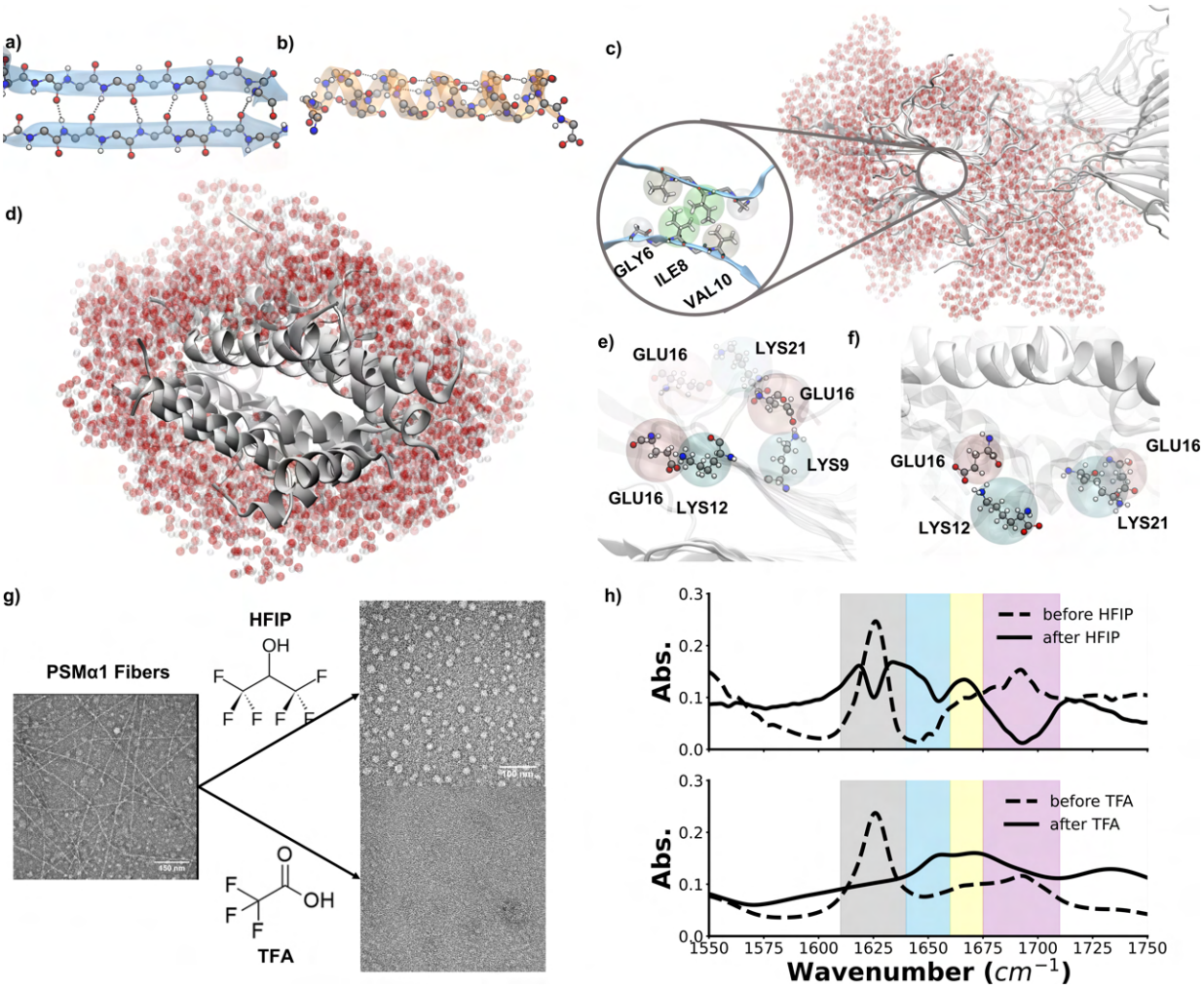

Figure 3.2: **Comparison of (a-f) Computational and (g-h) Experimental Nanofibers.** Hydrogen bonds (black dotted lines) stabilize (a) β-sheet strands and (b) α-helices. Hydrophobic regions in (c) β-sheet nanofibers occur inside each protofilament at a 4-to-6-residue Class 1 steric zipper[62], and in (d) α-helical sheet nanofibers between protofilaments; water atoms in the nanofiber's proximity are red. Salt bridges between GLU16 (pink bubbles) and LYS9, LYS12, or LYS21 (cyan bubbles) are found in (e) β and (f) α nanofibers. (e) Salt bridges formed between GLU16 and LYS9, LYS12, and LYS21 are inter-peptide salt bridges. (f) Salt bridges formed between GLU16 and LYS12, and LYS21 are intra-peptide salt bridges. (g) TEM images of PSMα1 nanofibers in solution (taken by Yichun Wang), pre- and post-treatment with HFIP and TFA. (h) Fourier-transform infrared spectroscopy of pre- and post-TFA and HFIP treatments (data by Yichun Wang). The pre-treated secondary structures of mature nanofibers are primarily β-sheets (1600 cm^{-1} to 1625 cm^{-1}) and β-turns (1700 cm^{-1}); shaded regions are associated with β-sheet (gray), disordered/random-coil (blue), α-helical (yellow), and β-turn (purple) secondary structures.

3.1.2.2 Peptide interactions

Simulated nanofibers assembled with α- and β-motifs share only limited similarities. Both types of aggregates are stabilized by a combination of hydrogen bonding, hydrophobic, hydrophilic, and Coulombic interactions, but where these interactions occur differentiates the two types of aggregates (Fig. 3.2). Within each protofilament, the PSMα1 peptides of β-sheet nanofibers assemble into parallel β-sheet strands (Fig. 3.2a), with hydrogen bonds primarily occurring between residues seven through thirteen. By contrast, the peptides in the α-nanofibers do not form hydrogen bonds with other peptides, but rather within each peptide (Fig. 3.2b). During the simulations, long α-helical aggregates break into smaller clusters, indicating that α-helical peptides are unlikely to form stable assemblies in the absence of external factors. This difference in stability is consistent with the characteristics of the strand interactions. In the α-nanofibers, the peptides orient themselves to form a hydrophobic core (Fig. 3.2d), while the β-strands within each protofilament are connected through a hydrophobic zipper formed by 3-5 hydrophobic amino acids (isoleucine, valine and sometimes glycine, *e.g.*, Fig. 3.2c). The resulting hydrophobic core for each β-sheet protofilament, an approximately 0.6 nm-radius cylindrical region, is smaller than the elliptical region observed for α nanofibers (approximately 2.5 by 1.5 nm for 1α, 2.5 by 3.5 nm for 2α, and 2.5 by 4.5 nm for 3α).

The structures of multi-protofilament nanofibers are also very different: α-protofilaments aggregate in assemblies with a common hydrophobic core but different diameter, while β-protofilaments stretch side-by-side, forming locally planar structures. This behavior can be linked to the distribution of charged groups and salt bridges (a bond between the oxygen atoms of an acidic residue and the nitrogen atoms of a basic residue). Salt bridges form between residue 16 (glutamic acid) and one of three lysine residues (9, 12, or 21) in both α and β aggregates, as shown in Fig. 3.2e & f, with differences, however, in both orientation and most likely participating lysine. In the β-sheet nanofibers, the most common salt bridges form with LYS9 (and partially with LYS12), which is located between the residues making up

the steric zipper (ILE8 and VAL10), easily accessible to GLU16. By contrast, the salt bridges in α-helical sheet nanofibers are predominantly formed with LYS12 and LYS21, as LYS9 is part of the α-helix backbone and, therefore, not as readily available.

Our experiments indicate that the simulated β-structures are in better agreement with the characteristics of the β-nanofibers, as infrared spectroscopy shows a strong signal associated with β-sheets and β-turns (Fig. 3.2g & h). Additionally, treating the mature nanofiber with HFIP, an aprotic surfactant, does not result in a complete nanofiber dissolution and only a partial disappearance of the β-sheets signal, which is compatible with the observed inter-peptide hydrogen bonds, protofilament hydrophobic interactions and location of β-turns. Finally, sample treatment with TFA, which affects the hydrogen bonding, results in nanofiber dissolution and loss of the β secondary structure, with the appearance of a weak α-helix signal, a phenomenon observed also in the simulations for unstable β-nanofibers (Fig. 3.5). These results speak to the fact that β-nanofibers are compatible with experimental observations; however, additional analysis is required to determine the number of protofilaments that compose the PSMα1 nanofiber.

3.1.2.3 Diameter of Nanofibers

The nanofiber's diameter appears to be a consistent feature of both *in vivo* and *in vitro* studies[1,11,21,104] and, therefore, a structural benchmark for our simulated structures. The experimental values for the diameter distribution of PSMα1 nanofibers in solution slightly differs depending on the type of data used (Fig. 3.3a & b), showing a single broad peak and an average value of 10 nm (TEM) and 12 nm (AFM). This discrepancy is likely due to the difference in sample solvation during the two measures. In order to take into account the experimental difference, we also simulated β-structures in vacuum. Of note, as mentioned before, distribution from TEM images remains largely unchanged for the mature nanofiber, with a marginal reduction of the average diameter occurring with the nanofiber aging.

By comparing corresponding experimental and simulated distributions (Fig. 3.3c), that

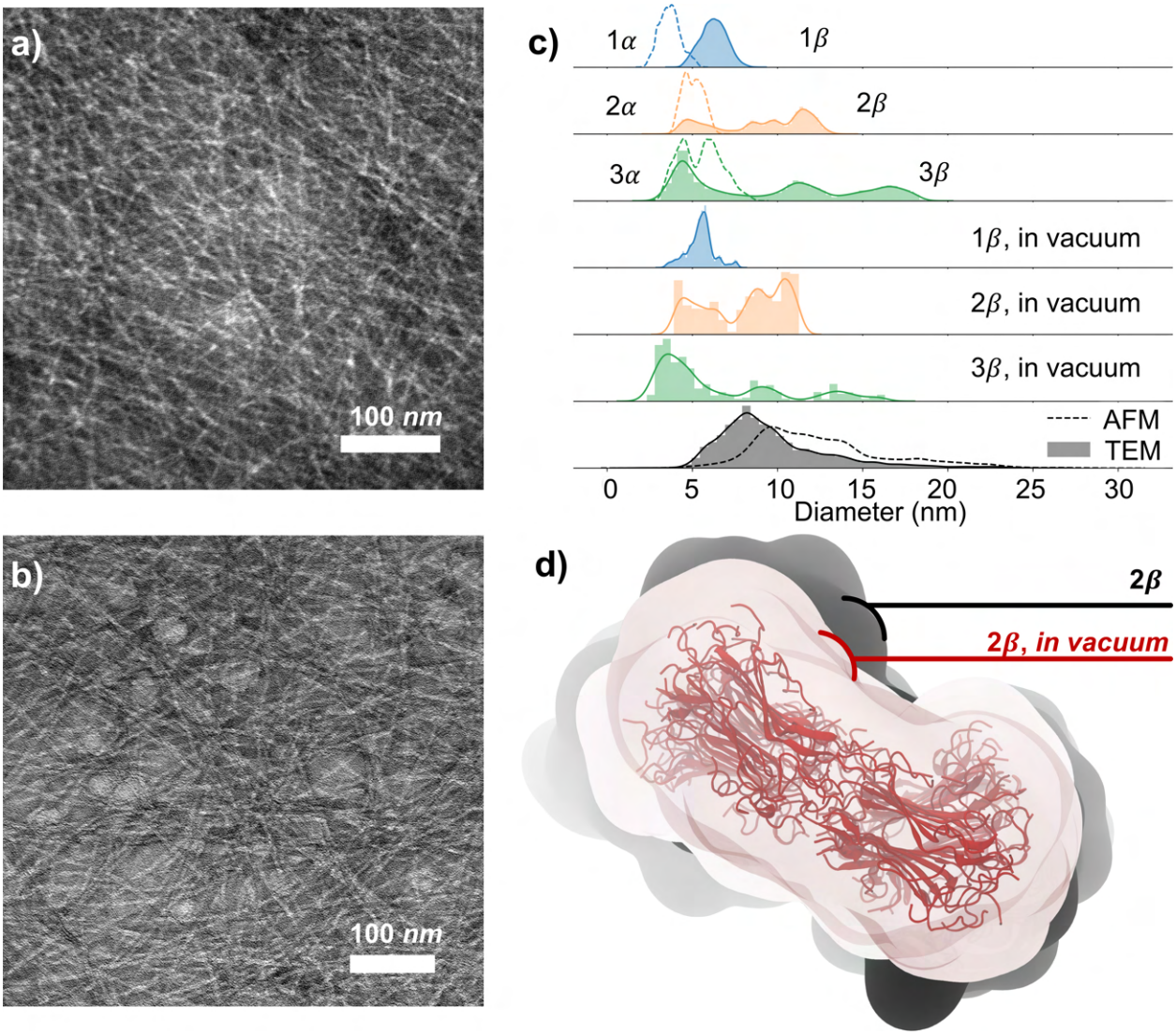

Figure 3.3: **Diameters of (a-c) Experimental and (c-d) Computational Nanofibers**. TEM images taken by Yichun Wang of (a) 21-day and (b) 60-day mature nanofibers. (c) Diameters from simulations for α-helical sheet (dotted, unfilled curves) and β-sheet (solid, filled curves) nanofibers. Distributions of PSMα1 in solution extracted from TEM (solid, filled) and AFM (dotted, unfilled) images are shown at the bottom. (d) 2β nanofiber volume in water (black) and in vacuum (red).

is TEM with nanofiber in vacuum and AFM with solvated nanofiber, we can exclude the 1β system, as it peaks at shorter distances and does not show any value of the diameter above 10 nm, which are present in all the experimental distributions as well as literature data. When it comes to selecting between the 2-protofilament and 3-protofilament structures, the comparison is not as discerning; while the 3β simulated structure tends to have more frequent peaks at short range (thanks to the almost planar structure of the aggregate), the difference with experimental data is not as marked. Moreover, there are several factors that can introduce differences in the diameter distributions when obtained from experiments and simulations. First, the simulation conditions (*i.e.*, fully solvated or in vacuum) do not necessarily match the conditions of the fiber in solution. Even though the shift towards shorter diameters observed in increasing vacuum conditions (*i.e.*, AFM vs TEM) is replicated by the simulations (see Fig. 3.3c & d), the experimental conditions are more likely to be in an intermediate state. Second, the results from the simulations are obtained by uniformly sampling the fiber at every angle; meanwhile, this may not be possible in the experiment due to substrate, preferential direction assumed by the fiber during solvent evaporation, shape of the AFM probe, or other similar factors.

3.1.2.4 Helicity of Nanofibers

As both 2β and 3β are possible candidates for the nanofiber structures in dispersion, we leveraged the differences in structure between these two classes of assembly, to determine if any (or both) structures are likely present in solution. Despite starting from crystal-like topology, which does not resemble the structure in solvent or *in vacuo*, all the simulated β assemblies spontaneously evolve to adopt a helical configuration (Fig. 3.4a) over a short period of time. Moreover, all the β-nanofibers display a left-handed chirality (Fig. 3.4b), which matches the handedness obtained from the CD spectra of the PSMα1 nanofibers in solution. The quantitative comparison for the half-periodicity length (peak-to-peak intensity in the AFM image) shows that the 2-protofilament β-structure better matches the experi-

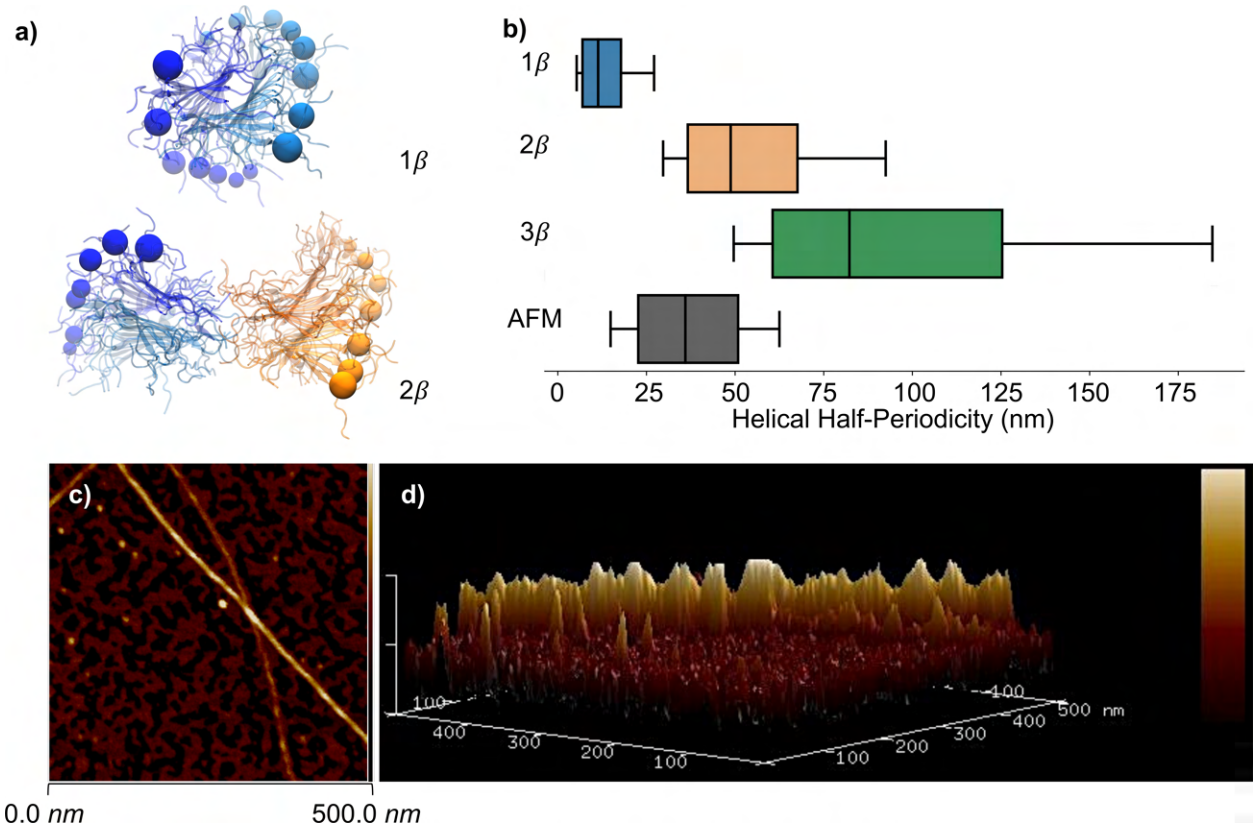

Figure 3.4: **Helical Structure of (a-b) Computational and (b-d) Experimental Nanofibers.** (a) Top view of 1β and 2β nanofiber. Residues at the edge of the nanofiber were drawn with differently-sized spheres to visualize the depth effect. Some layers have been omitted for clarity. (b) β-nanofiber half-periodicity: boxes represent quartiles and whiskers delineate the 10^{th} and 90^{th} percentiles of the distribution. (c) AFM image of mature PSMα1 nanofibers in aqueous solution, taken by Yichun Wang. (d) 3D landscape corresponding to panel (d). The vertical scale bar indicates height from 0 to 7.7 nm.

mental results. Using the interquartile range (IQR) as an estimate of the variability (similar to the standard deviation), we found that the IQR of the AFM data (from 23 nm to 51 nm) overlaps with the IQR of the 2β structure (from 37 nm to 68 nm), which also has a median periodicity of 49 nm. Conversely, the overlap of the experimental observation with the data for the 3β structure is minimal.

Interestingly, the 3β nanofibers tend to have a small layer-to-layer angle or an almost flat conformation (hence the long period), and very short fibers (10 layers, $\sim$4 nm) prefer a right-

Table 3.1: **PSMα1 nanofiber simulations** and their stability (Ⓢ stable, ⊗ unstable). n_{proto} is the number of protofilaments; ρ_{lin} is the linear density along the nanofiber axis in kDa nm^{-1}.

Class	n_{proto}	Type	ρ_{lin}	Ref.[1]	Vac.[2]	Flip.[3]	Mirror.[4]
1β	1	β	9.55 ± 0.05	Ⓢ	Ⓢ	⊗	Ⓢ
2β	2	β	19.48 ± 0.22	Ⓢ	Ⓢ	⊗	⊗
3β	3	β	29.15 ± 0.21	Ⓢ	Ⓢ	⊗	⊗
1α	1	α	4.88 ± 0.01	Ⓢ	Ⓢ	⊗	⊗
2α	2	α	6.83 ± 0.15	Ⓢ	Ⓢ	⊗	⊗
3α	3	α	9.88 ± 0.14	Ⓢ	Ⓢ	⊗	⊗

[1] Reference systems in water; *L*-peptides. [2] Same as the reference systems, but in vacuum. [3] Flipped configuration: fiber chirality is inverted; *L*-peptides. [4] Mirror configuration: fiber and peptide chirality are inverted (*D*-peptides).

handed chirality (Fig. A.5), an effect which disappears for longer strands. This behavior, together with the low stability of the flat conformation, resulted in instability of certain lengths of 3β nanofibers during the simulations. This observation is in contrast with the other types of aggregates that rapidly assume their helical structure when starting from flat conformation at any length.

These results suggest that the nanofiber can become locally unstable when more than two protofilaments are associated, limiting the ability of the fiber to grow laterally, and that one of the potential roles of the associated extracellular DNA observed *in vitro*[4] is to provide additional stability by hindering lateral growth of the nanofiber. This local instability would also explain the long time required for nanofibers in solution to reach a stable conformation ($\sim$ 14 days), compared to *in vitro* observations (in as few as 2 to 5 days), as lateral aggregation is still possible until most of the peptides are aggregated in a more stable nanoscale assembly. Similar phenomena have been reported before; the lateral growth of other amyloid nanofibers (Aβ of Alzheimer's disease, lysozyme, HET-s prion, and SAA_{1-12}, among others) due to chiral-specificity has been previously observed[116–118],

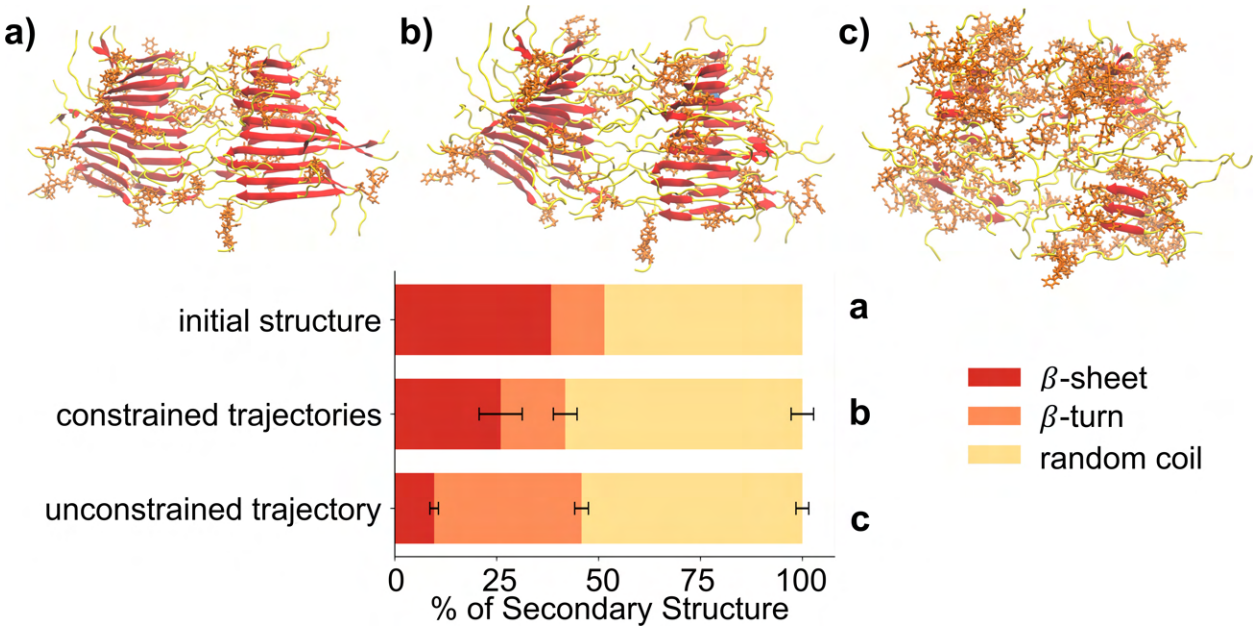

Figure 3.5: **Dissolution of a Flipped (*R*-enantiomer) 2β Nanofiber Model** and its secondary structure. Starting (a) from the flipped 2β configuration, (b) the restraints on the *R*-enantiomer of the nanofiber are gradually removed and (c) the system is then simulated without restraints. Error bars represent standard deviation.

with some studies proposing that amyloid nanofibers have exclusively left-handed chirality, although this hypothesis has been, by now, disproved[119].

The chirality reversal observed for the very short 3β strands during the simulations allude to the possibility of other structures assuming a right-handed conformation. To this end, as we did not observe their spontaneous formation, we directly tested the stability of these structures by taking the stable conformation (left-handed nanofiber, *L*-peptides) and either (1) inverting the chirality of the nanofiber (*i.e.*, right-handed helix) leaving peptide chirality unaltered (flipped nanofiber) or (2) inverting the chirality of both fiber and peptides (mirrored nanofiber). The results, shown in Table 3.1, indicate that both flipped and mirrored systems are unstable (with the notable exception of 1β formed by *D*-peptides). The instability did not stem from a simple disaggregation of protofilament or strands, but rather, as shown in Fig. 3.5, by a complete loss of the β-sheet structure of each peptide,

starting at the hydrophilic, randomly-coiled regions of the fiber and propelling toward the steric zippers at the center of the protofilaments.

3.1.3 Conclusions

PSM-derived functional amyloids are highly-ordered nanofibers that play a variety of important roles in the ECM of *S. aureus* biofilms. We determined the molecular structure of PSMα1-derived nanofibers and their characteristics, leveraging a combination of atomistic simulations and experiments, including mass spectroscopy, CD spectroscopy, TEM, and AFM. PSMα1 peptides in solution assemble into cross-β-sheet structures that spontaneously adopt a left-handed helical geometry, with an average diameter of about 12.5 nm and a periodicity of $\sim$72 nm. According to CD spectra and TEM images, the aggregates continuously evolve in the observed timeframe, although the majority of changes happen in the first two weeks. These "mature" nanofibers are stable to thermal and sonication stress, but can be partially or fully dissolved by treating the solution with HFIP or TFA, respectively. The characteristics of the nanofibers closely match a structure composed of two protofilaments, where β-sheet peptides form strands *via* intermolecular hydrogen bonds and pairs of strands form protofilaments largely by virtue of a hydrophobic steric zipper. The aggregation of protofilaments is stabilized by Coulombic interactions in a disordered region, composed of the random coils of the protofilament peptides.

In the absence of external factors, PSM-derived nanofibers show a longer time to stabilize than previously reported; even though fibers are clearly formed after 4 to 9 days, they continue undergoing small, but detectable, changes for about 2 weeks. This time evolution might be the consequence of the slow equilibration of the aggregates towards a two-protofilament structure, a process that in *in vitro* and *in vivo* is probably aided by other constituents in the ECM (*e.g.*, extracellular DNA).

The number of protofilaments in the nanofibers affects the chirality and the stability of the structures. Three-protofilament aggregates are the most striking example of this

phenomenon: While longer fibers (20 layers) form left-handed helices, short ones (10 layers) assume the opposite chirality. We speculate that, as short protofilaments are formed, the addition of a third strand causes either strain or instability for the structure, resulting in partial dissolution or fiber breakage. This process of destabilization might be responsible for the extremely slow equilibration time observed in solution, and it may represent an additional reason why extracellular DNA is associated with the PSMα1 nanofibers in biofilms. The extracellular DNA, besides concentrating the peptides, can potentially guide the chirality of the nanofiber, promoting the aggregation of two protofilaments, while hindering additional lateral growth or speeding up the recovery when a partial disaggregation occurs. While the two-protofilament fiber is the single best model among the ones we tested, it does not fully match the experimental data by itself. This discrepancy can be explained by the existence of polymorphs in solution, which is not only common for amyloids[120], but is also a consequence of the proposed growth mechanism. Not only short segments with three or four protofilaments are expected, but small aggregates, which may also retain some α-helical connotation, may briefly form as well.

The results of this work provide insights on the properties and characteristics of PSM-derived amyloids and can aid in the design of anti-amyloids compounds with nanoscale dimensions, exemplified by chiral nanoparticles[39]. MD simulations can be used as a tool to assist in exploratory research aimed at unraveling the cross-binding of fibers, inhibiting or reversing protein aggregation, and they may be an important tool when it comes to optimizing prospective nanomedicine candidates in the future.

CHAPTER 4

Combating Biofilm at the Cellular Level

4.1 Low-THz Vibrations of Biological Membranes

4.1.1 Introduction

The internal motions of biological membranes have increasingly been the focus of biological research, as they provide a connection between membrane composition and many biological processes[35]. For example, membranes' vibrations and density fluctuations have been linked to the transport of small molecules across membranes[31–34]. These processes and the membrane mechanical properties are influenced not only by the presence of transmembrane proteins and membrane composition[121–125], but also emerging molecular structures and their distributions play a critical role. For example, lipid asymmetry across bacterial membranes has been linked to varying susceptibility to antibiotics[126–128], and lipid rafts — the non-homogeneous distribution of lipids into localized regions— play a role in several biological processes[35,122–124].

First proposed in 1911[36], the idea that mechanical vibrations are an identifying feature of various compounds has been extensively studied in the past century[129–135]. Likewise,

The information in this chapter is available in the following cited publication. Chloe Luyet, Paolo Elvati, Jordan Vinh, and Angela Violi. Low-thz vibrations of biological membranes. Membranes, 13(2):139, 2023.

there exists a clear link between the mechanical properties of a membrane and its properties, and in turn its functionality, which has motivated research investigating the relationship between membrane vibration and cellular activity. Recently, this line of thinking has been used to show that vibrations can be used as a means of distinguishing among microorganisms[136,137], and to study the interactions between membranes and anchored or adjacent external structures, like in bacterial biofilms[138,139]. Moreover, an increasing number of studies have identified modes of membrane-adjacent structures. For example, functional amyloid fibers, proteinaceous fibers that grow in biofilm and anchor to the bacterial membranes, have been suggested to mechanically vibrate and deliver a damped vibrational signal to an adjacent bacterial cell[138–140]. Electromagnetic signals on the order of kHz of bacterial DNA that match DNA extracted from Alzheimer's and other amyloid-induced diseased patients[37] suggest that bacterial infections are present in such illnesses. THz vibrations have also been observed in protein-ligand binding[141] and other biological polymers[142,143], suggesting that protein-ligand interactions trigger unique changes in vibration that can be used in detection and diagnoses.

Despite these promising results, work in this direction has been hindered by several factors. Experimentally, membranes' mechanical and structural characterization, as well as cellular identification, have been expensive and time-consuming[35,122–124,135–137]. Indeed, many of the early works that discussed the use of mechanical vibrations as an identification tool speculated that computation would eventually dominate the field[130,132,133]. Nonetheless, while computationally probing the vibrational modes of biological structures, like membranes, is simpler, it is computationally demanding, which has led to less accurate approaches (*e.g.*, coarse-graining, continuous models) and assumptions (*e.g.*, membrane composition and structure)[144–151] of limited usefulness or reproducibility. Finally, even when data is available, an unbiased method for the identification and comparison of the vibrational spectra has long been a complex challenge[132,134,152–155].

To fill this gap, we propose an approach that combines atomistic molecular dynamics sim-

ulations, to gather information about the low-THz vibration of disparate membranes, with signal processing, to identify and compare their vibrational spectra. Using this approach, we discuss the effect of membrane asymmetry and lipid composition (with and without sterols) on the vibrations, as well as some hidden pitfalls that are potentially introduced by the use of atomistic simulations. Moreover, by employing a nonparametric test, our comparisons allow us to test the variability among samples obtained of the same system, and quantify spectral uncertainty.

4.1.2 Systems

In this work, instead of taking the standard approach of exploring the effect of each possible parameter (*e.g.*, the concentration of each possible lipid), we focused on three complex membranes using realistic compositions, as discussed in the following. We chose this approach because looking into the effect of all the possible parameters of a membrane is a generally daunting task, given the number of possible lipids and their concentrations (*e.g.*, *B. Subtilis* has at least 127 different lipids), and their often nonlinear relations. The latter is a critical consideration, as it can make the effort of decomposing the problem in simpler tasks very challenging; the addition of a single type of lipid can markedly change certain observed properties, like the spectra in the range of interest here. We show such an example at the end of this manuscript, when discussing the effect of sterols and LPG.

With this in mind, instead of trying to create a general model, we aimed to (1) determine if we could detect any difference between real compositions and (2) discuss the problems simulations would encounter in sampling more realistic and therefore complicated systems. We studied the plasma membranes of three types of cells, two of bacterial (*Staphylococcus aureus* and *Bacillus subtilis*) and one of mammalian (rat liver plasma[156]) origin. We chose *S. aureus* because of its high pathogenicity and prevalence in hospital-acquired infections[93,94], *B. Subtilis* thanks to its ubiquity and innocuousness in healthy individuals[157], and rat liver cell membrane as an example of mammalian plasma membranes. For *S. aureus*, we considered

two asymmetric membranes with different composition ($S476^{A}_{33}$, $S476^{A}_{51}$), observed at two different values of pH (*i.e.*, 5.5 and 7.4), as well as a symmetric membrane ($S476_{33}$) as close as possible to $S476^{A}_{33}$, to study the effect of lipid distribution between leaflets[126,144,158–163]. For *B. Subtilis* and rat liver cells, however, we could only find information about the total composition of the plasma membranes and therefore, we simulated homogenous bilayers. These five systems are illustrated in Figure 4.1a. Additionally, we simulated four membranes, derived from $S476^{A}_{33}$ and $S476^{A}_{51}$ by adding to each one of them 1.3% molar[164] of either ergosterol (ERG) or cholesterol (CHL). For all the membranes, 3 to 9 independent replicas were generated and simulated.

Except when noted otherwise, the *S. aureus* membranes consist of a periodic bilayer of 15 nm x 15 nm in size (approximately 700 lipids, exact number depends on composition), the *B. Subtilis* membrane 16 nm x 16 nm in size (840 lipids), and the rat liver membrane, 12 nm x 12 nm in size (600 lipids). These sizes were chosen based on the estimated lowest frequency mode (f_{min}) that could be observed,

$$f_{min} = \frac{s_{membrane}}{L_{max}} \tag{4.1}$$

where $s_{membrane}$ is the speed of sound in the membrane and L_{max} the longest distance between two points on the x-y dimension (membrane plan) of the periodic box. Since $s_{membrane}$ is hard to estimate accurately, we conservatively used the speed of sound of water ($1550\,\mathrm{m\,s^{-1}}$), which is greater than alcohols and alkenes with long aliphatic chains (1150-1250 $\mathrm{m\,s^{-1}}$), which places an upper limit to f_{min} of approximately 0.1 THz.

4.1.3 Results

Before analyzing the differences among replicas of different membranes, we tested the force field and relaxation protocol. As atomistic molecular dynamics has been extensively proven in the literature to be suitable to model bilayer dynamics, we performed a minimal

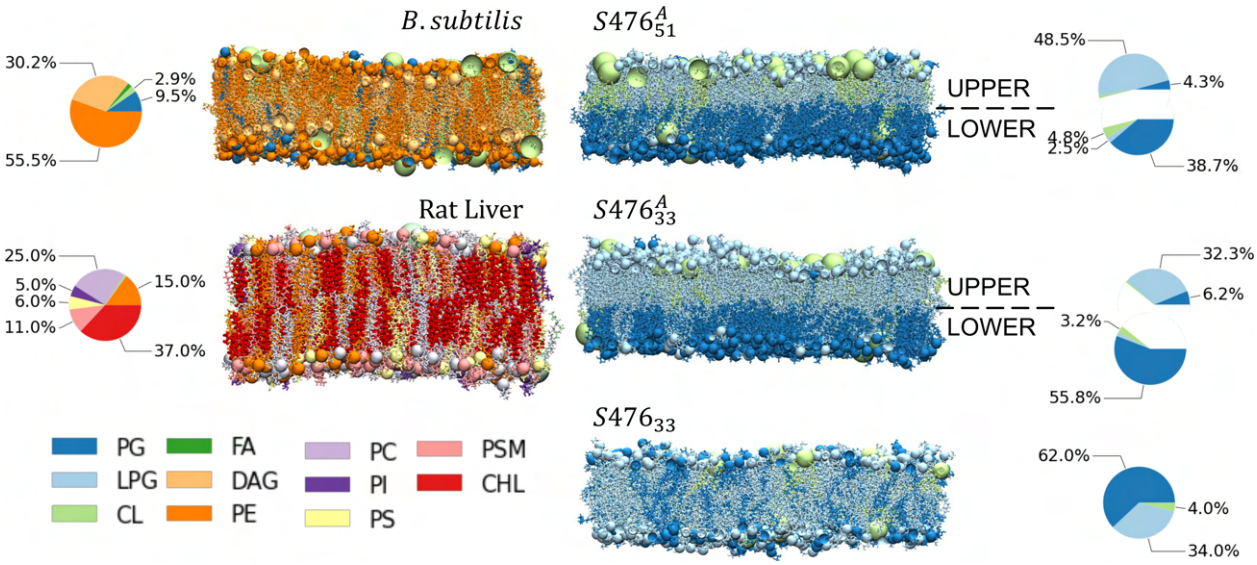

Figure 4.1: **Systems and Nomenclature Summary.** Composition and distribution of five types of plasma membranes modeled in this work: one for *B. Subtilis*, one for rat liver cell, and three for *S. aureus* (*S*476) membranes. *S. aureus* membrane are labeled according to symmetry (A for asymmetric) and percent concentration of LPG (33% or 51%). Only composition fractions greater than 2% are labeled; PG, LPG, CL (cardiolipin), FA, DAG, PE, PC, PI, PS, PSM, and CHL. Only non-sterol containing membranes are shown.

validation by computing the Langmuir isotherms in the between −4.2 MPa and 1.5 MPa for $S476^{A}_{33}$, $S476^{A}_{51}$, and $S476_{33}$. The comparison with experimental data (Figure B.2) shows that the difference of our estimates is well below the uncertainty (standard deviation).

As a second step, we tested the potential bias introduced by using periodic boundary conditions (*i.e.*, size effect). To this end, we compared the spectra of membranes with identical composition ($S476^{A}_{33}$) but having four different periodic system sizes (15 nm x 15 nm, 4 nm x 15 nm, 3 nm x 15 nm, and 3 nm x 12 nm). The results show (Figure B.7) that peak location is unaffected by the size of the bilayer patch, but the normalized intensity is marginally weaker for the smallest membranes. In the following, however, we will only use square periodic patches (15 nm x 15 nm for *S. aureus* systems, 16 nm x 16 nm for *B. Subtilis*, and 12 nm x 12 nm for rat liver, see *Methods*), to avoid introducing any anisotropy in the systems.

4.1.3.1 Membrane Asymmetry

The asymmetry in the membrane composition is suggested to play a key role in many cellular processes. At the same time, accurate information about the distribution of species between leaflets is generally scarce, due to the difficulty of experimental measurements, as well as the dynamic nature of the cellular membrane make-up. As a larger number of average compositions are available in the literature, we compared the differences in the vibrational spectra between symmetric and asymmetric *S. aureus* systems ($S476^{A}_{33}$ and $S476_{33}$). The initial comparison (see Figure 4.2), while showing a statistical equivalence between the peaks of the two systems, was surprisingly affected by large uncertainty, despite the number of replicas used for each system (9 for $S476_{33}$ and 6 for $S476^{A}_{33}$).

To investigate the rationale behind this observation, we looked into the similarity among replicas of a given membrane. To make sense of all these comparisons, we built an undirected weighted graph (Figure B.8a), where each node is a replica and the weight of each edge is equal to 1 - KS (*i.e.*, similar spectra are connected by an edge with higher value). Different types of clustering analyses can be performed to obtain such a graph, but the consistent

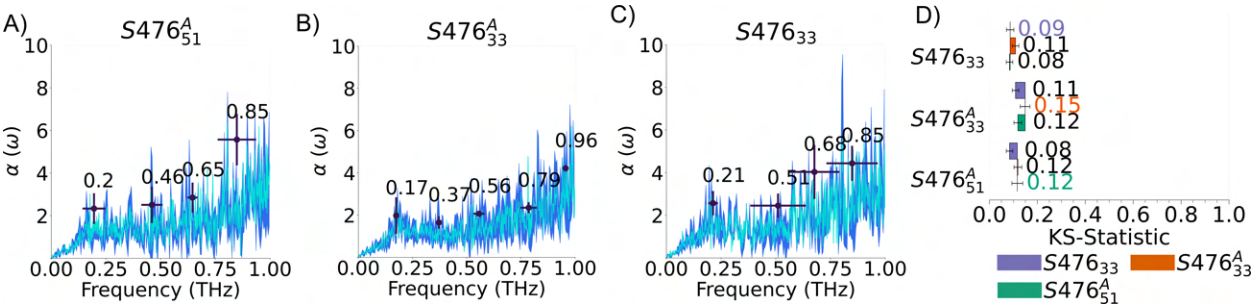

Figure 4.2: **Effect of composition and distribution on *S. aureus* membrane's spectra.** (A-C) *S. aureus* membrane average spectra (cyan), standard deviation of spectra (dark blue), and peaks (black); error bars represent standard deviations. For $S476^{A}_{33}$ and $S476_{33}$ the spectra are computed from the largest cluster of replicas (Figure B.8). (D) Kolmogorov-Smirnov (KS) statistics; error bars represent the standard error of the mean. Self comparison (*e.g.*, $S476_{33}$/ $S476_{33}$) indicates the average difference between replicas of the same system. KS statistic shows that this part of the absorption spectra for the three systems are not distinct.

result is that the replicas are not separated, as expected, in two groups based on their leaflet symmetry, but rather in three groups, where both types of systems are somewhat mixed. Given the microcanonical nature of the simulations used to generate the spectra, the reason for this clustering is a dependence on the initial conditions, likely resulting in some violation of the ergodic hypothesis. To narrow down the source of this difference, we considered the effects of the membrane thickness (Figure B.8a), periodic system size, and surface tension (Figure B.8b) on the spectra, but we found no strong correlation in all cases. Thus, we hypothesize that the differences are related to slightly different stability in the vibrational modes that are sampled, due to slightly different initial velocity distribution. This hypothesis is corroborated by the analysis of the peaks, which shows that, with the notable exception of the lowest frequency ($\sim 0.2\,\mathrm{THz}$), the peaks display variability in intensity and location between groups (Figure B.8c).

This analysis leads to three main conclusions. First, it shows that the leaflet symmetry, for equivalent total composition, does not have a statistically significant effect on the spectra, whether we consider KS statistic of the average of all replicas or we restrict ourselves to one

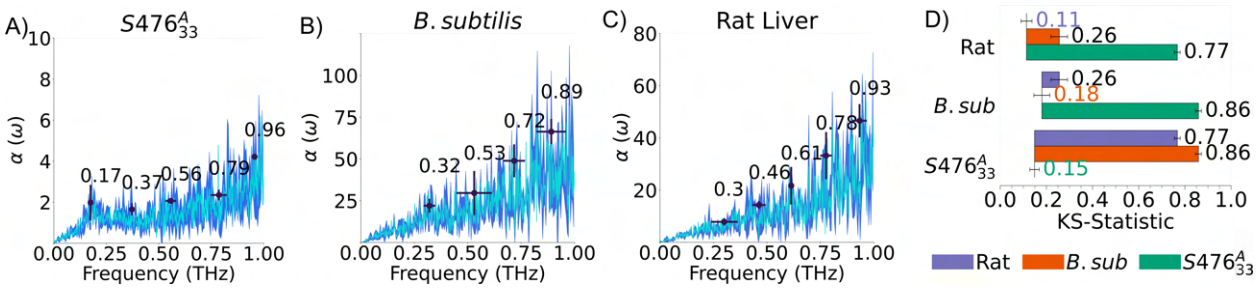

Figure 4.3: **Plasma membranes absorption spectra of different species.** (A-C) Average spectra are shown in cyan, standard deviation in spectra (dark blue), and peaks are labeled by black points; error bars represent standard deviations in peak location and intensity. The *S. aureus* membrane is the only one among the three that has a peak in the (0.17-0.2 THz) region. (D) Kolmogorov-Smirnov (KS) statistics; error bars represent the standard error of the mean. Self comparisons (*e.g.*, Rat / Rat) indicate the average difference between replicas of the same system. KS statistic shows that *S. aureus* spectra is very distinct from the other two, even though *B. Subtilis* and Rat spectra are still statistically discernible.

of the replica clusters, like in Figure 4.2. Of note, the membrane symmetry can still affect other processes, as well as other mechanical properties. Second, despite the differences and the complexity in comparing the spectra of each replica, the lowest frequency peak (between 0.17 THz-0.21 THz) is conserved in all *S. aureus* systems and replicas. Finally, the spectra obtained from simulations should be carefully tested for internal consistently. Even though we observed statistical variability only among replicas of two *S. aureus* systems in this work, this issue should be tested to avoid adding systematic uncertainty to the results, especially as we will show, below, for more rigid membranes.

4.1.3.2 Cell type

After establishing the effect of composition and lipid distribution for *S. aureus* membrane, we compared the spectra of the plasma membrane of different cells, namely we compared *S. aureus* with one other common bacterium as well as a mammalian cell.

The results (Figure 4.3) show that the *S. aureus* absorption spectra in the low-THz region is rather distinct from the other two, with a characteristic peak, just below 0.2 THz.

Of note, this distinction holds regardless of the *S. aureus* replicas or the symmetry chosen (Figure B.9). *B. Subtilis* and rat liver cell are also statistically distinct, although notably more similar than *S. aureus*, despite the remarkably different composition. Notably, these differences are the results of the interplay between lipids and not a simple inertial behavior due to the difference in the membranes' density: the mass per unit area of $S476^{A}_{33}$ (approximately $2.4\,\mathrm{kDa\,nm^{-2}}$) falls between the one for *B. Subtilis* (approximately $2.2\,\mathrm{kDa\,nm^{-2}}$) and the mammalian cell (approximately $2.6\,\mathrm{kDa\,nm^{-2}}$).

4.1.3.3 Sterols

Finally, we looked in the effect of the presence of sterols on the *S. aureus* membrane. Bacterial cells do not typically synthesize sterols, as the bacterial cell wall occupies the same function fulfilled by sterol-containing plasma membranes in eukaryotic cells by maintaining structural integrity and fluidity. However, cell-wall-deficient forms of *S. aureus*, called L-forms, do exist[165]. As staphylococcal L-forms lack cell walls, sterols provide a means of maintaining structural integrity and fluidity[166]. More importantly, the presence of sterols has been linked to increased resistance to antimicrobial peptides[167] and lipid raft formation, demonstrating their importance in membrane function and biological processes. For this reason, we analyzed the effect of sterols on the absorption spectra by comparing the spectra of the asymmetric *S. aureus* membranes (without sterols), with identical membranes to which we added either 1.3% cholesterol or ergosterol[164].

The presence of sterols in the membranes (see Figure 4.4) had a greater effect on the spectra of $S476^{A}_{33}$ than that of $S476^{A}_{51}$. This difference can be related to the different content of LPG between the two membranes, as higher levels of LPG decrease the membrane fluidity[168–172], causing a slight change in the absorption spectra. These results agree with a study in which mutant bacteria, producing less LPG, have membranes with a reduced rigidity[173]. Indeed, the presence of high LPG concentration, much like low concentration of sterols, has been shown to have a stabilizing effect on membrane fluidity[169,170]. While these effects do

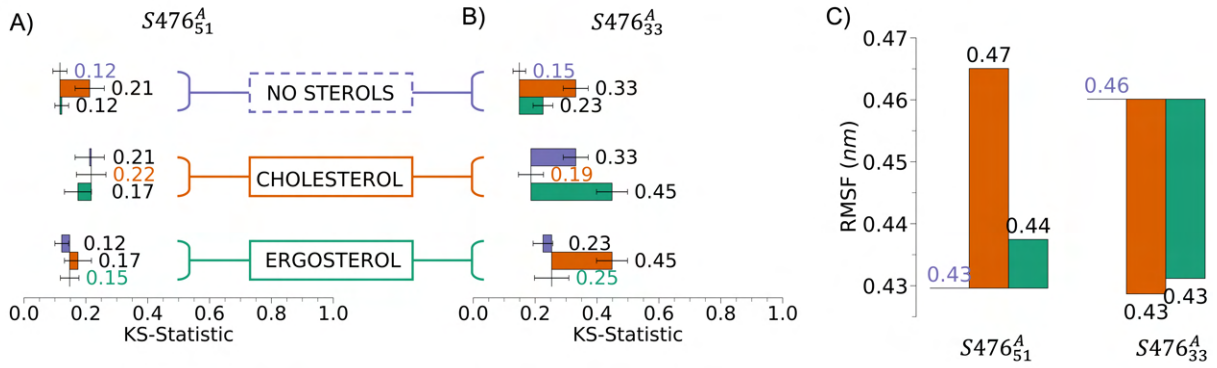

Figure 4.4: **Difference in the spectra due to the presence of sterols in *S. aureus* membranes.** Plots show the results of two-sample Kolmogorov-Smirnov (KS) tests for the average spectra of (A) $S476^{A}_{51}$ and (B) $S476^{A}_{33}$, without any additional sterol, and with 1.3% cholesterol or ergosterol. Error bars represent the standard error of the mean. (C) Average mobility measured as root-mean-squared fluctuations (RMSF) of the positions of non-sterol atoms in $S476^{A}_{51}$ and $S476^{A}_{33}$ membranes, without sterols (baseline) and with cholesterol (orange) or ergosterol (green).

not compound ($S476^{A}_{51}$), a membrane with a lower concentration of LPG ($S476^{A}_{33}$) would be more susceptible to changes caused by sterols. It is interesting that sterols in the membrane with more LPG cause an increase in mobility, as measured by the average atomic RMSF, while sterols in the membrane with less LPG cause an increase in rigidity (Figure 4.4c). Finally, cholesterol typically affects the membrane mechanical properties more than ergosterol (Figure 4.4b), which agrees with the experimental observation that ergosterol has a smaller effect on membrane mobility than cholesterol[167].

4.1.4 Discussion

The unique absorption spectra of biological membranes are a promising metric for species differentiation and bio-process identification. In this work, we show how to estimate, analyze, and compare the absorption spectra of bacterial and mammalian membranes, by combining molecular dynamics simulations and signal processing techniques (*i.e.*, peak detection and KS statistics). The analysis of *S. aureus*, *B. Subtilis*, and rat liver cells, shows that distinct

peaks can be identified for different species in the low-THz region and that certain peaks, for *S. aureus* around 0.19 THz, are present even for different compositions and symmetries, making them good identifiers under a variety of conditions.

The ability to rigorously compare noisy and complex spectra, like the one studies here, opens the door to finding unexpected correlations. For example, *S. aureus* membranes (at 7.4 pH) have a lower LPG content, which we found is associated with both increased variability among replicas and higher susceptibility to changes in mobility in the presence of sterols. This change could speak to higher rigidity in membranes with more LPG, as LPG tends to maintain membrane fluidity[168–172]. While higher fluidity may have biological advantages, it seems inversely correlated to antibiotic resistance as, generally, an increase in resistance of membranes to antimicrobial peptides is associated with higher concentrations of LPG[169,174] and sterols[167].

The comparison of spectra of different samples of the same system also provides a way to find similarities, even for complex signals like the one presented here. Different samples can be clustered and analyzed by building fully connected graphs, where edges are weighted based on the values of a two-sample KS test. This representation, allows visualizing and finding similarities on high dimensional spaces, like the 105th-dimensional space of the comparisons between 15 *S. aureus* samples in this work. While we found that the existence of clusters among the samples affected only the most rigid membrane (see the previous discussion about LPG content), it is nevertheless allowed extracting data from samples that would have been otherwise affected by a high uncertainty.

Finally, while this work was designed around the low-THz absorption spectra of plasma membranes, it can immediately generalize to other structures (*e.g.*, fibers present in biofilm matrix), other regions of the vibrational spectra, as well as to data obtained from experimental techniques. Our work reinforces the idea that vibrations can be used to successfully differentiate between different biological complexes and how they are affected by specific changes, which, then, can potentially be related to biological functions. This link, if present,

could inform a route by which these vibrations could be manipulated, for very targeted effects[37].

CHAPTER 5

Combating Biofilm with Carbon Nanoparticles (CNPs)

5.1 Chiral Carbon Nanoparticles (CNPs)

5.1.1 Introduction

Biofilm formation is a defense mechanism employed by bacteria to withstand hostile environments, evade immune responses, and resist antibiotics[175,176], as the embedded bacterial cells within biofilms exhibit significantly higher antibiotic resistance compared to free-floating cells[177,178]. Chiral CNPs have previously demonstrated antibacterial activity by generating reactive oxygen species, disrupting cell membranes, and interacting with intracellular proteins[52,53]. The stability, low toxicity[179,180], and high molecular weight of chiral CNPs make them promising candidates for anti-biofilm applications[39].

The unique physicochemical properties of carbon nanoparticles (CNPs) have sparked significant research interest. CNPs with an average diameter of less than 10 nm possess desirable optical and electronic properties, similar to semiconductor nanoparticles while avoiding

Some of the information in this chapter is available in the following cited publication and the rest is soon-to-be-published material. Misché A. Hubbard, Chloe Luyet, Prashant Kumar, Paolo Elvati, J Scott VanEpps, Angela Violi, and Nicholas A Kotov. Chiral chromatography and surface chirality of carbon nanoparticles. Chirality, 34(12):1494–1502, 2022. Experimental methodologies performed by Misché Hubbard have been omitted; however, in-text references to experiments performed by Misché Hubbard are denoted appropriately.

issues such as heavy metal toxicity, harsh synthesis conditions, and expensive starting materials[181–183]. CNPs, along with other nanocarbons, are highly stable, chemically inert, and biocompatible, making them useful for various applications such as light-emitting diodes[184], biosensors[185], photocatalysts[186], bioimaging[180], and drug delivery[49]. Another advantage of nanoparticles is their diverse sizes, shapes, and functional groups.

Mirror asymmetric CNPs, which exhibit multiple scales of chirality from molecular to nanoscale, have the added advantage of chiral recognition for various applications involving biomolecules with similar hierarchy of chirality. For example, *L*-CNP made from *L*-lysine has been found to remodel the secondary structure of amyloid-β (aβ-42) peptides and inhibit key factors of pathogenesis, while *D*-CNP made from *D*-lysine have little to no biological activity against the same peptide[54]. Furthermore, experimental results reveal that both *L*- and *D*-CNPs can disperse *S. aureus* biofilms, but *D*-CNPs exhibit enhanced anti-biofilm activity. Importantly, chiral CNPs do not affect the growth of planktonic *S. aureus* cells, indicating their specificity towards biofilm dispersal and highlighting the chiral recognition capabilities of CNPs within the ECM. Chiral chromatography analysis confirms the stability of CNPs in the biofilm supernatant. Likewise, it is worthwhile to investigate the potential of chiral CNPs to interfere with the self-assembly process of amyloid-like proteins within the ECM of biofilms, leading to their disruption.

If multiscale enantiomers of CNPs are expected to elicit distinct biological and pharmacological responses, there is a pharmacological demand to separate the two enantiomers. Moreover, to determine the chiral centers of CNPs and develop reproducible methods for separating enantiomeric NPs, it is crucial to know whether the chiral centers are located inside the particles or at their interfaces. Nonetheless, chiral separations of nanoparticle solutions using high-performance liquid chromatography (HPLC) have not been achieved yet, though using teicoplanin, a macrocyclic glycopeptide, as the column's stationary phase has shown promise in separating other chiral compounds[187–189].

In this study, we achieve two things: (1) we investigate the potential of chiral carbon

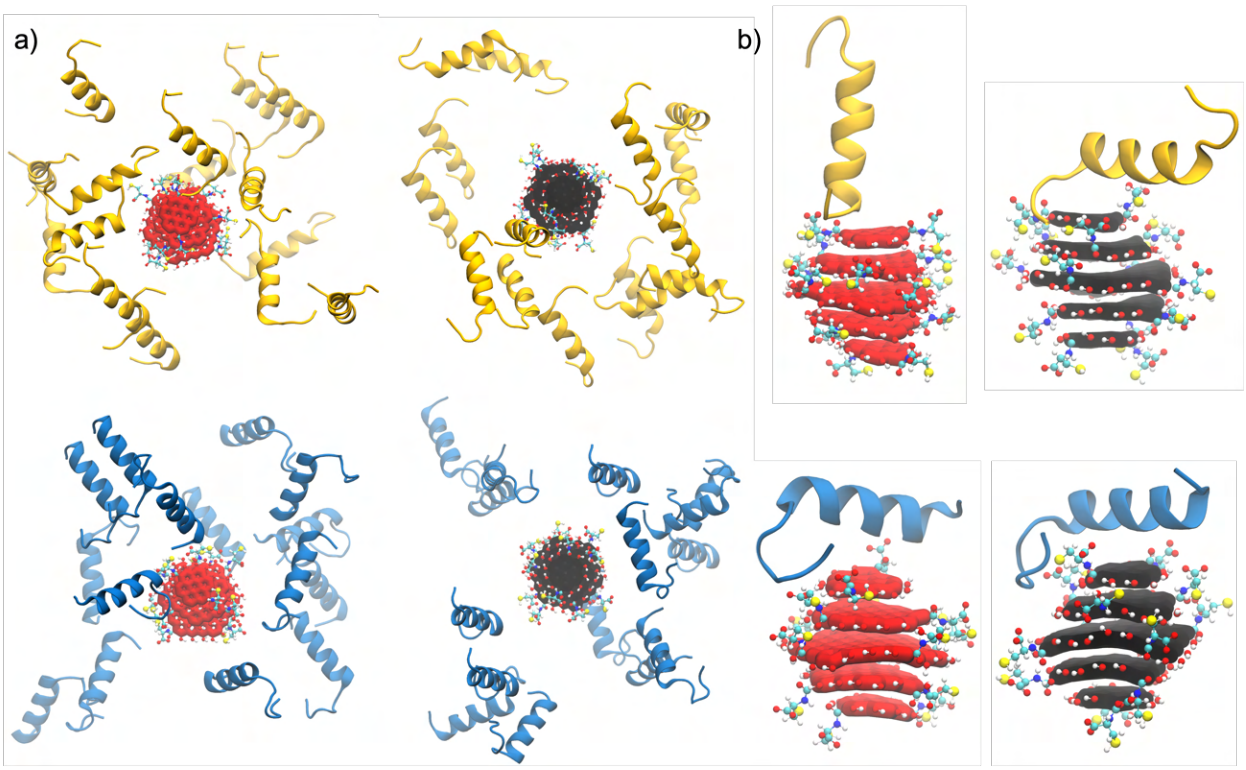

Figure 5.1: **Example of initial configurations** for (a) a **group** (15) of PSMs surrounding 1 CNP and (b) a **single** PSM interacting with 1 CNP. *D*-CNP is shown in red, *L*-CNP in black, PSMα3 in blue and PSMα1 in yellow. Water and ions are hidden for clarity.

nanoparticles (CNPs), derived from *L*- and *D*-cysteine, to disrupt biofilms based on their interactions with PSMs and (2) we demonstrate that a teicoplanin stationary phase has a chiral-dependent affinity for CNPs, which explains how a simple water/acetonitrile mobile phase was used to achieve chiral separation of cysteine-derived chiral CNPs.

5.1.2 Systems

We performed two sets of experiments (see Figure 5.1) to investigate CNP-PSM interactions, one aimed at understanding the specific interactions between peptide and nanoparticle (a **single** PSM + 1 CNP) and one to emulate a strong local concentration of PSMs (a **group** (15) of PSMs + 1 CNP).

To create a reasonable initial configuration of a single PSM interacting with a CNP, we

used HDOCK[190], by taking the top 10 most likely binding configurations of each PSM with each layer of each CNP. Of the resulting 120 configurations (2 PSMs x 2 CNPs x 3 molecules in each CNP x 10 predictions), only about 14% (17 configurations) were not discarded due to nonphysical atomic overlap. All these configurations were equilibrated using the protocol described above, but systems that did not equilibrate with 200 ns, were discarded, leaving only 11 systems (3 for PSMα1/*D*-CNP, PSMα3/*D*-CNP, and PSMα3/*L*-CNP, and 2 for PSM/*L*-CNP). The systems with 15 PSMs were generated by randomly placing the peptides around the CNP at an average COM-COM distance of 3- 4 nm. PLUMED[59] was used to place upper limits on the distance between the centers of mass of each PSM, with the CNP at the center. The walls were weak enough that the peptides could drift from the CNP and cluster among themselves.

To mimic the chromatographic conditions and investigate the chiral specificity of a teicoplanin stationary-phase column, two simplified models were created, one for teicoplanin with each chiral NP made from two cysteine enantiomers.

5.1.3 Results and Discussion

5.1.3.1 PSM-CNP Interactions

PSMs bind to CNP with chiral specificity. In all the simulations, we observe that the peptide will form long-lasting interactions with the CNPs. Specifically, we detect the formation of long-lived hydrogen bonds between the PSMs and the nanoparticles, with an average of about 8 peptides directly interacting with the CNP. While the interactions involve a variety of residues, from N-terminus, to C-terminus, and other, more central residues, lysine (LYS) residues show significant specificity in their preference for *L*-CNP over *D*-CNP. As shown in Figure 5.1, LYS residues on both PSMs form longer-living hydrogen bonds with *L*-CNP.

This chiral specificity is not limited to LYS groups, but extends also to Asparagine (ASN) C-terminal residues, ASN21 and ASN22 (present only on PSMα3), which form bonds with

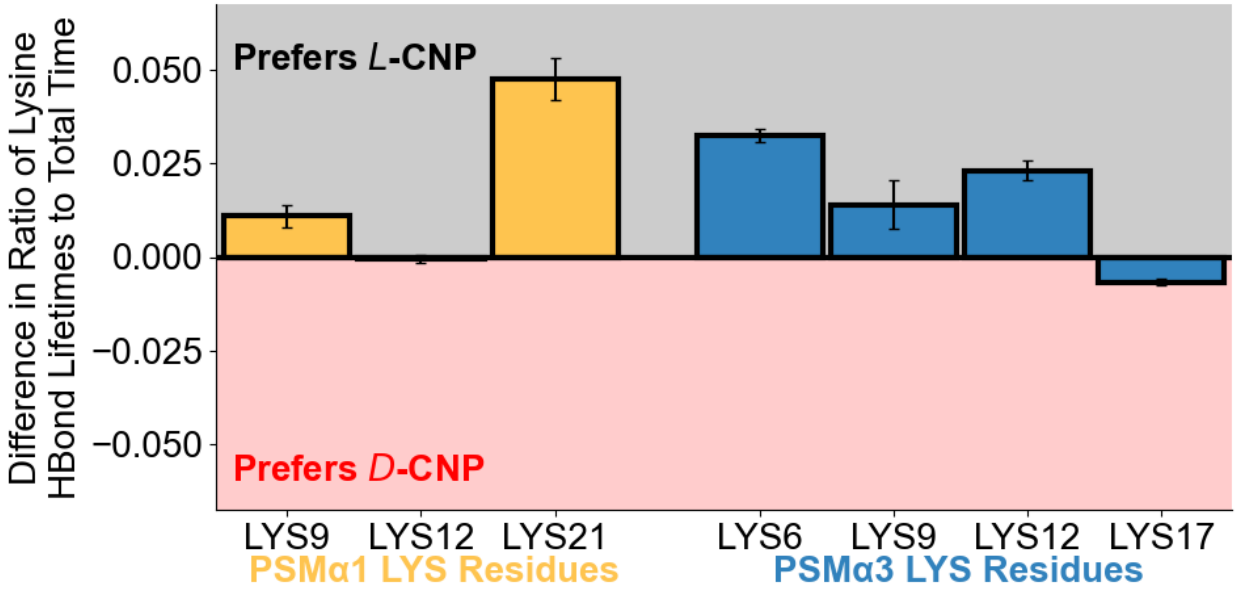

Figure 5.2: **Difference in Lysine Hydrogen Bond Lifetimes of PSMs to CNPs.** Data is collected from **group** simulations. Error bars are standard errors of the mean, taken at 5 ns intervals of the trajectory. All hydrogen bond lifetimes are positive and have been normalized by the 5 ns of total simulation time.

D-CNP with an average lifetime of 13.4± 4.3 ps and 3.7± 0.6 ps, respectively. These lifetimes are remarkably longer than the ones observed for PSMα3/*L*-CNP (0.12± 0.01 ps and 0.09± 0.01 ps), suggesting that, for PSMα3, the short-lived interactions of the LYS groups are compensated with longer lived ASN h-bonds. Both these types of residues play an important role in the structure and functionality of these peptides. PSMs' LYS residues have been shown to be essential for protein stability and interactions with other molecules[191]. Post-translational modification of LYS residues significantly enhances protein aggregation, including into amyloid fibers, through a mechanism that involves the PTM shielding the positive charge of the LYS residue, decreasing electrostatic repulsive forces, and promoting aggregation[192]. Lysine residues are also responsible for the inter-protofilament salt-bridge interactions of PSM amyloid fibers[28]. ASN21 and ASN22 have been shown to be important in the recognition of PSMα3 during the FRP2-mediated proinflammatory response.

CNPs seed PSM aggregation. We observe that not only do the PSMs aggregate on the CNP, but this aggregation seeds further clustering of PSMs. We observe only up to 4 layers, with outer layers sometimes composed of a single peptide. Still, this process could be even more prominent, as peptide deposition on layers and layer reorganization happens on a longer timescale than the one simulated here. While the aggregation and seeding are observed for all the systems (see Figure 5.3), the PSMα3/*L*-CNP aggregate is the only system that forms two stable layers, while the other systems have four. This difference is more significant when considering that more PSMα3 aggregates around *L*-CNP (all 15 peptides) compared to the 9 that aggregate on *D*-CNP, suggesting that *L*-CNP could not only bind PSMα3 strongly, but thanks to the number of H-bonds distributed along the length of the peptide (see previous paragraph), favor a better spatial organization that leads to a more efficient clustering. This effect is not observed for the PSMα1/*L*-CNP aggregate, likely because the long-lived H-bond is more localized towards the end of the peptide, allowing higher configurational freedom that results in a more disorganized assembly as indirectly shown by more spread distribution of peptides (see Figure 5.3d). A more quantitative description of the differences between the orientations of the peptides cannot be surmised from the simulations performed here. Nevertheless, it is worth noting that the aggregation is generally quite disorganized, with peptides aggregating with respect to the CNP surface in a variety of orientations, as shown in Figure C C.1.

CNPs affect PSMs' secondary structure. The generally wider distribution of distances for PSMα1 is also due to the change in secondary structure caused by the interaction with the CNP. While all PSMs show some loss of -helical secondary structure when interacting with CNP (first layer), compared to when they are solvated in water, this change is almost negligible for PSMα3. For both PSMs, we observe that the slight loss of -helix corresponds to a roughly equal increase in random coil and β-sheet, independently of the CNP chirality; however, we observe a much more relevant loss of the -helical secondary structure with both CNPs for PSMα1. Moreover, for PSMα1, this change results primarily

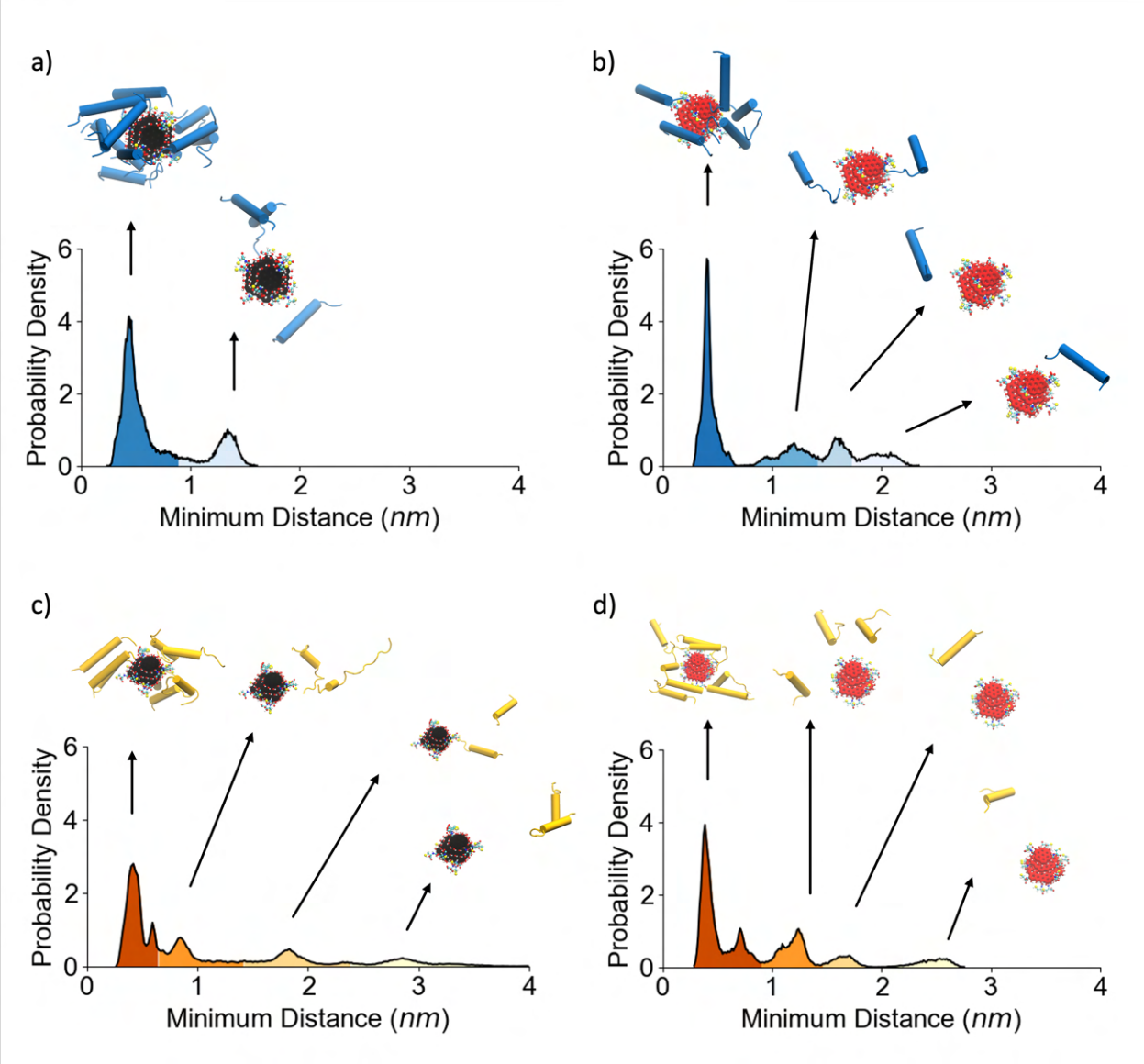

Figure 5.3: **CNPs seed the formation of PSM aggregates.** (a-b) PSMα1 (yellow palette) aggregating around (a) *L*-CNP (red) and (b) *D*-CNP (black). (c-d) PSMα3 (blue palette) aggregating around (c) *L*-CNP (red) and (d) *D*-CNP (black). The distributions are collected during the **group** simulations, where the minimum distance is taken between each amino acid on the PSM and non-hydrogen atoms on the surface of the CNP.

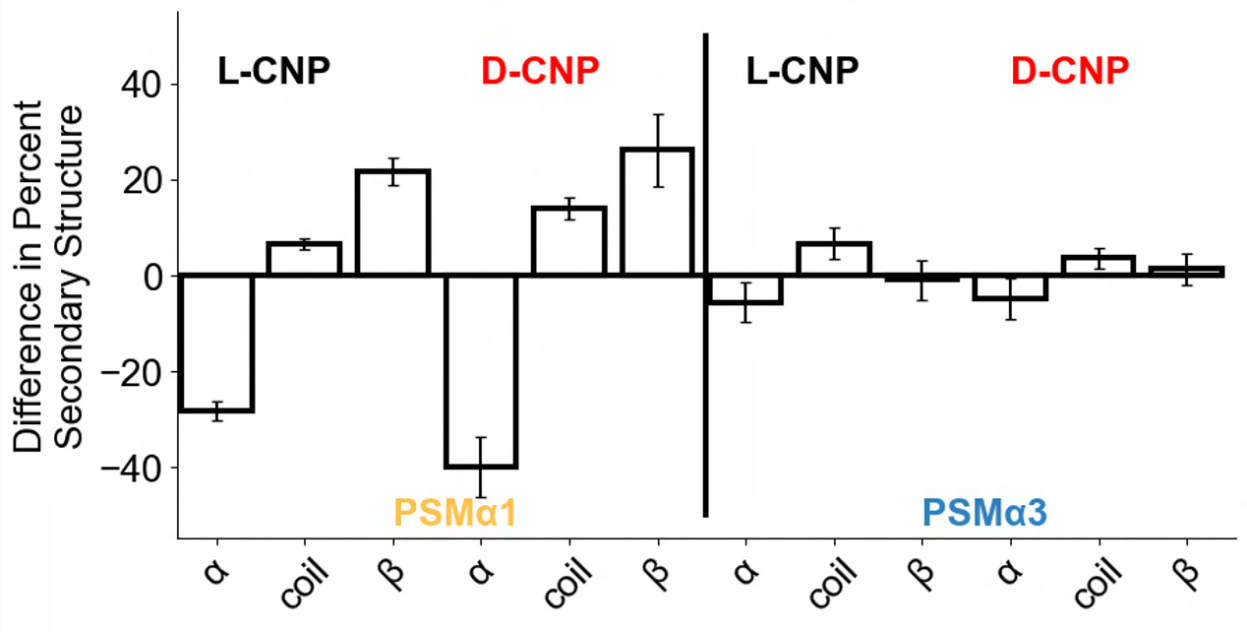

Figure 5.4: **Change in structure of PSMs due to interactions with CNP.** Bars show the difference in secondary structure compared to the solvated peptides as sampled in the **single** PSM simulations. Error bars are standard errors of the mean. Negative values indicate a reduction in the secondary structure interacting with CNPs.

in an increase of β-sheet and some random coil secondary structure. This difference between the peptides is likely due to the higher stability of the PSMα1 β-aggregates[28], and is likely responsible for the observed differences in the structure of the additional peptide layers, as discussed above.

5.1.3.2 Chiral Separation of CNPs

D-CNP eluted slower than *L*-CNP (Table 5.1.3.2) in the chiral column. The longer retention time of *D*-CNP suggests that chiral ligands at the surface of the CNPs are the primary mechanism for enantioselective separation through polar ionic interactions. Biased molecular dynamics (MD) simulations were employed using unbound teicoplanin to study its interaction with chiral CNPs (Figure 5.5a). Two simplified models were created to mimic the chromatographic conditions, one for teicoplanin with chiral NPs made from two cysteine

Table 5.1: **Affinity of Chiral CNPs for Teicoplanin.** Experimental retention times, collected from experiments performed by Misché Hubbard, of CNPs in the column and computational binding free energy from simulations are shown. A longer retention time indicates higher affinity of the *D*-CNP for teicoplanin; a negative binding free energy also points to *D*-CNP having a higher affinity for teicoplanin. Errors are standard deviations.

System	Retention Time (min)	ΔA (kcal/mol)
***L*-CNP**	0.795 ± 0.046	0.35 ± 0.51
***D*-CNP**	0.961 ± 0.022	-1.95 ± 0.64

enantiomers. Metadynamics simulations were performed to determine the binding free energy for teicoplanin with *L*- and *D*-CNP, which were found to be 0.35 ± 0.51 and -1.95 ± 0.64, respectively (Table 5.1.3.2), where the error represents the standard deviation. The higher binding energy for the teicoplanin/*L*-CNP system indicates a weaker or unfavorable interaction. Interestingly, *L*-CNP was observed to become warped in close proximity to teicoplanin (Figure 5.5c), and the center of mass distance between teicoplanin's binding region and the *L*-CNP was found to be larger than for the *D*-CNP when they interacted. This observation provides a possible explanation for the difference in affinity (Table 5.1.3.2), as teicoplanin's binding region orients itself closer to the *D*-CNP (Figure 5.5b). Overall, the MD simulations demonstrated a higher binding affinity between teicoplanin and *D*-CNP, consistent with the elution order observed in experiments. This suggests that MD simulations can be powerful tools for understanding the interactions of chiral NPs and chiral selectors, and can be used to screen multiple parameters to identify suitable conditions for enhanced resolution between enantiomers.

5.1.3.3 Conclusions

The interaction between PSMs and chiral, cysteine-based CNPs was elucidated, revealing significant implications for biomedical applications. In practical applications, these chiral CNPs have been shown to selectively disassemble amyloid-rich *S. aureus* biofilms; *L*-CNPs, in particular, exhibit lower anti-biofilm activity than *D*-CNPs, perhaps, due to their ability to

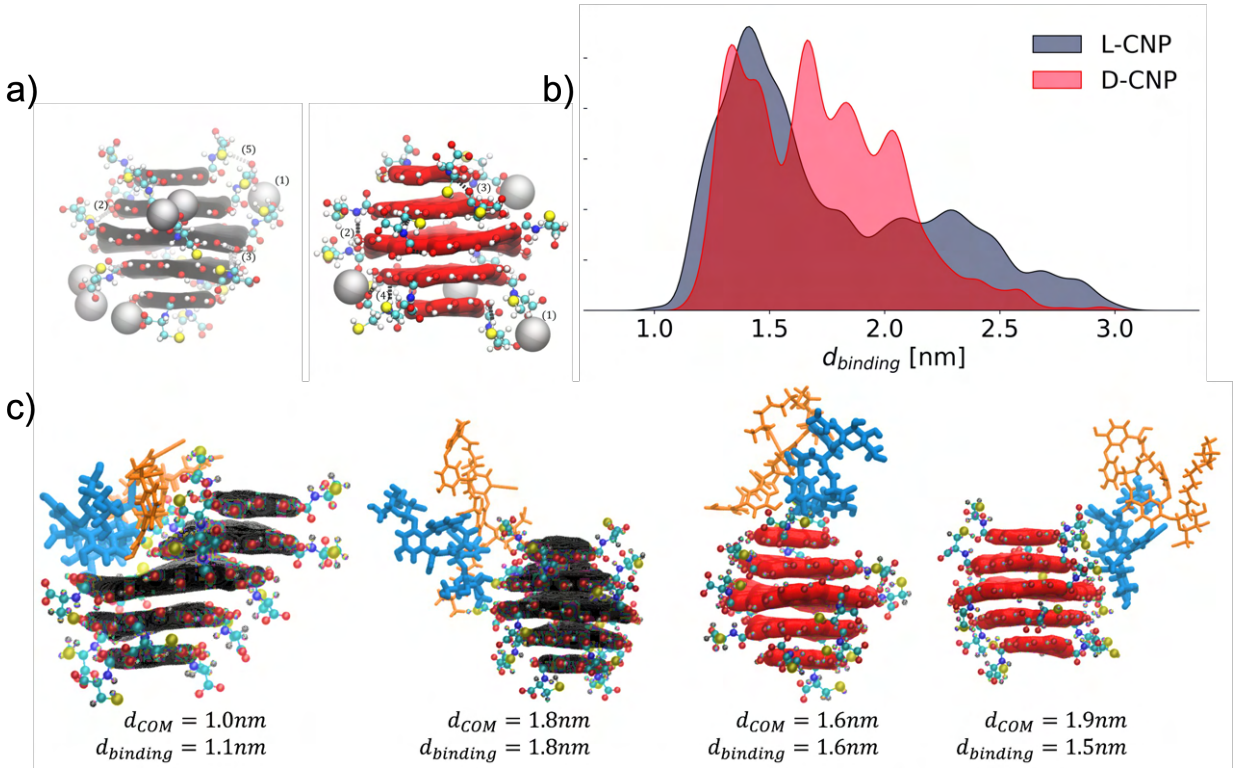

Figure 5.5: **Chiral Separation of Chiral CNPs by Teicoplanin.** (a) Structure of the *L*-CNP (left) and *D*-CNP (right) CNP in water. Electrostatic repulsion due to dissociated carboxylic groups is mitigated (1) by Na+ ions (silver spheres) and (2-5) by intermolecular hydrogen bonds. (b) $d_{binding}$, the distance between the COM of TEIC binding region and COM of each CNP, distributions illustrate a higher probability that the binding region of teicoplanin is closer to the *D*-CNP than to the *L*-CNP. (c) Chiral CNPs interacting with teicoplanin. Teicoplanin (orange and blue), teicoplanin binding region (blue), *D*-CNP (red), and *L*-CNP (black)

selectively interact with LYS residues. Also, *D*-CNP instigates a greater loss of the α-helical secondary structure of PSMα1. The chiral CNPs were separated using high-performance liquid chromatography (HPLC), which demonstrated the presence of chiral centers on their surface, crucial for interactions with cellular membranes and biomacromolecules. Furthermore, the separation of *L*- and *D*-CNPs using teicoplanin stationary phase HPLC columns indicates that not only are they chirally stable, but they are, also, resistant to reverting to their cysteine precursors. Combined, these findings underscore the promise of CNPs as an anti-biofilm platform, with the potential for tailored applications in combating bacterial infections.

CHAPTER 6

Conclusions

My research has explored PSMα1 functional amyloid aggregation[28], cellular membrane vibrations[38], and chiral CNPs as antimicrobial agents[55].

6.1 Impact

Alone, the work presented in the PSMα1 functional amyloid publication[28] and Chapter 3 is a groundbreaking computational study, where, for the first time, we demonstrate that we can observe the preference of PSMα1 amyloid fibers for β-sheet, rather than α-helical, aggregates computationally with molecular dynamics simulations. We, also, explain the lateral aggregation mechanism of the fibers with chirality, and the exceptional agreement to experimental results that we achieve in this study suggests that molecular dynamics simulations are an invaluable tool in the characterization of proteinaceous and polymorphic fibers. This has immediate implications in the study of biomolecular structures because, now that we understand their aggregation mechanism and structure in superior detail, we can learn how to prevent their formation, modify or manipulate them, and destroy them using new materials (*e.g.*, chiral carbon nanoparticles in Chapter 5). In the membrane vibrations publication[38] and Chapter 4, we demonstrate that we can detect differences in the mechanical vibrations among membranes with various lipid compositions and in a high-dimensional space with a combination of graph theory and the Kolmogorov-Smirnov Statistic. The

procedure we present can be immediately applied to other structures (*e.g.*, amyloid fibers), as well as to data obtained experimentally; therefore, this work has vast implications in the identification of compounds in a variety of contexts. Furthermore, our study briefly hints at how comparisons could be used to discern correlations between membrane composition and function, even in the face of noisy data. Finally, the work summarized in Chapter 5, including published[55] and unpublished results, can serve as a blueprint for the design of new anti-biofilm compounds. Now that we are cognizant of the importance of chirality in the aggregation of PSMα1 amyloid fibers, as well as the functionalization of carbon nanoparticles and subsequent dissemination of biofilm, we can approach the study of other anti-biofilm compounds with conviction. Using computational techniques, including molecular dynamics simulations, to help explain experimentally observed phenomena in the realm of drug-target interactions is a mutually beneficial partnership I do not see losing its merit anytime soon. If anything, computational drug discovery will become increasingly conventional, but as I will mention in the Future Work section, it can be improved.

Combined, the results of my research, and future work motivated by my research, will make anti-biofilm treatment more affordable and readily available and curb the consequences of bacterial resistance. Currently, there is little incentive for pharmaceutical companies to invest in antibiotic research and development because it is time-consuming, expensive, and rendered obsolete, as antibiotic discovery cannot compete with growing antibiotic resistance. Computationally searching for answers will expedite the process, saving valuable time and money. The implications of this work, however, reach far beyond the clinical envelope. Biofilm flourishes in soil and leaches into the water supply. It is everywhere. Because biofilm affects everyone, on a global scale, this work has the potential to improve the lives of billions of people.

6.2 Future Work

Future work will (1) further characterize the aggregation of amyloid fibers, and (2) explore the development of targeted nanoparticulate compounds that specifically interact with PSM-derived amyloids to disrupt biofilm stability. These future aims, taken together, explore increasingly complex nanosystems relevant to addressing the issue of biofilm manipulation and resilience by applying molecular dynamics simulations, novel computational analysis techniques, and machine learning. In the following subsections, I explore the future of research in both of these areas.

6.2.1 Amyloid Fiber Characterization

We can build upon the computational amyloid fiber characterization performed in this thesis by investigating two aspects of fiber formation in more detail: the evolution of fiber structure over time (which includes oligomers, eDNA, polymorphs, and α to β transition) and the environment of the biofilm.

6.2.1.1 Evolution of Fiber Structure

The study of the aggregation of proteinaceous amyloid fiber subunits into larger and larger oligomers before becoming fibers is essential, as oligomers of amyloid-forming proteins, including PSM peptides, have been identified to possess enhanced toxicity compared to their monomeric forms[14]. Computational research could focus on simulating the initial stages of oligomer formation, employing molecular dynamics simulations to observe the conditions under which oligomers form and identify the structural features that contribute to their increased pathogenicity. This information could be used to design drugs or anti-biofilm compounds that inhibit oligomerization, potentially mitigating the toxicity of bacterial infections. Such observations could even have implications for amyloid-induced diseases, like Alzheimer's and Parkinson's.

Since amyloid fibers undergo small, but detectable, changes for about 2 weeks, the slow

evolution process of fibers formed in solution, as opposed to their relatively quick formation *in vitro* and *in vivo*, could be a consequence of other constituents in the ECM (*e.g.*, eDNA)[4]. Since we know that amyloid fiber formation is bolstered by seeding and undergoes a rate-limiting nucleation phase, eDNA might have a hand in initiating, the aggregation process[108]. eDNA might, also, template the chirality of the fiber by hindering additional lateral growth or expediting the recovery when any disaggregation occurs. eDNA plays a critical role in the stabilization and maturation of biofilms, acting as a scaffold that supports the aggregation of PSM fibers. Thus, understanding the interaction between eDNA and PSM peptides could reveal targets for disrupting biofilm integrity. Though developing a coarse-grained approach is probably necessary as the system of eDNA and fiber becomes increasingly convoluted, computational studies can model these interactions, exploring the interactive forces and binding affinities between eDNA and PSMs. On a similar note, the α-helical peptide to β-sheet secondary-structure transition is, also, a fundamental stage in the formation of functional amyloids. This conformational change is associated with the maturation of fibers and their functional properties, and could, also, be a bottleneck in fiber maturation. Advanced computational techniques, such as enhanced sampling methods, can be utilized to study the free energy barriers associated with this transition. By capturing the detailed pathway of this conformational change, researchers can identify critical intermediate states that may serve as potential targets for therapeutic intervention, aiming to halt or reverse the amyloid formation process.

Last but not least on the subject of fiber evolution is the acknowledgement of polymorphs. Polymorphs represent the diverse structural variants that PSM fibers can adopt, whether it be a local deviation in the secondary structure or the number of protofilaments, and are an innate consequence of how the fibers form. Different polymorphic forms can have distinct biological properties, influencing the pathogenicity and stability of biofilms[108,120]. By understanding the polymorphic landscape, it becomes possible to predict and potentially control the formation of less harmful or more easily disruptable biofilm structures. Compu-

tational methods like free energy calculations can be applied to study the stability of various polymorphs and their propensity to form under different environmental conditions.

6.2.1.2 Environment of the Biofilm

While most of our knowledge about microbial biofilms comes from those formed at liquid-solid interfaces, it is crucial to understand biofilms at gas-solid interfaces, which have a profound impact on human health[193]. Biofilms formed at gas-solid interfaces, like hospital surfaces and food contact surfaces, can cause material degradation, deterioration, and potential health risks[194,195]. Studying these biofilms is challenging due to their unique characteristics, including low resource availability, low biomass, and low growth; therefore, gaining insights into the chemical, physical, and biological attributes of these environmental films and their ecological succession over time and space is essential for material design, control features, functionalized materials, and synthetic biology.

The identification and analysis of essential biological matrix components, such as proteins, carbohydrates, eDNA, and phage, are crucial for understanding the formation and maintenance of surface films. First, computational techniques, such as MD simulations, can be employed to generate accurate nanoscale assemblies of ECM constituents and explore their interactions with various bacterial structures. Then, coarse-grained (CG) models can be developed based on the atomistic descriptions, allowing the representation of larger-scale biomolecules and conformational changes. Extending the scale of molecular simulations from atomistic to mesoscopic levels could provide a deeper understanding of the behavior and properties of biofilm components. By combining MD simulations with machine learning (ML) approaches[196], the probability and location of nanoscale interactions can be estimated, providing valuable insights into the formation and stability of biofilms in various environments.

6.2.2 Disrupting Biofilms with Nanoparticles

The advent of machine-learning tools for predicting protein-nanoparticle interactions, like NeCLAS developed by Saldinger *et al.*, presents a promising frontier for the speedy prediction and identification of innovative antibacterial therapies. Because there are many other nanoparticles, besides carbon nanoparticles, that could be potential drug candidates (*e.g.*, zinc oxide nanoparticles[197,198] and gold nanoparticles[199–201]), machine learning can be used to predict potential binding sites and interaction strengths between different nanoparticles and their suggested targets. Knowing the drug target in a multi-, whole-cell biofilm or bacterial colony is challenging because of experimental microscopy limitations[202]. Regardless, understanding the mechanism of action of the drug is critical not only to optimize the drug's efficacy and safety profile, but also to anticipate how resistance will, inevitably, develop, which is crucial for the continued effectiveness of the drug. In the interest of mitigating bacterial resistance, it's worth noting that multidrug-tolerant persister cells (or bacteria with a low metabolic state) are often the culprits behind chronic and relapsing infections[203–206], so it would be shrewd to consider probing the effectiveness of drug candidates against persister cells to avoid triggering the development of new antimicrobial resistance mechanisms, or at least not as quickly.

Significant strides can be made in the development of targeted antibacterial therapies, with careful application and a judicious combination of machine learning and molecular dynamics simulations. Machine-learning predictions will streamline the setup of molecular dynamics simulations, allowing us to focus on the most promising interaction regions and apply a minimal bias to drive the system toward these sites. Then, unbiased molecular dynamics simulations will confirm the stability of the nanoparticle-protein complexes and allow for the quantification of any conformational and dynamic changes that result from the interaction. Nonetheless, acknowledging there are pitfalls inherent to machine-learning predictions (*e.g.*, uncommon mechanisms of interaction may evade detection because they lacked representation in the training set), more computationally demanding enhanced sam-

pling techniques to ensure a comprehensive exploration of the phase space may be necessary. This protocol can serve as a foundation for future medicinal chemistry efforts to refine the search for antimicrobial candidates, carrying with that the potential to revolutionize the treatment of bacterial infections by rapidly scanning a vast array of nanoparticulate drug candidates and significantly accelerating the drug discovery process.

APPENDICES

APPENDIX A

PSMα1

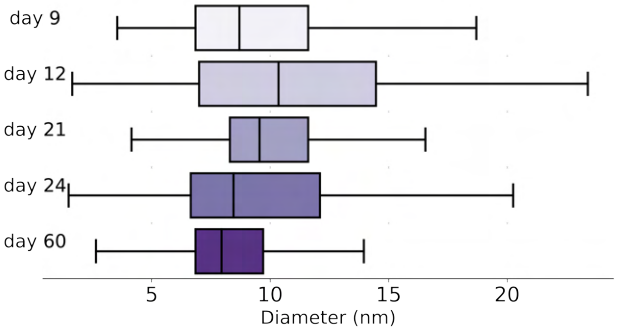

Figure A.1: **Evolution of the diameter of PSMα1 fibers** computed from TEM images. The distributions are generally multi-modal: the boxes represent first and third quartiles of the dataset and the middle line represents the median; whiskers show the rest of the distribution.

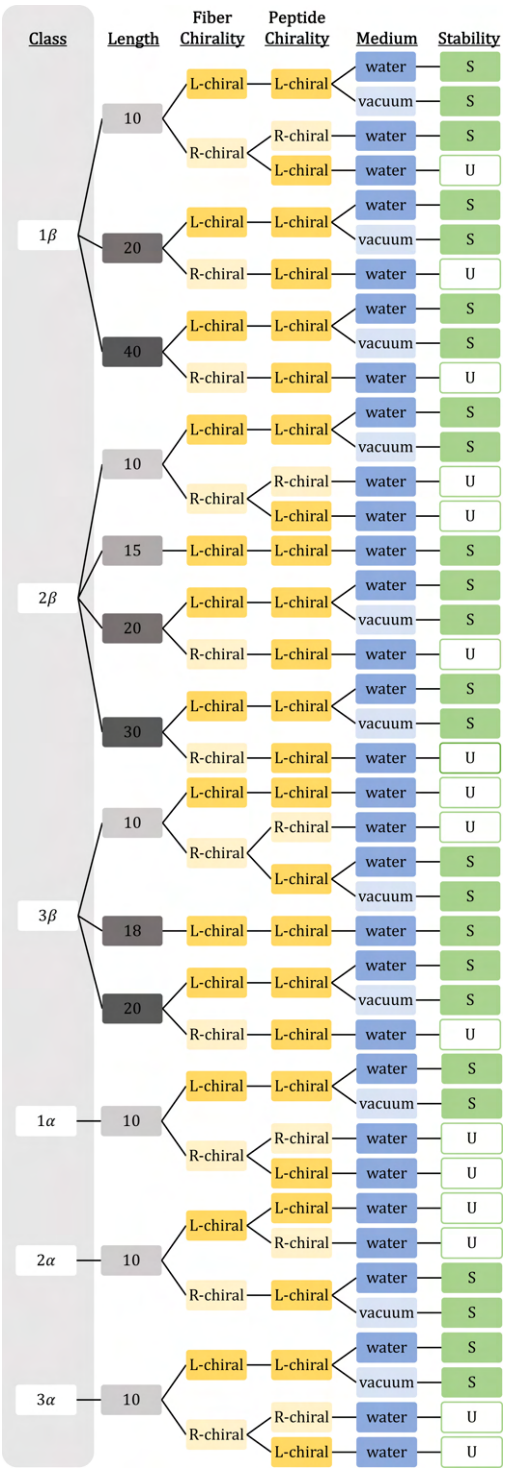

Figure A.2: **Stability of the PSMα1 aggregates** in all the simulated systems. S for stable, U for unstable.

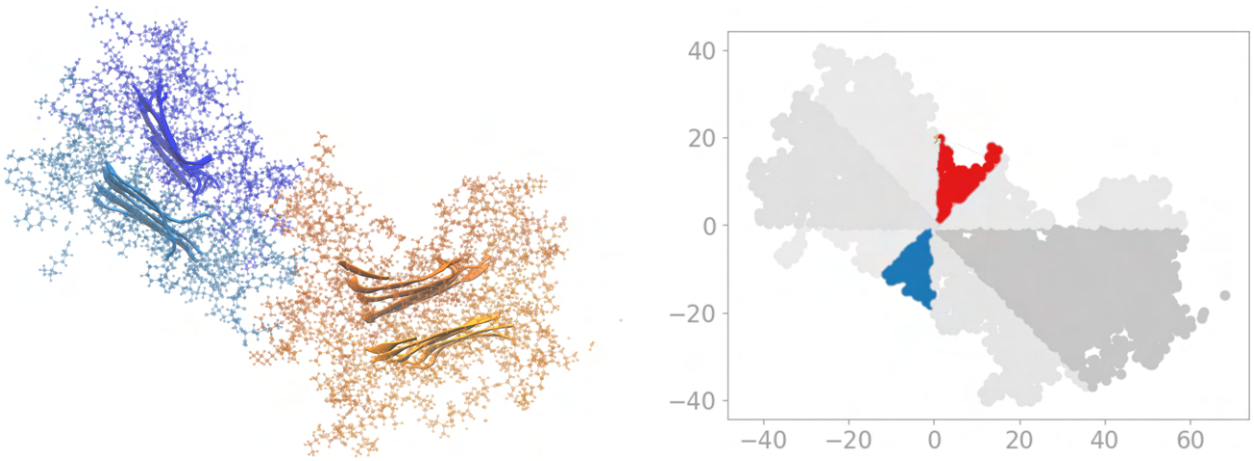

Figure A.3: **Contribution to the diameter distribution** computed from MD simulations. Diameters smaller than 5 nm appear at inter-protofilament regions, where there is a lower atom density and smaller diameter. In this snapshot of the $2\beta_{20}$ fiber, diameters smaller than 5 nm (colored) are detected in the middle slice. Coordinates of atoms (right panel) in each slice are represented in angstrom.

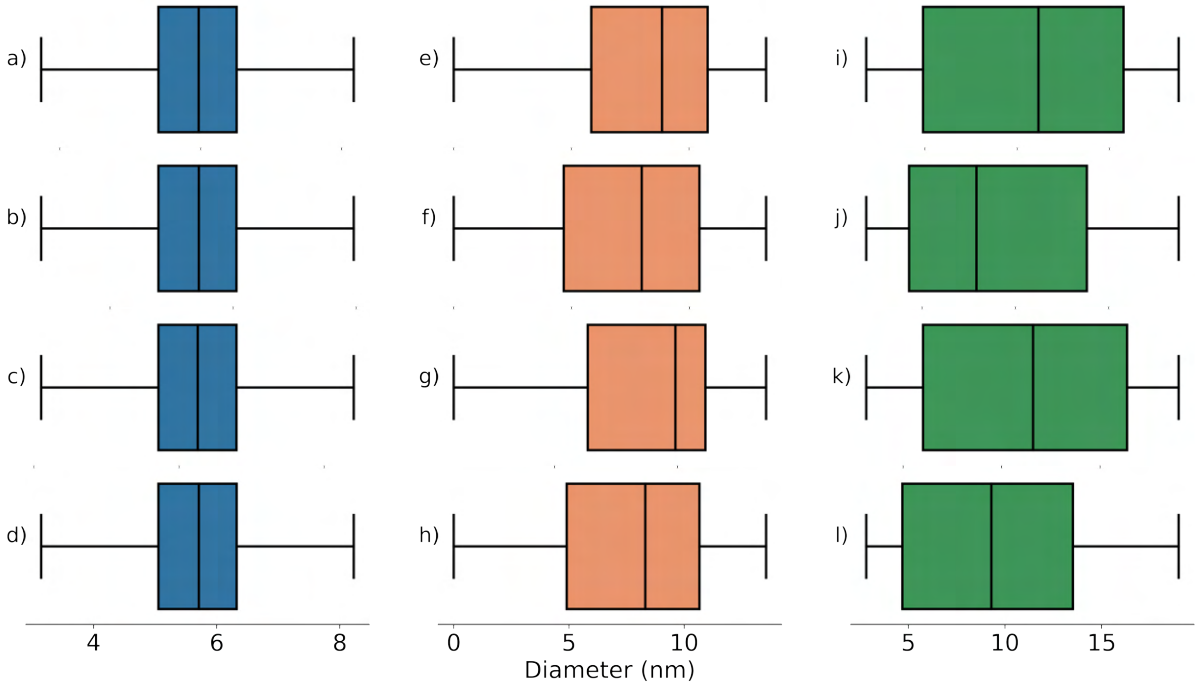

Figure A.4: **Diameter Parameter Selection** does not significantly influence the average, nor the overall shape of the diameter distribution. Shown are diameter distributions for $1\beta_{40}$ with (a) slice height of 1.5 nm and 8 sectors, (b) slice height of 1.5 nm and 20 sectors, (c) slice height of 2.5 nm and 8 sectors, and (d) slice height of 2.5 nm and 20 sectors; $2\beta_{20}$ with (e) slice height of 1.5 nm and 8 sectors, (f) slice height of 1.5 nm and 16 sectors, (g) slice height of 2.5 nm and 8 sectors, and (h) slice height of 2.5 nm and 16 sectors; and $3\beta_{20}$ with (i) slice height of 1.5 nm and 8 sectors, (j) slice height of 1.5 nm and 20 sectors, (k) slice height of 4.0 nm and 8 sectors, and (l) slice height of 4.0 nm and 20 sectors.

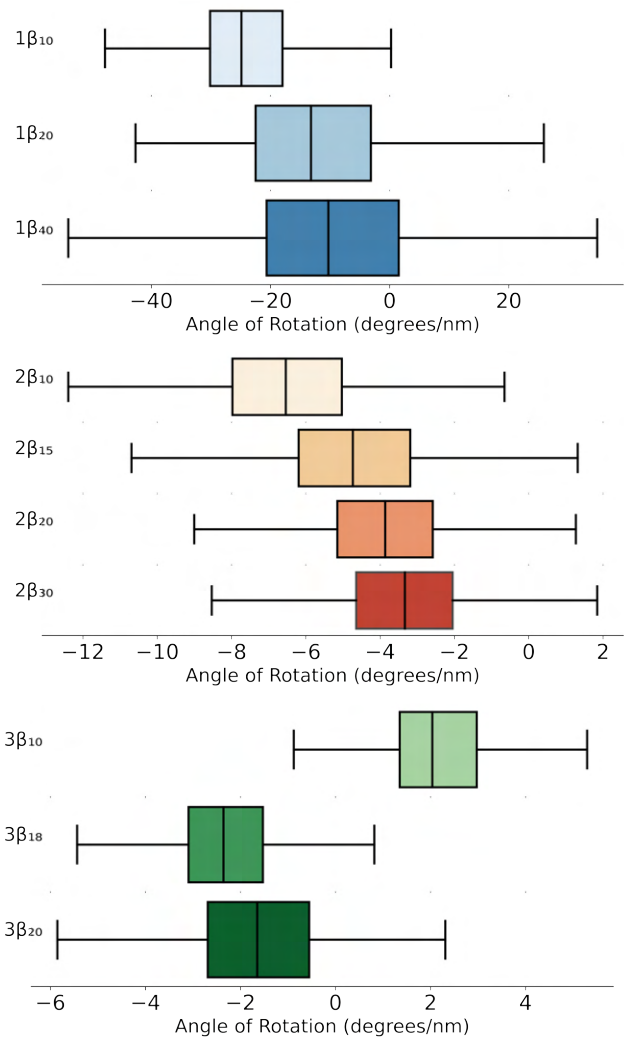

Figure A.5: **Angles of Rotation vs. Fiber Length** boxplots The distributions are generally not multi-modal: the boxes represent first and third quartiles of the dataset and the middle line represents the median; whiskers show the rest of the distribution. Averages are unweighted.

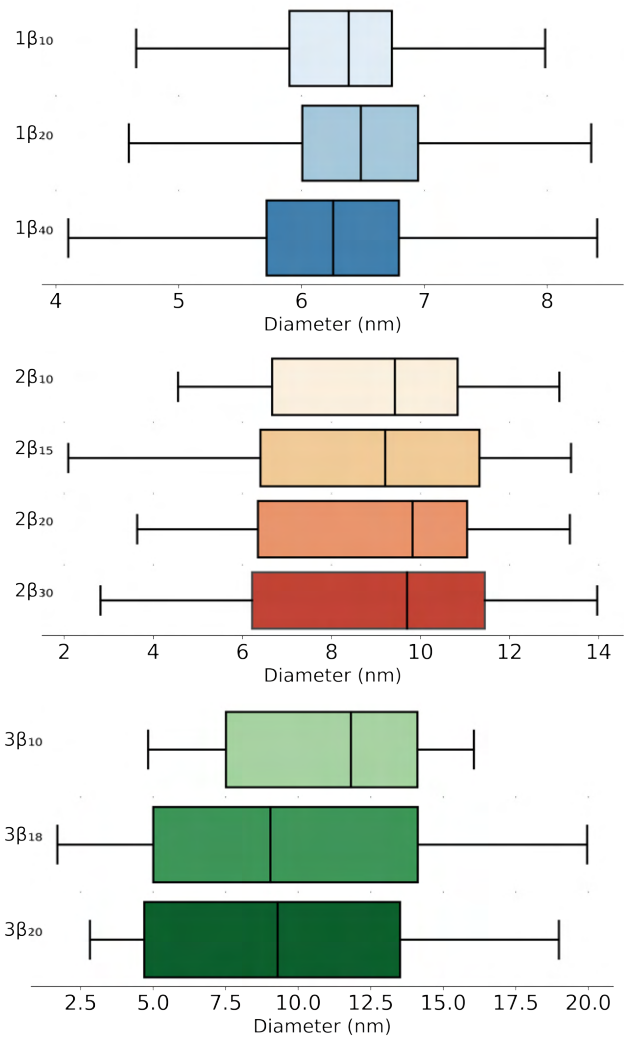

Figure A.6: **Diameter vs. Fiber Length** for 1-protofilament (left), 2-protofilament (middle), and 3-protofilament (right) MD fibers simulations. The distributions are generally multi-modal: the boxes represent first and third quartiles of the dataset and the middle line represents the median; whiskers show the rest of the distribution.

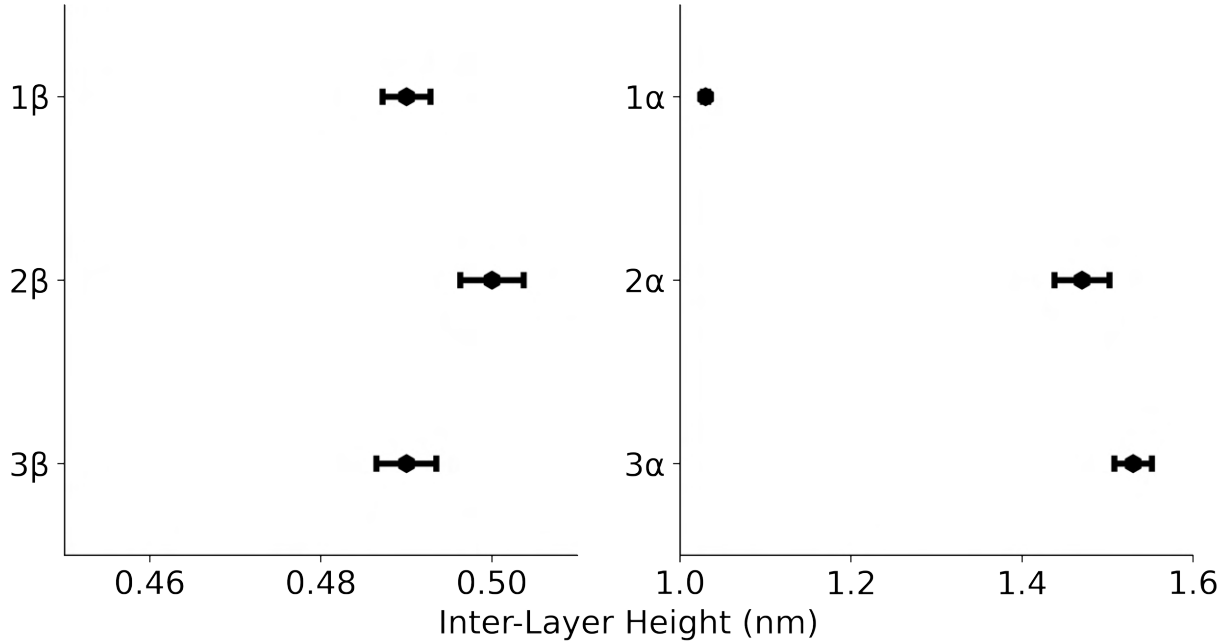

Figure A.7: **Inter-Layer Distance** in nm for simulated nanofibers.

Table A.1: **Fiber Diameter Statistics** (in nm) from TEM day-by-day images. Seven-figure summary is reported as percentiles.

Day	***Percentile***						
	0^{th}	10^{th}	25^{th}	50^{th}	75^{th}	90^{th}	100^{th}
9	3.550	6.100	6.850	8.700	11.60	17.50	25.75
12	1.650	5.375	7.000	10.35	14.48	17.70	23.40
21	4.150	7.600	8.300	9.550	11.60	14.10	23.85
24	1.500	5.650	6.650	8.450	12.10	15.55	24.90
60	1.650	5.900	6.850	7.950	9.700	12.55	26.20
Averages							
Forming Fiber	1.650	5.950	6.850	9.000	12.50	17.60	25.75
Mature Fiber	1.500	6.450	7.600	8.900	11.00	13.90	26.20

Day	**Average**	**Standard Error**	**Samples**
9	10.10	0.0014	3131
12	10.96	0.0053	852
21	10.28	0.0001	24324
24	9.690	0.0009	4500
60	8.830	0.0002	17035
Averages			
Forming Fiber	10.28	0.0011	3983
Mature Fiber	9.690	0.0200	45859

Table A.2: **Fiber Diameter Statistics** (in nm) for simulated PSMα1 fibers. The seven-figure summary is reported as percentiles. $^{(v)}$ for vacuum simulations; unmarked simulations are in 0.15 M NaCl solution.

System	***Percentile***							**Average**
	0^{th}	10^{th}	25^{th}	50^{th}	75^{th}	90^{th}	100^{th}	
$1\beta_{40}$	3.632	5.204	5.715	6.258	6.792	7.242	9.155	6.250
$1\beta_{40}^{(v)}$	3.211	4.433	5.0635	5.534	5.862	6.402	7.847	5.480
$2\beta_{30}$	2.813	4.802	6.220	9.696	11.442	12.096	13.965	9.03
$2\beta_{30}^{(v)}$	3.912	4.396	5.659	8.623	10.21	10.900	11.26	8.010
$3\beta_{20}$	2.818	4.118	4.692	9.2915	13.511	16.604	18.986	9.460
$3\beta_{20}^{(v)}$	2.334	3.115	3.571	4.7245	8.943	13.342	16.315	6.51
$1\alpha_{10}$	1.845	2.899	3.231	3.661	4.072	4.511	5.763	3.68
$2\alpha_{10}$	3.220	4.265	4.565	5.019	5.497	5.841	7.029	5.04
$3\alpha_{10}$	2.350	3.871	4.440	5.523	6.349	7.107	9.116	5.46
AFM	1.230	8.607	9.697	11.74	14.23	18.36	29.99	12.52

Table A.3: **Half Helical Periodicity Statistics** (in nm) from simulations and AFM images. The seven-figure summary is reported as percentiles. All systems are in 0.15 M NaCl solution.

System	***Percentile***						
	0^{th}	10^{th}	25^{th}	50^{th}	75^{th}	90^{th}	100^{th}
$1\beta_{40}$	2.694	5.328	6.990	11.38	17.85	27.16	47.52
$2\beta_{30}$	17.43	29.72	36.68	48.78	67.63	92.47	137.6
$3\beta_{20}$	30.39	49.65	60.62	82.27	125.4	184.6	290.5
AFM	8.864	14.90	22.68	36.02	50.88	62.53	86.43

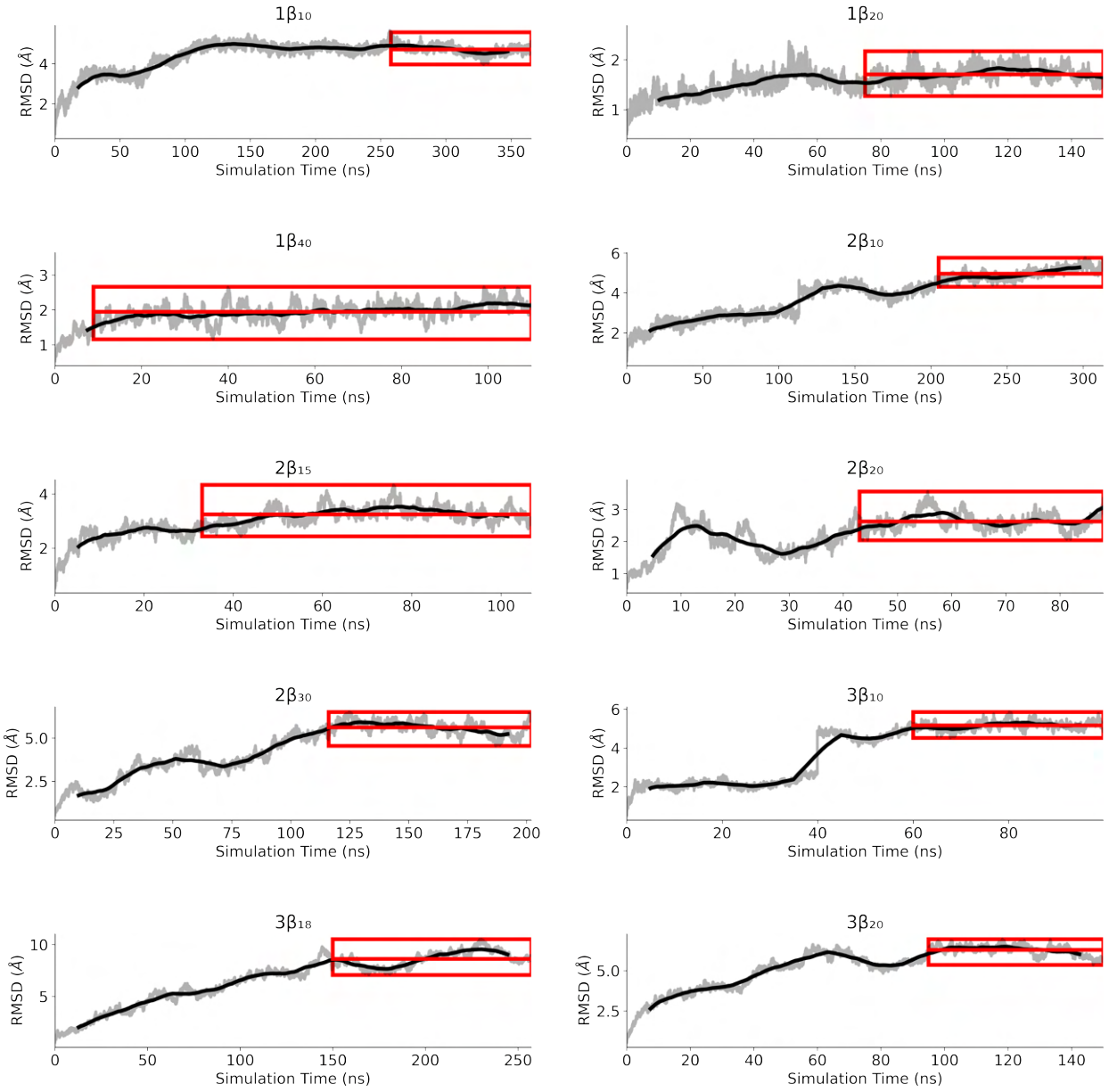

Figure A.8: **RMSDs for β-sheet fibers in water** show converged and stable systems. The faint gray line is unaltered RMSD, the black line is the moving average of RMSD. The red region demonstrates from where production data was taken, where the upper line is the maximum RMSD of that region, the lower line is the minimum, and the middle line is the average.

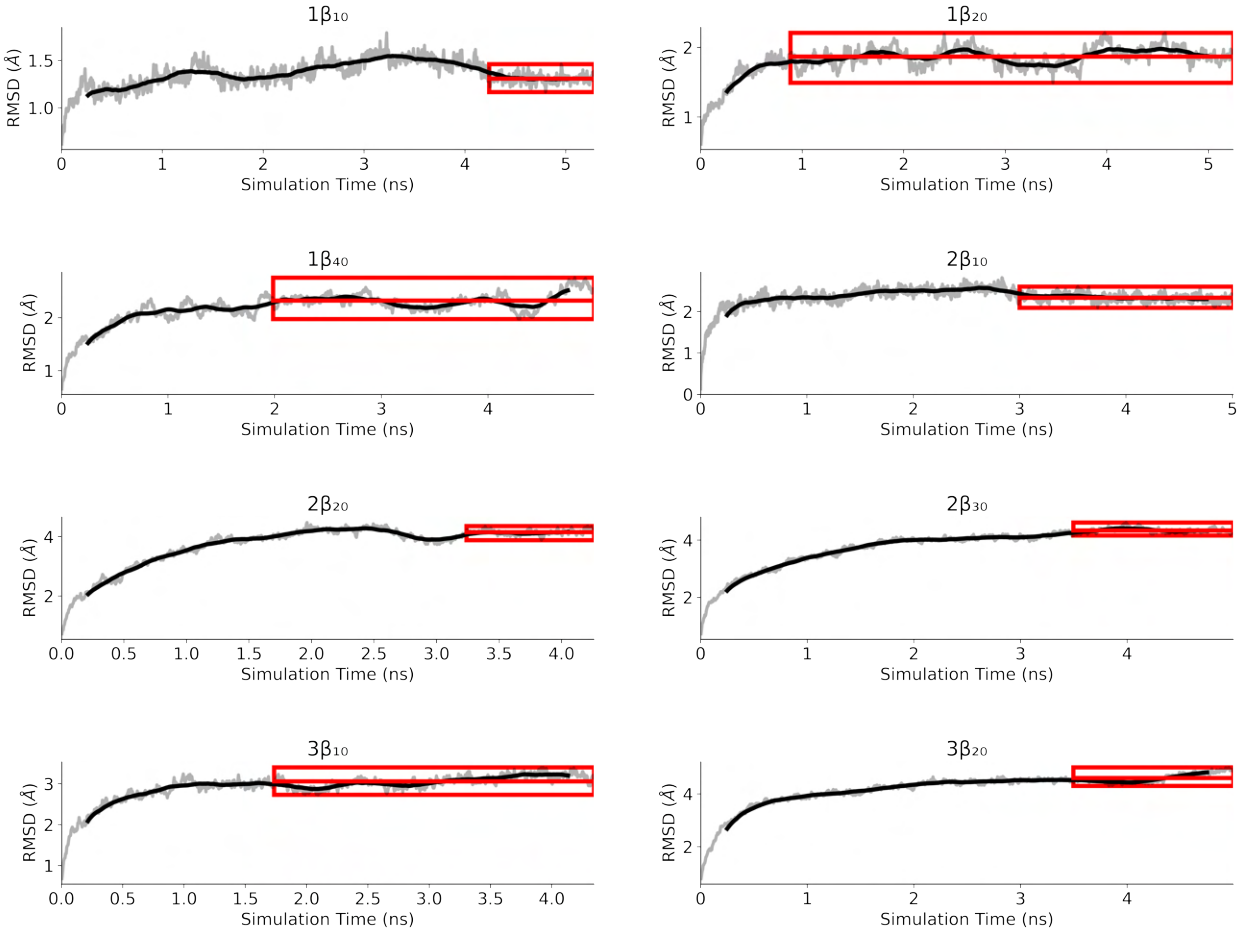

Figure A.9: **RMSDs for β-sheet fibers in vacuum** show converged and stable systems. The faint gray line is unaltered RMSD, the black line is the moving average of RMSD. The red region demonstrates from where production data was taken, where the upper line is the maximum RMSD of that region, the lower line is the minimum, and the middle line is the average.

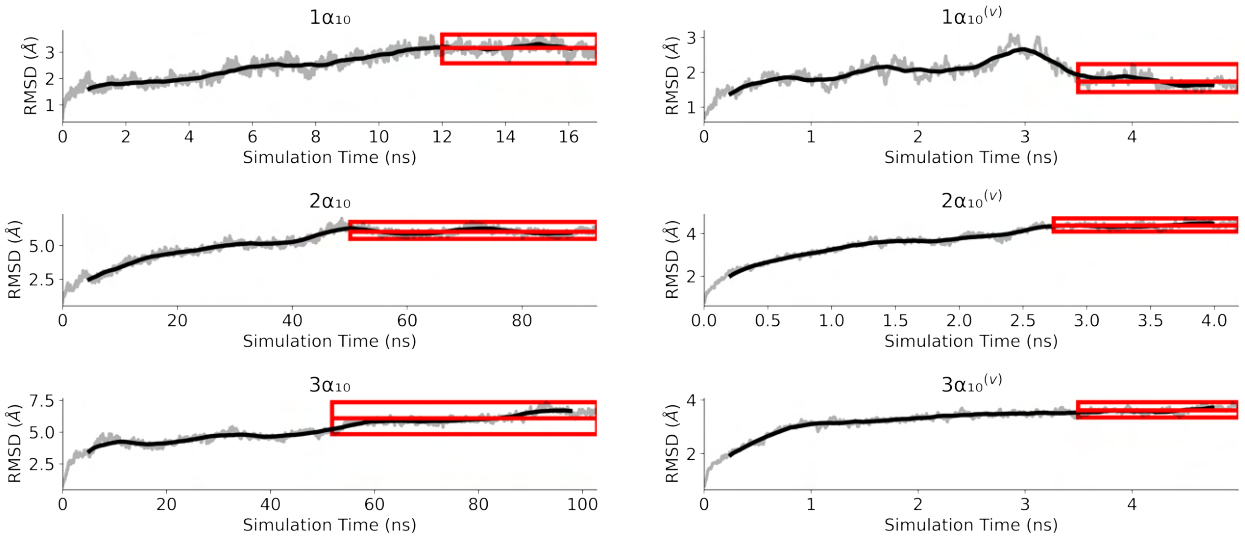

Figure A.10: **RMSDs for α-helical sheet fibers** in water and in vacuum ($^{(v)}$) shows converged and stable systems. The faint gray line is unaltered RMSD, the black line is a moving average of RMSD. The red region demonstrates from where production data was taken, where the upper line is the maximum RMSD of that region, the lower line is the minimum, and the middle line is the average.

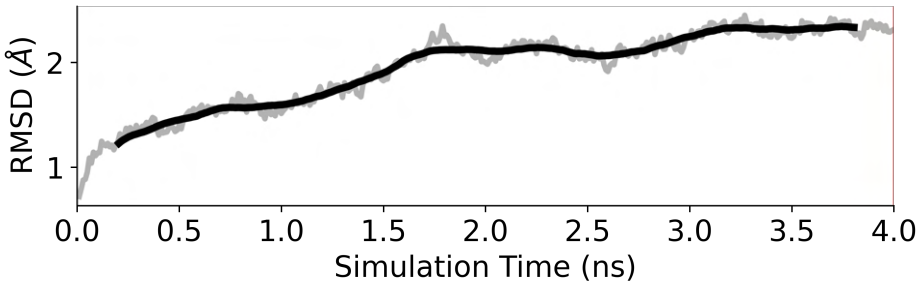

Figure A.11: **RMSD for mirrored $1\beta_{10}$ fiber** shows converged and stable system. The faint gray line is unaltered RMSD, and the black line is the moving average of RMSD.

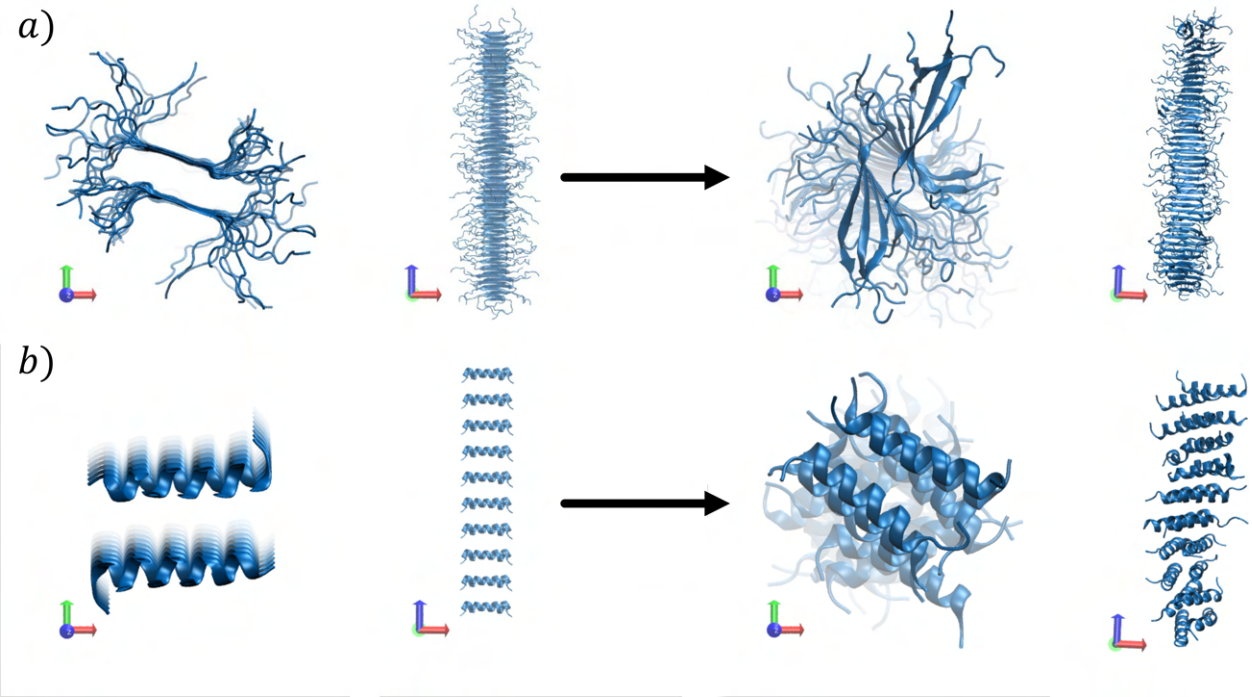

Figure A.12: **Initial (left of arrows) and final structures (right of arrows)** of $1\beta_{40}$ (a), and $1\alpha_{10}$ (b) model nanofibers. Initial structures begin with crystal-like topology and evolve to helical final structure. Axes colors in the bottom left of each snapshot can be identified as blue for z-axis, green for y-axis, and red for x-axis.

APPENDIX B

Membranes

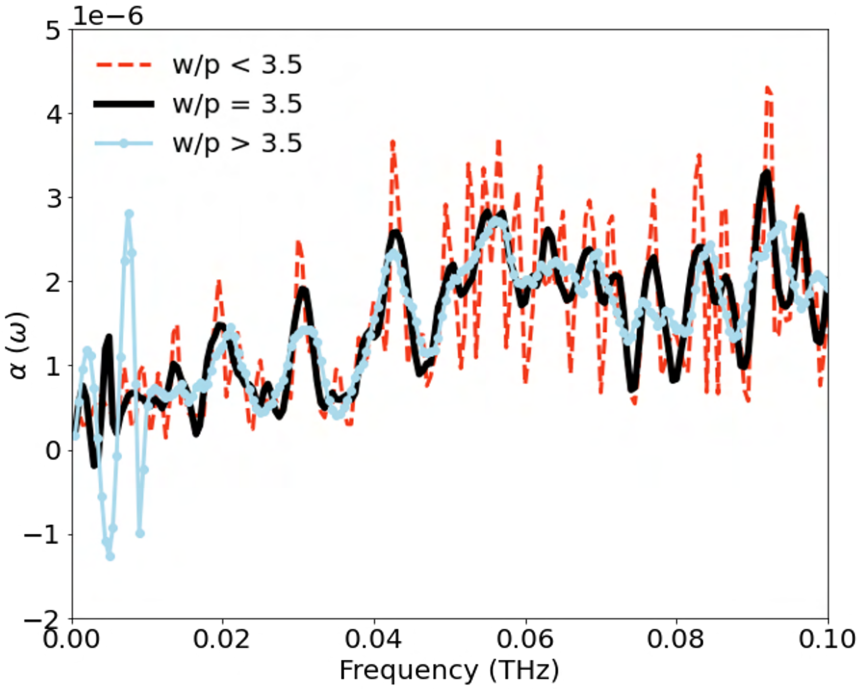

Figure B.1: **Savitsky-Golay Filter Selection.** Savitsky-Golay Parameter Selection Demo shows why we chose a ratio between window and polynomial order of 3.5 (solid, black line) to filter our data. Data in this figure is not normalized.

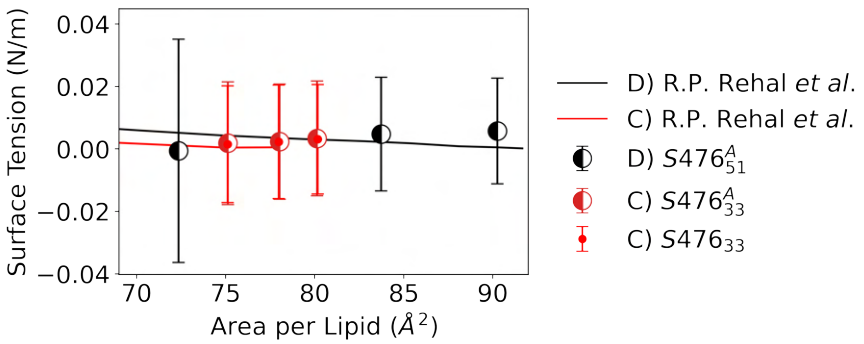

Figure B.2: **Langmuir Isotherms.** Langmuir Isotherms for *S. aureus* membranes studied in this paper and in Rehal *et al.* Bars indicate standard error of the mean.

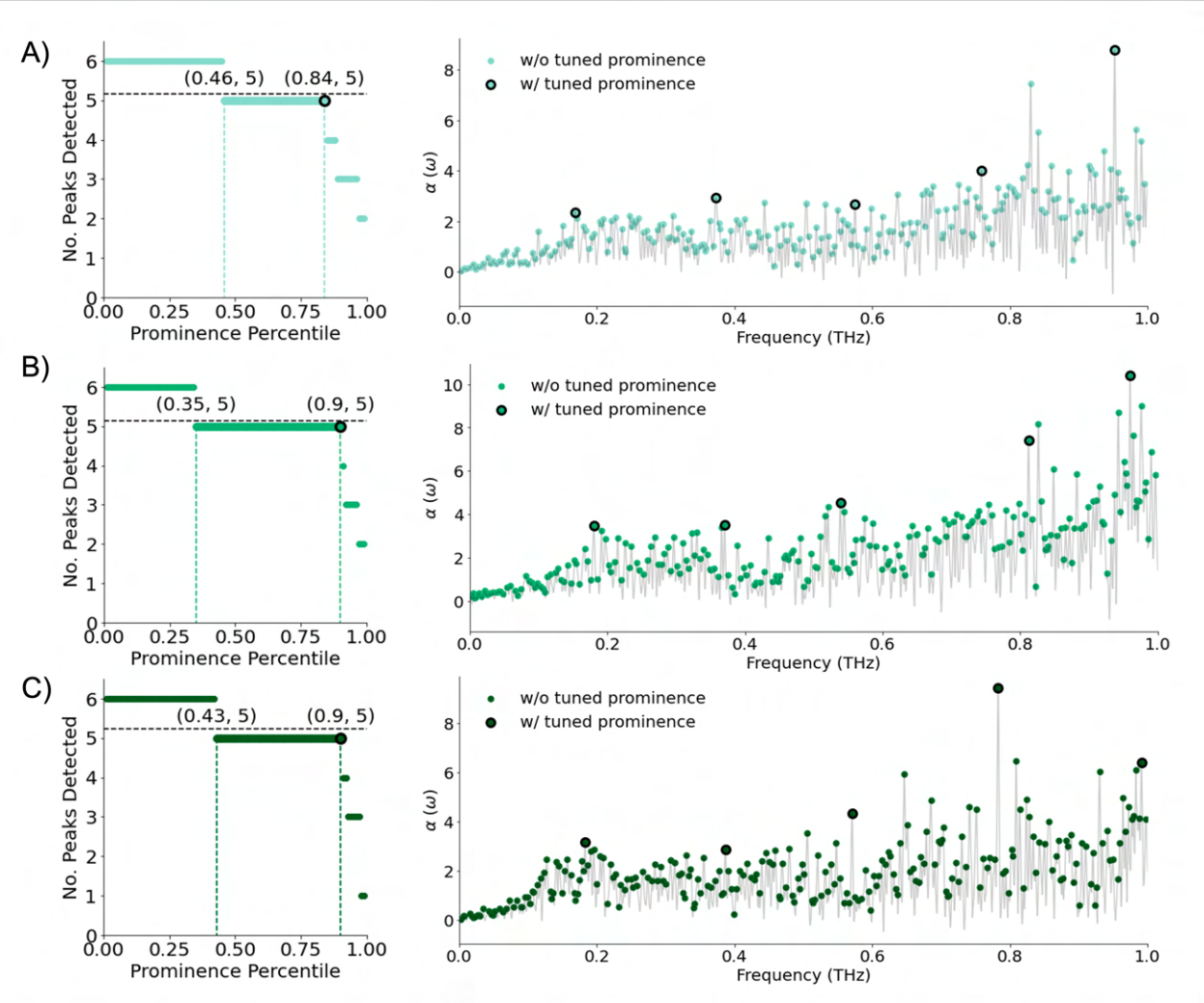

Figure B.3: **Prominence Filter Tuning.** Demonstration of prominence filter tuning in signal detection for 3 replicas of the $S476^{A}_{33}$ membrane. Each panel represents a different replica. Final peaks are determined by taking the average and standard error of the mean for each tuned peak across replicas. (left) Step function plots show the number of peaks as a function of the prominence threshold, with the dashed line indicating the average number of peaks; the black circle shows the final threshold value and number in parentheses demarcate the percentile interval of thresholds that detect a number of peaks close to the average.

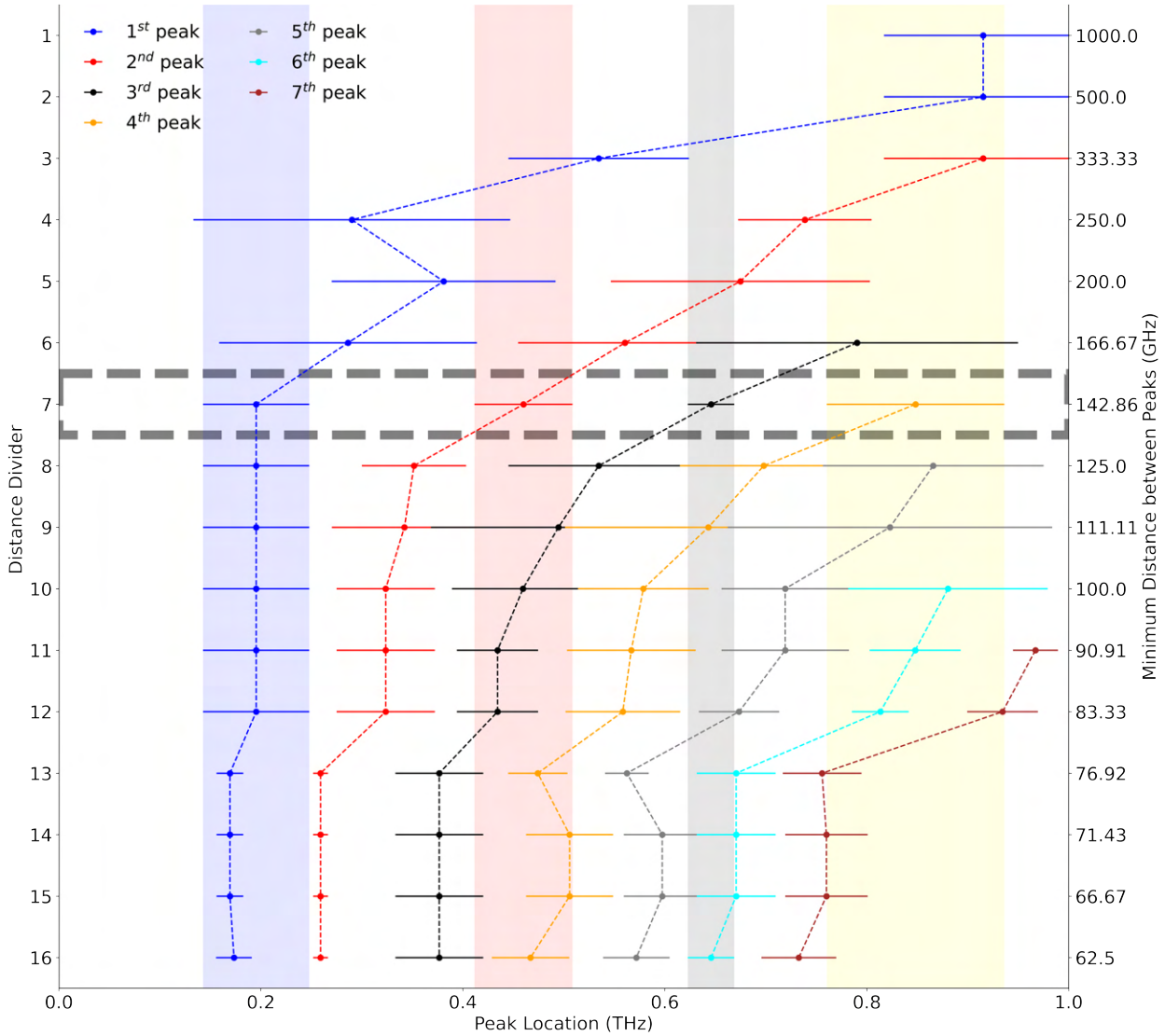

Figure B.4: **Distance Filter Selection for S476$^{A}_{51}$.** Horizontal, gray, dotted box highlights the distance filter chosen for S476$^{A}_{51}$ membranes. Shaded blue (first peak), red (second peak), gray (third peak), and yellow (fourth peak) demonstrate the region of convergence of spectra peaks.

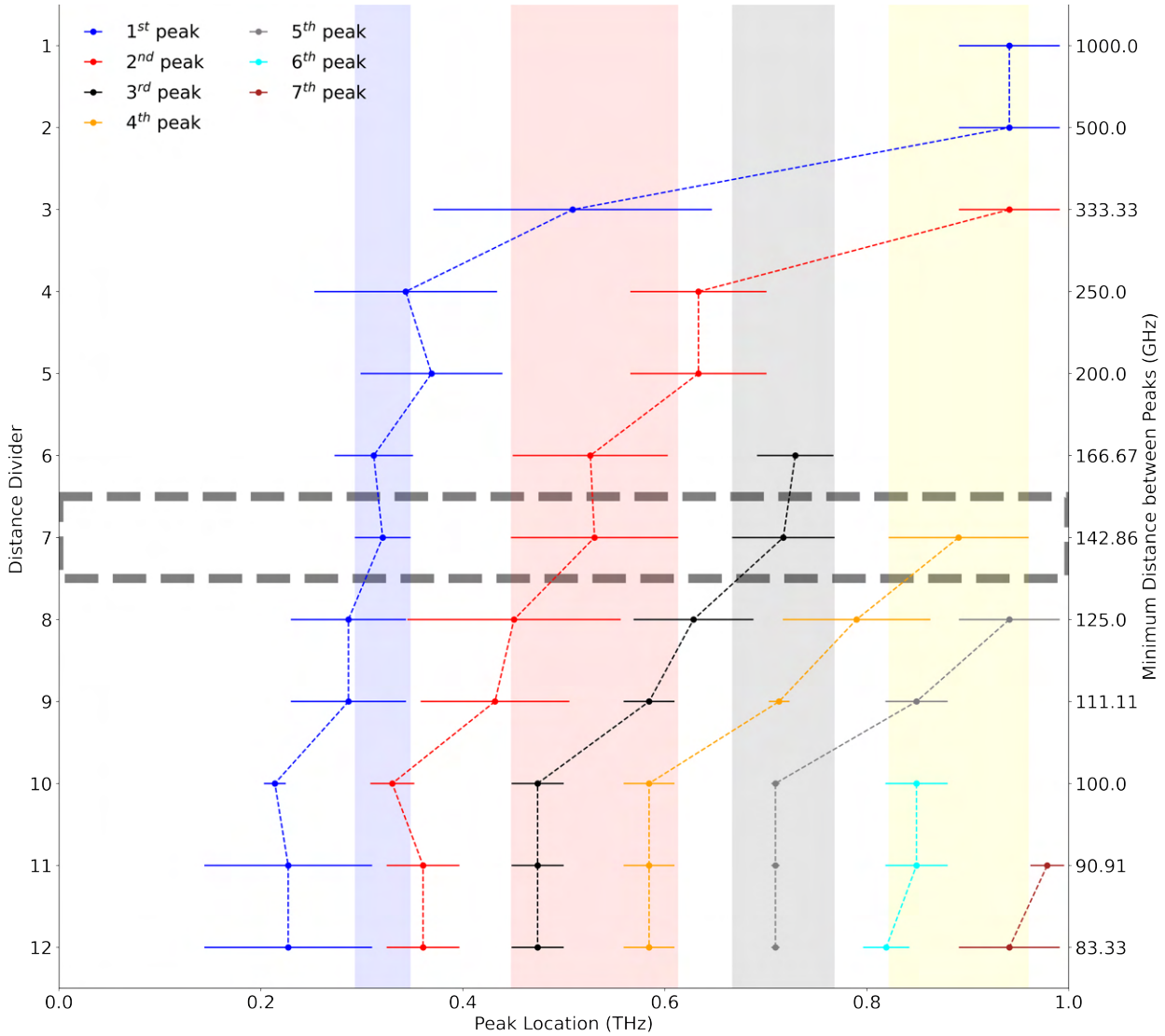

Figure B.5: **Distance Filter Selection for *B. Subtilis* Membrane.** Horizontal, gray, dotted box highlights the distance filter chosen for *B. Subtilis* membrane. Shaded blue (first peak), red (second peak), gray (third peak), and yellow (fourth peak) demonstrate the region of convergence of spectra peaks.

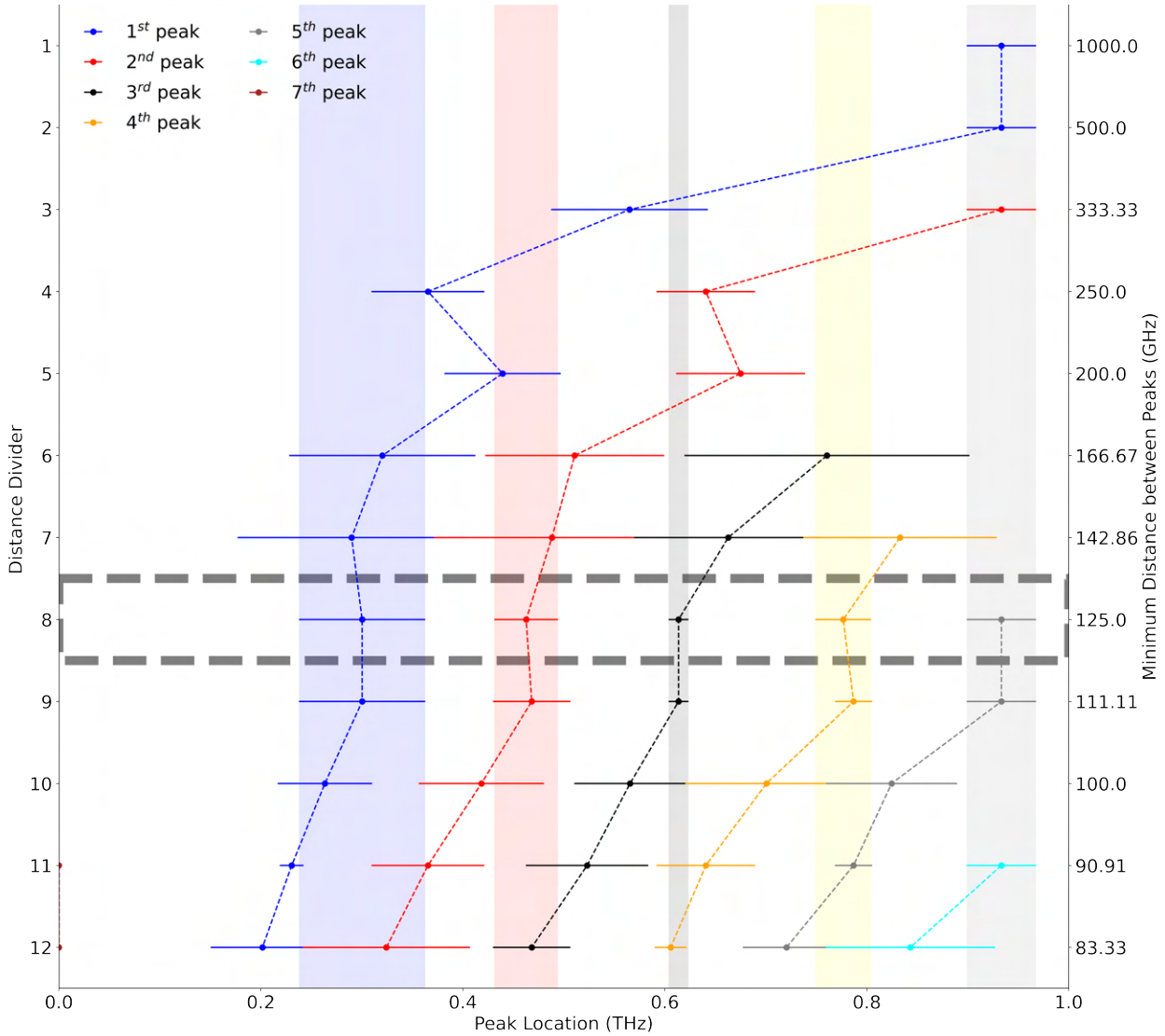

Figure B.6: **Distance Filter Selection for Rat Liver Plasma Membrane.** Horizontal, gray, dotted box highlights the distance filter chosen for rat liver plasma membrane. Shaded blue (first peak), red (second peak), gray (third peak), yellow (fourth peak), and light gray (fifth peak) demonstrate the region of convergence of spectra peaks.

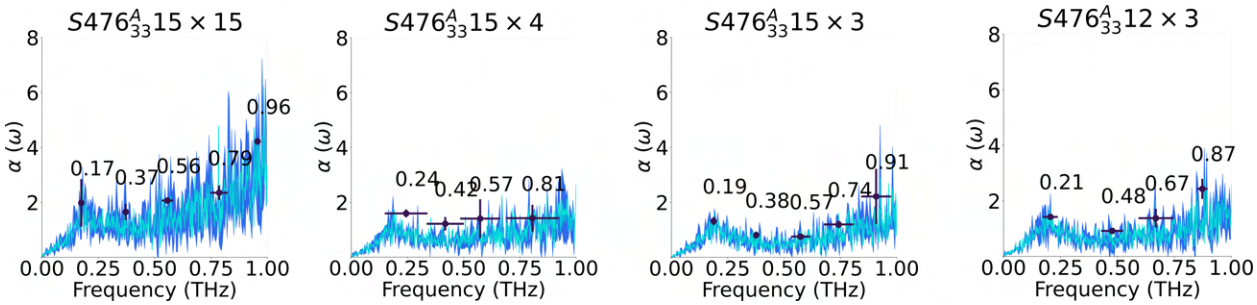

Figure B.7: **Effect of S476$^{A}_{33}$ Periodic Boundary Size on Spectra** after normalization. Normalization occurs after the filter is applied. Average spectra is in cyan, and standard deviation among replicas for spectra is in dark blue. Bars indicate standard deviation for peaks.

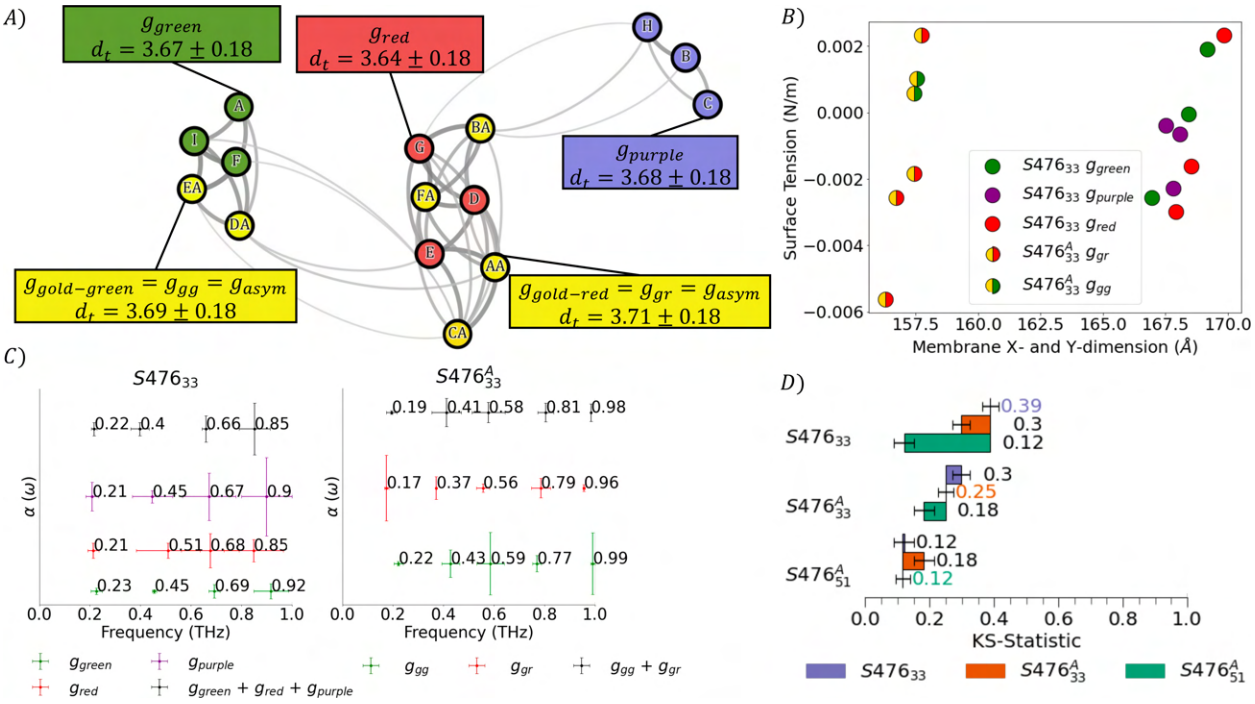

Figure B.8: **Clustering Analysis for KS Statistics of $S476_{33}$ and $S476^{A}_{33}$ Replicas.** (A) Fully connected weighted graph created using (1 - KS-statistics) as the weight for each edge. Nodes represent replicas of $S476^{A}_{33}$ and $S476_{33}$; only edges with weight higher than 0.75 are shown. Colors indicate modularity clustering; $S476_{33}$ spectra are grouped into 3 clusters (g_{green}, g_{red}, and g_{purple},) and the $S476^{A}_{33}$ spectra into 2 groups (g_{gg} and g_{gr}). Groups g_{red} and g_{gr} were chosen in the main text. Membrane thickness (d_t) with its standard deviation is reported for each group/membrane type. (B) Membrane dimension and surface tension of the system are also not determinants of grouping. Errors are not shown, as standard deviations are insignificant compared to marker size. (C) Both peak location and peak intensity among replicas in different groups; peak locations are staggered upward on the relative absorption scale for clarity. Error bars indicate standard deviation. (D) KS-statistics comparison among *S. aureus* membranes as a result of averaging groups (g_{green}, g_{red}, and g_{purple} to make $S476_{33}$, and groups g_{gg} and g_{gr} to make $S476^{A}_{33}$) shows that the spectra from symmetric and asymmetric membranes are still statistically indistinguishable. Error bars represent the standard error of the mean.

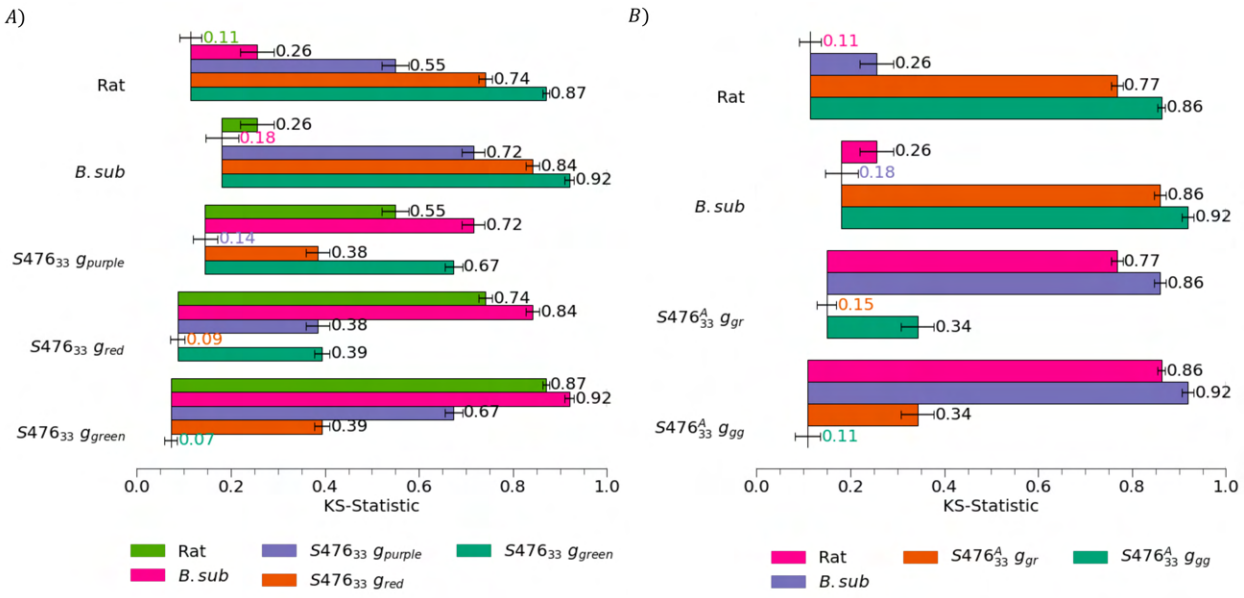

Figure B.9: **KS Statistics for S476$_{33}$ and S476$^{A}_{33}$ Clusters.** KS statistics for each S476$_{33}$ (A) and S476$^{A}_{33}$ (B) cluster (see Fig. B.8A for definition), shows that independently of the chosen group, the spectra of *S. aureus*, *B. Subtilis* and rat liver cell are distinguishable. Error bars represent the standard error of the mean.

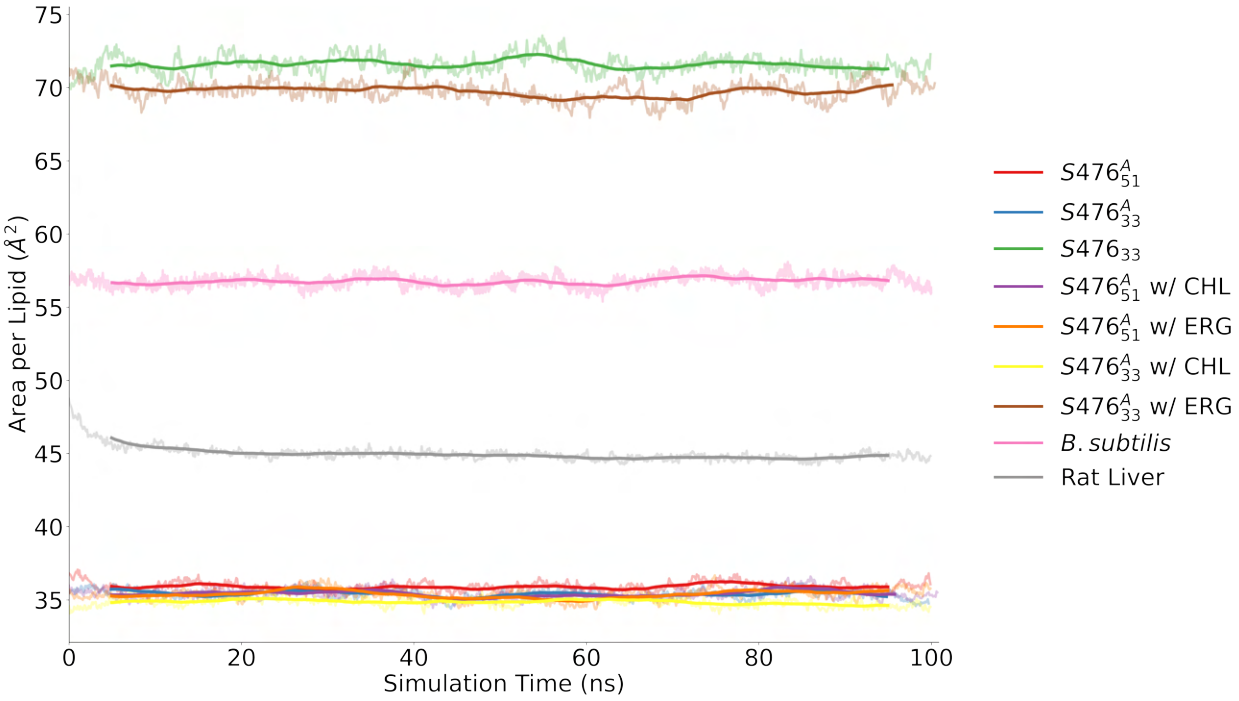

Figure B.10: **Area per Lipid Equilibration.** Area per Lipid over Time from NPsT Ensemble shows converged and stable membrane systems. Faint lines are raw area per lipids calculated over time, and solid lines are the moving averages of area per lipid for each membrane.

Table B.1: **Asymmetric *S. aureus* Membrane Compositions per Leaflet.** Asymmetric *S. aureus* Membrane Compositions for $S476^A_{51}$ and $S476^A_{33}$.The subscript represents the total concentration of LPG in the membrane, as determined by Rehal *et al.*

Leaflet	PG	LPG	CL
Upper	10%	95%	20%
Lower	90%	5%	80%

Table B.2: **Detailed Membrane Compositions** by lipid type as percentages. In the Leaflet column, U stands for "Upper", while L stands for "Lower". For *S. aureus* membranes, PG fatty acid tail is POPG, LPG fatty acid tail is PLPG, and CL is TMCL1. For rat liver plasma membranes, CL is PVCL2, PE is POPE, PC is POPC, PI is POPI, and PS is POPS.

Type	Leaflet	PG	LPG	CL	FA	DAG	PE	PC	PI	PS	PSM	CHL
$S476^{A}_{51}$	U	48.5	4.3	1.2	-	-	-	-	-	-	-	-
	L	2.5	38.7	4.8	-	-	-	-	-	-	-	-
$S476^{A}_{33}$	U	32.3	6.2	0.8	-	-	-	-	-	-	-	-
	L	1.7	55.8	3.2	-	-	-	-	-	-	-	-
$S476_{33}$	Both	62	34	4	-	-	-	-	-	-	-	-
B. subtilis	Both	9.5	-	2.9	1.9	30.2	55.5	-	-	-	-	-
Rat Liver	Both	-	-	1	-	-	15	25	5	6	11	37

Table B.3: **Complete KS Statistics.** KS Statistics, where KS statistic is reported to three significant figures. Errors are standard errors of the mean. ⊗ indicates that the membrane does not contain sterols, CHL indicates the membrane contains cholesterol, and ERG indicates the membrane contains ergosterol.

Type	KS Statistic
S476$^A_{51}$ (⊗) vs. S476$^A_{51}$ (⊗)	0.12 ± 0.02
S476$^A_{51}$ (⊗) vs. S476$^A_{33}$ (⊗)	0.12 ± 0.02
S476$^A_{51}$ (⊗) vs. S476$_{33}$ (⊗)	0.08 ± 0.01
S476$^A_{51}$ (⊗) vs. S476$^A_{51}$ (CHL)	0.21 ± 0.05
S476$^A_{51}$ (⊗) vs. S476$^A_{51}$ (ERG)	0.12 ± 0.02
S476$^A_{33}$ (⊗) vs. S476$^A_{33}$ (⊗)	0.15 ± 0.02
S476$^A_{33}$ (⊗) vs. S476$_{33}$ (⊗)	0.11 ± 0.01
S476$^A_{33}$ (⊗) vs. S476$^A_{33}$ (CHL)	0.33 ± 0.04
S476$^A_{33}$ (⊗) vs. S476$^A_{33}$ (ERG)	0.23 ± 0.03
S476$^A_{33}$ (⊗) vs. *B. Subtilis*	0.86 ± 0.01
S476$^A_{33}$ (⊗) vs. Rat Liver	0.77 ± 0.01
S476$_{33}$ (⊗) vs. S476$_{33}$ (⊗)	0.09 ± 0.02
S476$^A_{51}$ (CHL) vs. S476$^A_{51}$ (CHL)	0.22 ± 0.05
S476$^A_{51}$ (CHL) vs. S476$^A_{51}$ (ERG)	0.17 ± 0.04
S476$^A_{33}$ (CHL) vs. S476$^A_{33}$ (CHL)	0.19 ± 0.04
S476$^A_{33}$ (CHL) vs. S476$^A_{33}$ (ERG)	0.45 ± 0.05
S476$^A_{33}$ (ERG) vs. S476$^A_{33}$ (ERG)	0.15 ± 0.03
S476$^A_{33}$ (ERG) vs. S476$^A_{33}$ (ERG)	0.25 ± 0.06
B. Subtilis* vs. *B. Subtilis	0.18 ± 0.03
***B. Subtilis* vs. Rat Liver**	0.30 ± 0.04
Rat Liver vs. Rat Liver	0.11 ± 0.02

```
// Dipole Calculation TCL Script
// Step 1 in Figure 2
#!/usr/bin/tclsh

set name1 "psf_file"
set name2 "pdb_file"
set selection "segid MEMB"

set ipsf ${name1}.psf
set idcd ${name2}.dcd

mol load psf $ipsf dcd $idcd

set sel [atomselect top ${selection}]

set totq [vecsum [join [${sel} get charge] { }]]
vmdcon -info "Selection net charge: $totq"

set of [open ${name2}.dipole.txt w]
puts $of [format "# D_tot Dx  Dy    Dz"]
set numframes [molinfo top get numframes]

for {set i 0} { $i < ${numframes} } {incr i} {
  ${sel} frame $i
  set dipv [measure dipole $sel -masscenter]
  set Dx [lindex ${dipv} 0]
  set Dy [lindex ${dipv} 1]
  set Dz [lindex ${dipv} 2]
  set D [expr sqrt(${Dx}**2 + ${Dy}**2 + ${Dz}**2) ]
  puts ${of} [format "%6g %6g %6g %6g" $D ${Dx} ${Dy} ${Dz}]
  flush ${of}
}

close ${of}
exit
```

APPENDIX C

Nanoparticles

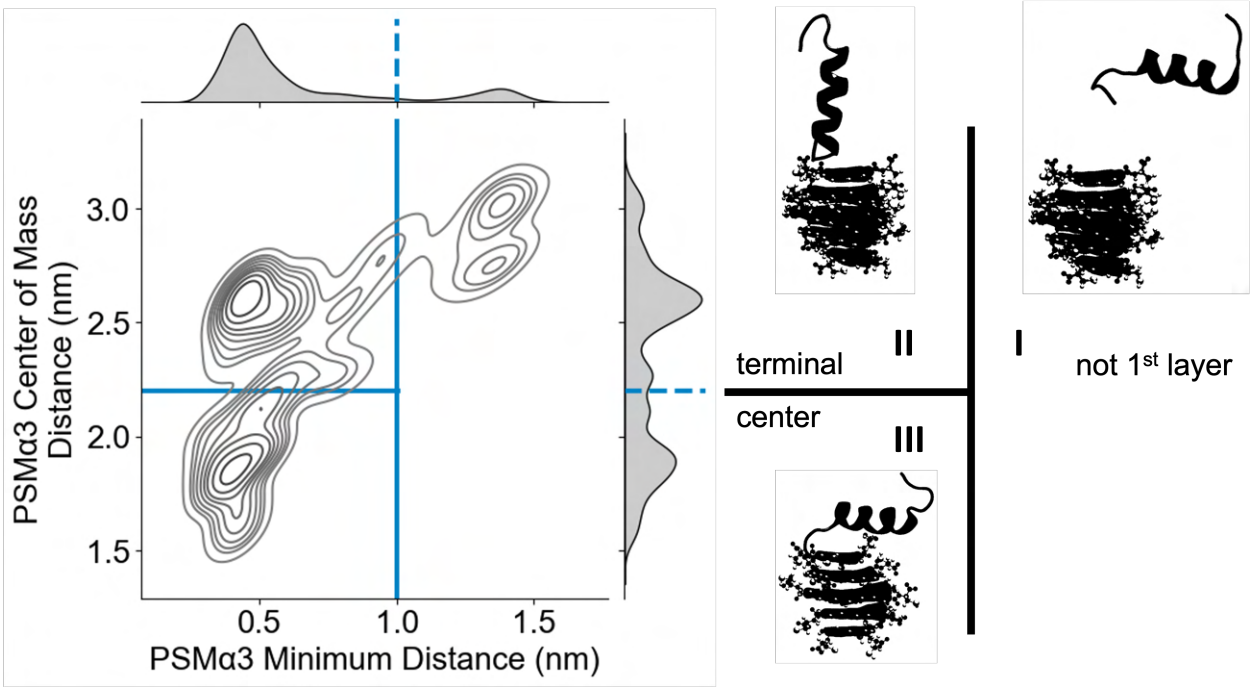

Figure C.1: **Example of conformations assumed by PSMα3 peptides interacting with *L*-CNP** (first layer). The left panel shows the distribution of configuration as a function of the minimum distance (between the CNP surface and all the PSMα3 atoms) and PSMα3 center of mass distance. Isolines of the smoothed data (using a Gaussian kernel function) are shown in gray. Projected distributions on single dimensions are shown on the right and top. Blue lines indicate the approximate grouping of confirmation, as explained in the right panel.

BIBLIOGRAPHY

BIBLIOGRAPHY

[1] Alissa Bleem, Robyn Francisco, James D Bryers, and Valerie Daggett. Designed α-sheet peptides suppress amyloid formation in staphylococcus aureus biofilms. *NPJ Biofilms and Microbiomes*, 3(1):1–10, 2017.

[2] David M Bamberger and Sarah E Boyd. Management of staphylococcus aureus infections. *American family physician*, 72(12):2474–2481, 2005.

[3] C Lee Ventola. The antibiotic resistance crisis: part 1: causes and threats. *Pharmacy and therapeutics*, 40(4):277, 2015.

[4] Kelly Schwartz, Mahesh Ganesan, David E Payne, Michael J Solomon, and Blaise R Boles. Extracellular dna facilitates the formation of functional amyloids in staphylococcus aureus biofilms. *Molecular microbiology*, 99(1):123–134, 2016.

[5] Virginio Cepas, Yuly López, Estela Munoz, Dora Rolo, Carmen Ardanuy, Sara Martí, Mariona Xercavins, Juan Pablo Horcajada, Jordi Bosch, and Sara M Soto. Relationship between biofilm formation and antimicrobial resistance in gram-negative bacteria. *Microbial Drug Resistance*, 25(1):72–79, 2019.

[6] Ping Zeng, Chen Xu, Qipeng Cheng, Jun Liu, Wei Gao, Xuemei Yang, Kwok-Yin Wong, Sheng Chen, and Kin-Fai Chan. Phenol-soluble-modulin-inspired amphipathic peptides have bactericidal activity against multidrug-resistant bacteria. *ChemMedChem*, 14(16):1547–1559, 2019.

[7] Cecily Wing Hei Cheng, Matthew Wai Heng Chung, and Joseph Chi Fung Ng. Structural dynamics of amyloid-β aggregation in alzheimer's disease: computational and experimental approaches. *Journal of Young Investigators*, 31(6):44–50, 2016.

[8] TO Kryuchko, O Ya Tkachenko, NV Kuzmenko, IN Nesina, SM Tanianska, IA Kolenko, and MO Melnyk. Modern approaches to antivirulent therapy of diseases associated with staphylococcus aureus. *The Medical and Ecological Problems*, 23(3-4):26–31, 2019.

[9] Matthew P Jackson and Eric W Hewitt. Why are functional amyloids non-toxic in humans? *Biomolecules*, 7(4):71, 2017.

[10] M Fändrich. On the structural definition of amyloid fibrils and other polypeptide aggregates. *Cellular and Molecular Life Sciences*, 64(16):2066–2078, 2007.

[11] Kelly Schwartz, Adnan K Syed, Rachel E Stephenson, Alexander H Rickard, and Blaise R Boles. Functional amyloids composed of phenol soluble modulins stabilize staphylococcus aureus biofilms. *PLoS pathogens*, 8(6):1–11, 2012.

[12] Katherine Y Le, Amer E Villaruz, Yue Zheng, Lei He, Emilie L Fisher, Thuan H Nguyen, Trung V Ho, Anthony J Yeh, Hwang-Soo Joo, Gordon YC Cheung, et al. Role of phenol-soluble modulins in staphylococcus epidermidis biofilm formation and infection of indwelling medical devices. *Journal of molecular biology*, 431(16):3015–3027, 2019.

[13] Agustina Taglialegna, Iñigo Lasa, and Jaione Valle. Amyloid structures as biofilm matrix scaffolds. *Journal of bacteriology*, 198(19):2579–2588, 2016.

[14] Theodoros K Karamanos, Matthew P Jackson, Antonio N Calabrese, Sophia C Goodchild, Emma E Cawood, Gary S Thompson, Arnout P Kalverda, Eric W Hewitt, and Sheena E Radford. Structural mapping of oligomeric intermediates in an amyloid assembly pathway. *Elife*, 8, 2019.

[15] Hajime Ikigai and Taiji Nakae. Assembly of the alpha-toxin-hexamer of staphylococcus aureus in the liposome membrane. *Journal of Biological Chemistry*, 262(5):2156–2160, 1987.

[16] JE Gillam and CE MacPhee. Modelling amyloid fibril formation kinetics: mechanisms of nucleation and growth. *Journal of Physics: Condensed Matter*, 25(37):373101, 2013.

[17] Gordon YC Cheung, Hwang-Soo Joo, Som S Chatterjee, and Michael Otto. Phenol-soluble modulins–critical determinants of staphylococcal virulence. *FEMS microbiology reviews*, 38(4):698–719, 2014.

[18] Nir Salinas, Jacques-Philippe Colletier, Asher Moshe, and Meytal Landau. Extreme amyloid polymorphism in staphylococcus aureus virulent psmα peptides. *Nature communications*, 9(1):1–9, 2018.

[19] Patrizia Marinelli, Irantzu Pallares, Susanna Navarro, and Salvador Ventura. Dissecting the contribution of staphylococcus aureus α-phenol-soluble modulins to biofilm amyloid structure. *Scientific reports*, 6(1):1–13, 2016.

[20] Einav Tayeb-Fligelman, Orly Tabachnikov, Asher Moshe, Orit Goldshmidt-Tran, Michael R Sawaya, Nicolas Coquelle, Jacques-Philippe Colletier, and Meytal Landau. The cytotoxic staphylococcus aureus psmα3 reveals a cross-α amyloid-like fibril. *Science*, 355(6327):831–833, 2017.

[21] Sarah L Shammas, Tuomas PJ Knowles, Andrew J Baldwin, Cait E MacPhee, Mark E Welland, Christopher M Dobson, and Glyn L Devlin. Perturbation of the stability of amyloid fibrils through alteration of electrostatic interactions. *Biophysical journal*, 100(11):2783–2791, 2011.

[22] Anthony WP Fitzpatrick, Galia T Debelouchina, Marvin J Bayro, Daniel K Clare, Marc A Caporini, Vikram S Bajaj, Christopher P Jaroniec, Luchun Wang, Vladimir Ladizhansky, Shirley A Müller, Cait E MacPhee, Christopher A Waudby, Helen R Mott, Alfonso De Simone, Tuomas P J Knowles, Helen R Saibil, Michele Vendruscolo, Elena V Orlova, Robert G Griffin, and Christopher M Dobson. Atomic structure and hierarchical assembly of a cross-β amyloid fibril. *Proceedings of the National Academy of Sciences*, 110(14):5468–5473, 2013.

[23] Jason Greenwald and Roland Riek. Biology of amyloid: structure, function, and regulation. *Structure*, 18(10):1244–1260, 2010.

[24] Katja Schlatterer, Christian Beck, Dennis Hanzelmann, Marco Lebtig, Birgit Fehrenbacher, Martin Schaller, Patrick Ebner, Mulugeta Nega, Michael Otto, Dorothee Kretschmer, et al. The mechanism behind bacterial lipoprotein release: Phenol-soluble modulins mediate toll-like receptor 2 activation via extracellular vesicle release from staphylococcus aureus. *MBio*, 9(6):e01851–18, 2018.

[25] Jens Schreiner, Dorothee Kretschmer, Juliane Klenk, Michael Otto, Hans-Jörg Bühring, Stefan Stevanovic, Ji Ming Wang, Sandra Beer-Hammer, Andreas Peschel, and Stella E Autenrieth. Staphylococcus aureus phenol-soluble modulin peptides modulate dendritic cell functions and increase in vitro priming of regulatory t cells. *The Journal of Immunology*, 190(7):3417–3426, 2013.

[26] Andreas Peschel and Michael Otto. Phenol-soluble modulins and staphylococcal infection. *Nature Reviews Microbiology*, 11(10):667–673, 2013.

[27] Sana S Dastgheyb, Amer E Villaruz, Katherine Y Le, Vee Y Tan, Anthony C Duong, Som S Chatterjee, Gordon YC Cheung, Hwang-Soo Joo, Noreen J Hickok, and Michael Otto. Role of phenol-soluble modulins in formation of staphylococcus aureus biofilms in synovial fluid. *Infection and immunity*, 83(7):2966–2975, 2015.

[28] Paolo Elvati, Chloe Luyet, Yichun Wang, Changjiang Liu, J Scott VanEpps, Nicholas A Kotov, and Angela Violi. Molecular architecture and helicity of bacterial amyloid nanofibers: Implications for the design of nanoscale antibiotics. *ACS Applied Nano Materials*, 6:6594–6604, 2023.

[29] Mitradip Das, Sandeep Dash, and BL Bhargava. Computational studies of fibrillation induced selective cytotoxicity of cross-α amyloid–phenol soluble modulin α3. *Chemical Physics*, page 110777, 2020.

[30] Raffaella Paparcone and Markus J Buehler. Microscale structural model of alzheimer a β (1–40) amyloid fibril. *Applied Physics Letters*, 94(24):243904, 2009.

[31] Changjiang Liu, Paolo Elvati, Sagardip Majumder, Yichun Wang, Allen P. Liu, and Angela Violi. Predicting the Time of Entry of Nanoparticles in Lipid Membranes. *ACS Nano*, 13(9):10221–10232, 2019.

[32] Stefan Paula, AG Volkov, AN Van Hoek, TH Haines, and David W Deamer. Permeation of protons, potassium ions, and small polar molecules through phospholipid bilayers as a function of membrane thickness. *Biophysical journal*, 70(1):339–348, 1996.

[33] Mikhail Zhernenkov, Dima Bolmatov, Dmitry Soloviov, Kirill Zhernenkov, Boris P Toperverg, Alessandro Cunsolo, Alexey Bosak, and Yong Q Cai. Revealing the mechanism of passive transport in lipid bilayers via phonon-mediated nanometre-scale density fluctuations. *Nature communications*, 7(1):1–10, 2016.

[34] SH Chen, CY Liao, HW Huang, TM Weiss, MC Bellisent-Funel, and F Sette. Collective dynamics in fully hydrated phospholipid bilayers studied by inelastic x-ray scattering. *Physical Review Letters*, 86(4):740, 2001.

[35] Dmitry V Leonov, Sergei A Dzuba, and Nikolay V Surovtsev. Normal vibrations of ternary dopc/dppc/cholesterol lipid bilayers by low-frequency raman spectroscopy. *RSC advances*, 9(59):34451–34456, 2019.

[36] William Weber Coblentz. *Radiometric investigation of water of crystallization, light filters, and standard absorption bands*, volume 7. US Government Printing Office, 1911.

[37] Luc Montagnier, Jamal Aissa, Stéphane Ferris, Jean-Luc Montagnier, and Claude Lavalléee. Electromagnetic signals are produced by aqueous nanostructures derived from bacterial dna sequences. *Interdisciplinary Sciences: Computational Life Sciences*, 1(2):81–90, 2009.

[38] Chloe Luyet, Paolo Elvati, Jordan Vinh, and Angela Violi. Low-thz vibrations of biological membranes. *Membranes*, 13(2):139, 2023.

[39] Yichun Wang, Usha Kadiyala, Zhibei Qu, Paolo Elvati, Christopher Altheim, Nicholas A Kotov, Angela Violi, and J Scott VanEpps. Anti-biofilm activity of graphene quantum dots via self-assembly with bacterial amyloid proteins. *ACS nano*, 13(4):4278–4289, 2019.

[40] Huajuan Wang, Zhiyong Song, Jiangjiang Gu, Shuojun Li, Yang Wu, and Heyou Han. Nitrogen-doped carbon quantum dots for preventing biofilm formation and eradicating drug-resistant bacteria infection. *ACS Biomaterials Science & Engineering*, 5(9):4739–4749, 2019.

[41] Yibiao Liu, Li-Ping Xu, Wenhao Dai, Haifeng Dong, Yongqiang Wen, and Xueji Zhang. Graphene quantum dots for the inhibition of β amyloid aggregation. *Nanoscale*, 7(45):19060–19065, 2015.

[42] Zhiping Zeng, Dingshan Yu, Ziming He, Jing Liu, Fang-Xing Xiao, Yan Zhang, Rong Wang, Dibakar Bhattacharyya, and Timothy Thatt Yang Tan. Graphene oxide quantum dots covalently functionalized pvdf membrane with significantly-enhanced bactericidal and antibiofouling performances. *Scientific reports*, 6:20142, 2016.

[43] Mei-Ling Chen, Ye-Ju He, Xu-Wei Chen, and Jian-Hua Wang. Quantum-dot-conjugated graphene as a probe for simultaneous cancer-targeted fluorescent imaging, tracking, and monitoring drug delivery. *Bioconjugate chemistry*, 24(3):387–397, 2013.

[44] Zhengfang Tian, Xianxian Yao, Kexin Ma, Xingxing Niu, Julia Grothe, Qingni Xu, Liansheng Liu, Stefan Kaskel, and Yufang Zhu. Metal–organic framework/graphene quantum dot nanoparticles used for synergistic chemo-and photothermal therapy. *ACS omega*, 2(3):1249–1258, 2017.

[45] Zhuang Liu, Joshua T Robinson, Xiaoming Sun, and Hongjie Dai. Pegylated nanographene oxide for delivery of water-insoluble cancer drugs. *Journal of the American Chemical Society*, 130(33):10876–10877, 2008.

[46] Nozomu Suzuki, Yichun Wang, Paolo Elvati, Zhi-Bei Qu, Kyoungwon Kim, Shuang Jiang, Elizabeth Baumeister, Jaewook Lee, Bongjun Yeom, Joong Hwan Bahng, Jaebeom Lee, Angela Violi, and Nicholas A. Kotov. Chiral Graphene Quantum Dots. *ACS Nano*, 10(2):1744–1755, 2016.

[47] Yu Chong, Yufei Ma, He Shen, Xiaolong Tu, Xuan Zhou, Jiaying Xu, Jianwu Dai, Saijun Fan, and Zhijun Zhang. The in vitro and in vivo toxicity of graphene quantum dots. *Biomaterials*, 35(19):5041–5048, 2014.

[48] Max Levy, Partha P Chowdhury, and Prashant Nagpal. Quantum dot therapeutics: a new class of radical therapies. *Journal of biological engineering*, 13(1):48, 2019.

[49] Daniela Iannazzo, Alessandro Pistone, Marina Salamò, Signorino Galvagno, Roberto Romeo, Salvatore V Giofré, Caterina Branca, Giuseppa Visalli, and Angela Di Pietro. Graphene quantum dots for cancer targeted drug delivery. *International journal of pharmaceutics*, 518(1-2):185–192, 2017.

[50] Feng Li, Yiye Li, Xiao Yang, Xuexiang Han, Yang Jiao, Taotao Wei, Dayong Yang, Huaping Xu, and Guangjun Nie. Highly fluorescent chiral n-s-doped carbon dots from cysteine: affecting cellular energy metabolism. *Angewandte Chemie*, 130(9):2401–2406, 2018.

[51] Vsevolod A Tverdislov. Chirality as an instrument of stratification of hierarchical systems in animate and inanimate nature. *arXiv preprint arXiv:1212.1677*, 2012.

[52] Dan Zhao, Mengyu Xu, Kang Dai, Huan Liu, Yan Jiao, and Xincai Xiao. The preparation of chiral carbon dots and the study on their antibacterial abilities. *Materials Chemistry and Physics*, 295:127144, 2023.

[53] Florence Victoria, John Manioudakis, Liana Zaroubi, Brandon Findlay, and Rafik Naccache. Tuning residual chirality in carbon dots with anti-microbial properties. *RSC advances*, 10(53):32202–32210, 2020.

[54] Ravit Malishev, Elad Arad, Susanta Kumar Bhunia, Shira Shaham-Niv, Sofiya Kolusheva, Ehud Gazit, and Raz Jelinek. Chiral modulation of amyloid beta fibrillation and

cytotoxicity by enantiomeric carbon dots. *Chemical Communications*, 54(56):7762–7765, 2018.

[55] Misché A Hubbard, Chloe Luyet, Prashant Kumar, Paolo Elvati, J Scott VanEpps, Angela Violi, and Nicholas A Kotov. Chiral chromatography and surface chirality of carbon nanoparticles. *Chirality*, 34(12):1494–1502, 2022.

[56] James C Phillips, Rosemary Braun, Wei Wang, James Gumbart, Emad Tajkhorshid, Elizabeth Villa, Christophe Chipot, Robert D Skeel, Laxmikant Kale, and Klaus Schulten. Scalable molecular dynamics with namd. *Journal of computational chemistry*, 26(16):1781–1802, 2005.

[57] James C. Phillips, David J. Hardy, Julio D.C. Maia, John E. Stone, João V. Ribeiro, Rafael C. Bernardi, Ronak Buch, Giacomo Fiorin, Jérôme Hénin, Wei Jiang, Ryan McGreevy, Marcelo C.R. Melo, Brian K. Radak, Robert D. Skeel, Abhishek Singharoy, Yi Wang, Benoît Roux, Aleksei Aksimentiev, Zaida Luthey-Schulten, Laxmikant V. Kalé, Klaus Schulten, Christophe Chipot, and Emad Tajkhorshid. Scalable molecular dynamics on CPU and GPU architectures with NAMD. *Journal of Chemical Physics*, 153(4):44130, jul 2020.

[58] Gareth A Tribello, Massimiliano Bonomi, Davide Branduardi, Carlo Camilloni, and Giovanni Bussi. Plumed 2: New feathers for an old bird. *Computer physics communications*, 185(2):604–613, 2014.

[59] Massimiliano Bonomi, Davide Branduardi, Giovanni Bussi, Carlo Camilloni, Davide Provasi, Paolo Raiteri, Davide Donadio, Fabrizio Marinelli, Fabio Pietrucci, Ricardo A Broglia, et al. Plumed: A portable plugin for free-energy calculations with molecular dynamics. *Computer Physics Communications*, 180(10):1961–1972, 2009.

[60] William L Jorgensen, Jayaraman Chandrasekhar, Jeffry D Madura, Roger W Impey, and Michael L Klein. Comparison of simple potential functions for simulating liquid water. *The Journal of chemical physics*, 79(2):926–935, 1983.

[61] Jing Huang and Alexander D MacKerell Jr. Charmm36 all-atom additive protein force field: Validation based on comparison to nmr data. *Journal of computational chemistry*, 34(25):2135–2145, 2013.

[62] Michael R Sawaya, Shilpa Sambashivan, Rebecca Nelson, Magdalena I Ivanova, Stuart A Sievers, Marcin I Apostol, Michael J Thompson, Melinda Balbirnie, Jed JW Wiltzius, Heather T McFarlane, Anders Ø Madsen, Christian Riekel, and David Eisenberg. Atomic structures of amyloid cross-β spines reveal varied steric zippers. *Nature*, 447(7143):453–457, 2007.

[63] William Humphrey, Andrew Dalke, and Klaus Schulten. Vmd: visual molecular dynamics. *Journal of molecular graphics*, 14(1):33–38, 1996.

[64] Richard J Gowers, Max Linke, Jonathan Barnoud, Tyler JE Reddy, Manuel N Melo, Sean L Seyler, Jan Domanski, David L Dotson, Sébastien Buchoux, Ian M Kenney,

et al. Mdanalysis: a python package for the rapid analysis of molecular dynamics simulations. In *Proceedings of the 15th python in science conference*, volume 98, page 105. SciPy Austin, TX, 2016.

[65] Sunhwan Jo, Taehoon Kim, Vidyashankara G Iyer, and Wonpil Im. Charmm-gui: a web-based graphical user interface for charmm. *Journal of computational chemistry*, 29(11):1859–1865, 2008.

[66] Pauli Virtanen, Ralf Gommers, Travis E Oliphant, Matt Haberland, Tyler Reddy, David Cournapeau, Evgeni Burovski, Pearu Peterson, Warren Weckesser, Jonathan Bright, et al. Scipy 1.0: fundamental algorithms for scientific computing in python. *Nature methods*, 17(3):261–272, 2020.

[67] Naveen Michaud-Agrawal, Elizabeth J Denning, Thomas B Woolf, and Oliver Beckstein. Mdanalysis: a toolkit for the analysis of molecular dynamics simulations. *Journal of computational chemistry*, 32(10):2319–2327, 2011.

[68] Alessandro Barducci, Giovanni Bussi, and Michele Parrinello. Well-tempered metadynamics: a smoothly converging and tunable free-energy method. *Physical review letters*, 100(2):020603, 2008.

[69] Alessandro Barducci, Massimiliano Bonomi, and Michele Parrinello. Metadynamics. *Wiley Interdisciplinary Reviews: Computational Molecular Science*, 1(5):826–843, 2011.

[70] John D Hunter. Matplotlib: A 2d graphics environment. *Computing in science & engineering*, 9(03):90–95, 2007.

[71] Scott E Feller, Yuhong Zhang, Richard W Pastor, and Bernard R Brooks. Constant pressure molecular dynamics simulation: The langevin piston method. *The Journal of chemical physics*, 103(11):4613–4621, 1995.

[72] Glenn J Martyna, Douglas J Tobias, and Michael L Klein. Constant pressure molecular dynamics algorithms. *The Journal of Chemical Physics*, 101(5):4177–4189, 1994.

[73] Richard J Loncharich, Bernard R Brooks, and Richard W Pastor. Langevin dynamics of peptides: The frictional dependence of isomerization rates of n-acetylalanyl-n"-methylamide. *Biopolymers: Original Research on Biomolecules*, 32(5):523–535, 1992.

[74] Jean-Paul Ryckaert, Giovanni Ciccotti, and Herman JC Berendsen. Numerical integration of the cartesian equations of motion of a system with constraints: molecular dynamics of n-alkanes. *Journal of computational physics*, 23(3):327–341, 1977.

[75] Axel T Brünger. *X-PLOR: version 3.1: a system for x-ray crystallography and NMR*. Yale University Press, 1992.

[76] Darrin M York, Tom A Darden, and Lee G Pedersen. The effect of long-range electrostatic interactions in simulations of macromolecular crystals: A comparison of the ewald and truncated list methods. *The Journal of Chemical Physics*, 99(10):8345–8348, 1993.

[77] Rafael Ramírez, Telesforo López-Ciudad, Padma Kumar P, and Dominik Marx. Quantum corrections to classical time-correlation functions: Hydrogen bonding and anharmonic floppy modes. *The Journal of chemical physics*, 121(9):3973–3983, 2004.

[78] Gerald J Wilmink, Bennett L Ibey, Benjamin D Rivest, Jessica E Grundt, William P Roach, Thomas D Tongue, Brian J Schulkin, Norman Laman, Xomalin G Peralta, Caleb C Roth, et al. Development of a compact terahertz time-domain spectrometer for the measurement of the optical properties of biological tissues. *Journal of biomedical optics*, 16(4):047006, 2011.

[79] John L Hodges. The significance probability of the smirnov two-sample test. *Arkiv för Matematik*, 3(5):469–486, 1958.

[80] Hans-Curt Flemming, Jost Wingender, Ulrich Szewzyk, Peter Steinberg, Scott A Rice, and Staffan Kjelleberg. Biofilms: an emergent form of bacterial life. *Nature Reviews Microbiology*, 14(9):563–575, 2016.

[81] Steven S Branda, Åshild Vik, Lisa Friedman, and Roberto Kolter. Biofilms: the matrix revisited. *Trends in microbiology*, 13(1):20–26, 2005.

[82] Wei Li, Jing Jing Wang, Hui Qian, Ling Tan, Zhaohuan Zhang, Haiquan Liu, Yingjie Pan, and Yong Zhao. Insights into the role of extracellular dna and extracellular proteins in biofilm formation of vibrio parahaemolyticus. *Frontiers in Microbiology*, 11:813, 2020.

[83] Anna Dragoš and Ákos T Kovács. The peculiar functions of the bacterial extracellular matrix. *Trends in microbiology*, 25(4):257–266, 2017.

[84] H-C Flemming and Jost Wingender. Relevance of microbial extracellular polymeric substances (epss)-part i: Structural and ecological aspects. *Water science and technology*, 43(6):1–8, 2001.

[85] Shayon Bhattacharya, Liang Xu, and Damien Thompson. Characterization of amyloidogenic peptide aggregability in helical subspace. In *Computer Simulations of Aggregation of Proteins and Peptides*, pages 401–448. Springer, 2022.

[86] Matthew R Chapman, Lloyd S Robinson, Jerome S Pinkner, Robyn Roth, John Heuser, Mårten Hammar, Staffan Normark, and Scott J Hultgren. Role of escherichia coli curli operons in directing amyloid fiber formation. *Science*, 295(5556):851–855, 2002.

[87] Diego Romero, Claudio Aguilar, Richard Losick, and Roberto Kolter. Amyloid fibers provide structural integrity to bacillus subtilis biofilms. *Proceedings of the National Academy of Sciences*, 107(5):2230–2234, 2010.

[88] Lauren Nicastro and Çagla Tükel. Bacterial amyloids: the link between bacterial infections and autoimmunity. *Trends in microbiology*, 27(11):954–963, 2019.

[89] David A Hufnagel, Çagla Tükel, and Matthew R Chapman. Disease to dirt: the biology of microbial amyloids. *PLoS pathogens*, 9(11):e1003740, 2013.

[90] Morten S Dueholm, Steen V Petersen, Mads Sønderkær, Poul Larsen, Gunna Christiansen, Kim L Hein, Jan J Enghild, Jeppe L Nielsen, Kåre L Nielsen, Per H Nielsen, and Daniel E Otzen. Functional amyloid in pseudomonas. *Molecular microbiology*, 77(4):1009–1020, 2010.

[91] Mnar Ghrayeb, Shahar Hayet, Neta Lester-Zer, Yael Levi-Kalisman, and Liraz Chai. Fibrilar polymorphism of the bacterial extracellular matrix protein tasa. *Microorganisms*, 9(3):529, 2021.

[92] Nitai Steinberg and Ilana Kolodkin-Gal. The matrix reloaded: how sensing the extracellular matrix synchronizes bacterial communities. *Journal of bacteriology*, 197(13):2092–2103, 2015.

[93] Sebastian J Van Hal, Slade O Jensen, Vikram L Vaska, Björn A Espedido, David L Paterson, and Iain B Gosbell. Predictors of mortality in staphylococcus aureus bacteremia. *Clinical microbiology reviews*, 25(2):362–386, 2012.

[94] AP Kourtis, K Hatfield, J Baggs, Y Mu, I See, E Epson, J Nadle, MA Kainer, G Dumyati, S Petit, et al. Emerging infections program mrsa author group: Vital signs: Epidemiology and recent trends in methicillin-resistant and in methicillin-susceptible staphylococcus aureus bloodstream infections-united states. *MMWR Morb Mortal Wkly Rep*, 68:214–219, 2019.

[95] Jaclyn A Cusumano, Amy C Dupper, Yesha Malik, Elizabeth M Gavioli, Jaspreet Banga, Ana Berbel Caban, Devika Nadkarni, Ajay Obla, Chirag V Vasa, Dana Mazo, and Deena R Altman. Staphylococcus aureus bacteremia in patients infected with covid-19: a case series. In *Open forum infectious diseases*, volume 7, page ofaa518. Oxford University Press US, 2020.

[96] Andreas Peschel and Michael Otto. Phenol-soluble modulins and staphylococcal infection. *Nature Reviews Microbiology*, 11(10):667–673, 2013.

[97] Saravanan Periasamy, Hwang-Soo Joo, Anthony C Duong, Thanh-Huy L Bach, Vee Y Tan, Som S Chatterjee, Gordon YC Cheung, and Michael Otto. How staphylococcus aureus biofilms develop their characteristic structure. *Proceedings of the National Academy of Sciences*, 109(4):1281–1286, 2012.

[98] Mark AB Kreutzberger, Shengyuan Wang, Leticia C Beltran, Abraham Tuachi, Xiaobing Zuo, Edward H Egelman, and Vincent P Conticello. Phenol-soluble modulins psmα3 and psmβ2 form nanotubes that are cross-α amyloids. *Proceedings of the National Academy of Sciences*, 119(20):e2121586119, 2022.

[99] Einav Tayeb-Fligelman, Nir Salinas, Orly Tabachnikov, and Meytal Landau. Staphylococcus aureus psmα3 cross-α fibril polymorphism and determinants of cytotoxicity. *Structure*, 28(3):301–313, 2020.

[100] Olivia M Cracchiolo, Dean N Edun, Vincent M Betti, Jacob M Goldberg, and Arnaldo L Serrano. Cross-α/β polymorphism of psmα3 fibrils. *Proceedings of the National Academy of Sciences*, 119(5):e2114923119, 2022.

[101] David S Eisenberg and Michael R Sawaya. Structural studies of amyloid proteins at the molecular level. *Annual review of biochemistry*, 86:69–95, 2017.

[102] Morten S Dueholm, Mads Albertsen, Daniel Otzen, and Per Halkjær Nielsen. Curli functional amyloid systems are phylogenetically widespread and display large diversity in operon and protein structure. *PloS one*, 7(12):e51274, 2012.

[103] Arne Olsén, Anna Jonsson, and Staffan Normark. Fibronectin binding mediated by a novel class of surface organelles on escherichia coll. *Nature*, 338(6217):652–655, 1989.

[104] Kelly Schwartz and Blaise R Boles. Microbial amyloids–functions and interactions within the host. *Current opinion in microbiology*, 16(1):93–99, 2013.

[105] Kelly Schwartz, Matthew D Sekedat, Adnan K Syed, Brendan O'Hara, David E Payne, Abigail Lamb, and Blaise R Boles. The agrd n-terminal leader peptide of staphylococcus aureus has cytolytic and amyloidogenic properties. *Infection and immunity*, 82(9):3837–3844, 2014.

[106] Adnan K Syed and Blaise R Boles. Fold modulating function: bacterial toxins to functional amyloids. *Frontiers in microbiology*, 5:401, 2014.

[107] Martín Carballo-Pacheco and Birgit Strodel. Advances in the simulation of protein aggregation at the atomistic scale. *The journal of physical chemistry B*, 120(12):2991–2999, 2016.

[108] Alex Morriss-Andrews and Joan-Emma Shea. Computational studies of protein aggregation: methods and applications. *Annual review of physical chemistry*, 66:643–666, 2015.

[109] James C. Stroud, Cong Liu, Poh K. Teng, and David Eisenberg. Toxic fibrillar oligomers of amyloid-β have cross-β structure. *Proceedings of the National Academy of Sciences of the United States of America*, 109(20):7717–7722, may 2012.

[110] Keh-Ming Pan, Michael Baldwin, Jack Nguyen, Maria Gasset, ANA Serban, Darlene Groth, Ingrid Mehlhorn, Ziwei Huang, Robert J Fletterick, and Fred E Cohen. Conversion of alpha-helices into beta-sheets features in the formation of the scrapie prion proteins. *Proceedings of the National Academy of Sciences*, 90(23):10962–10966, 1993.

[111] EP DeBenedictis, D Ma, and Sinan Keten. Structural predictions for curli amyloid fibril subunits csga and csgb. *RSC advances*, 7(76):48102–48112, 2017.

[112] Maria Andreasen, Georg Meisl, Jonathan D Taylor, Thomas CT Michaels, Aviad Levin, Daniel E Otzen, Matthew R Chapman, Christopher M Dobson, Steve J Matthews, and Tuomas PJ Knowles. Physical determinants of amyloid assembly in biofilm formation. *Mbio*, 10(1):e02279–18, 2019.

[113] Martha Dunbar, Elizabeth DeBenedictis, and Sinan Keten. Dimerization energetics of curli fiber subunits csga and csgb. *npj Computational Materials*, 5(1):1–9, 2019.

[114] Jessica Nasica-Labouze, Phuong H Nguyen, Fabio Sterpone, Olivia Berthoumieu, Nicolae-Viorel Buchete, Sebastien Cote, Alfonso De Simone, Andrew J Doig, Peter Faller, Angel Garcia, Alessandro Laio, Mai Suan Li, Simone Melchionna, Normand Mousseau, Yuguang Mu, Anant Paravatsu, Samuela Pasquali, David J Rosenman, Birgit Strodel, Bogdan Tarus, John H Viles, Tong Zhang, Chunyu Wang, and Phillippe Derreumaux. Amyloid β protein and alzheimer's disease: When computer simulations complement experimental studies. *Chemical reviews*, 115(9):3518–3563, 2015.

[115] Minjeong Cha, Emine Sumeyra Turali Emre, Xiongye Xiao, Ji-Young Kim, Paul Bogdan, J Scott VanEpps, Angela Violi, and Nicholas A Kotov. Unifying structural descriptors for biological and bioinspired nanoscale complexes. *Nature Computational Science*, 2(4):243–252, 2022.

[116] Shuai Gong, Jingjing Liu, Mengting Tian, Kang Wang, Shali Cai, Weiyan Wang, Lei Shen, Rsc Li, / Chemcomm, and Chemcomm Communication. Unravelling the mechanism of amyloid-b peptide oligomerization and fibrillation at chiral interfaces †. *Chem. Commun*, 55:13725–13728, 2019.

[117] Wojciech Dzwolak. Chirality and chiroptical properties of amyloid fibrils. *Chirality*, 26(9):580–587, 2014.

[118] Noa Rubin, Emanuel Perugia, Michal Goldschmidt, Mati Fridkin, and Lia Addadi. Chirality of amyloid suprastructures. *Journal of the American Chemical Society*, 130(14):4602–4603, 2008.

[119] Dmitry Kurouski, Xuefang Lu, Ludmila Popova, William Wan, Maruda Shanmugasundaram, Gerald Stubbs, Rina K Dukor, Igor K Lednev, and Laurence A Nafie. Is Supramolecular Filament Chirality the Underlying Cause of Major Morphology Differences in Amyloid Fibrils? *Journal of the American Chemical Society*, 2014.

[120] Shuai Zhang, Maria Andreasen, Jakob T Nielsen, Lei Liu, Erik H Nielsen, Jie Song, Gang Ji, Fei Sun, Troels Skrydstrup, Flemming Besenbacher, Niels C Nielsen, Daniel E Otzen, and Mingdong Dong. Coexistence of ribbon and helical fibrils originating from hiapp20–29 revealed by quantitative nanomechanical atomic force microscopy. *Proceedings of the National Academy of Sciences*, 110(8):2798–2803, 2013.

[121] Changjiang Liu, Paolo Elvati, and Angela Violi. On Drug-Membrane Permeability of Antivirals for SARS-CoV-2. *The Journal of Physical Chemistry Letters*, 12(5):1384–1389, 2021.

[122] MC Rheinstädter, C Ollinger, G Fragneto, F Demmel, and T Salditt. Collective dynamics of lipid membranes studied by inelastic neutron scattering. *Physical Review Letters*, 93(10):108107, 2004.

[123] Clare L Armstrong, Matthew A Barrett, Arno Hiess, Tim Salditt, John Katsaras, An-Chang Shi, and Maikel C Rheinstädter. Effect of cholesterol on the lateral nanoscale dynamics of fluid membranes. *European Biophysics Journal*, 41(10):901–913, 2012.

[124] NV Surovtsev and SV Adichtchev. Dynamic response on a nanometer scale of binary phospholipid-cholesterol vesicles: Low-frequency raman scattering insight. *Physical Review E*, 104(5):054406, 2021.

[125] Samuel L Foley, Amirali Hossein, and Markus Deserno. Fluid-gel coexistence in lipid membranes under differential stress. *Biophysical Journal*, 121(16):2997–3009, 2022.

[126] Helena Rosado, Robert D. Turner, Simon J. Foster, and Peter W. Taylor. Impact of the β-Lactam resistance modifier (-)-epicatechin gallate on the non-random distribution of phospholipids across the cytoplasmic membrane of staphylococcus aureus. *International Journal of Molecular Sciences*, 16(8):16710–16727, 2015.

[127] Tiffanny Jones, Michael R. Yeaman, George Sakoulas, Soo Jin Yang, Richard A. Proctor, Hans Georg Sahl, Jacques Schrenzel, Yan Q. Xiong, and Arnold S. Bayer. Failures in clinical treatment of Staphylococcus aureus infection with daptomycin are associated with alterations in surface charge, membrane phospholipid asymmetry, and drug binding. *Antimicrobial Agents and Chemotherapy*, 52(1):269–278, 2008.

[128] Tahsina Shireen, Madhuri Singh, Tiyasa Das, and Kasturi Mukhopadhyay. Differential adaptive responses of Staphylococcus aureus to in vitro selection with different antimicrobial peptides. *Antimicrobial Agents and Chemotherapy*, 57(10):5134–5137, 2013.

[129] INGEBURG Horbach, DIETER Naumann, and FRANZ J Fehrenbach. Simultaneous infections with different serogroups of legionella pneumophila investigated by routine methods and fourier transform infrared spectroscopy. *Journal of Clinical Microbiology*, 26(6):1106–1110, 1988.

[130] Dieter Naumann, Dieter Helm, and Harald Labischinski. Microbiological characterizations by ft-ir spectroscopy. *Nature*, 351(6321):81–82, 1991.

[131] MC Curk, F Peledan, and JC Hubert. Fourier transform infrared (ftir) spectroscopy for identifying lactobacillus species. *FEMS microbiology letters*, 123(3):241–248, 1994.

[132] D Helm, H Labischinski, Gisela Schallehn, and D Naumann. Classification and identification of bacteria by fourier-transform infrared spectroscopy. *Microbiology*, 137(1):69–79, 1991.

[133] D Naumann, V Fijala, H Labischinski, and P Giesbrecht. The rapid differentiation and identification of pathogenic bacteria using fourier transform infrared spectroscopic and multivariate statistical analysis. *Journal of Molecular Structure*, 174:165–170, 1988.

[134] LC Thomas and JES Greenstreet. The identification of micro-organisms by infrared spectrophotometry. *Spectrochimica Acta*, 6(4):302–319, 1954.

[135] Bernard A Kenner, Jackson W Riddle, Sue W Rockwood, and Robert H Bordner. Bacterial identification by infrared spectrophotometry ii: Effect of instrumental and environmental variables. *Journal of Bacteriology*, 75(1):16–20, 1958.

[136] Audrey Berrier, Martijn C Schaafsma, Guillaume Nonglaton, Jonas Bergquist, and Jaime Gómez Rivas. Selective detection of bacterial layers with terahertz plasmonic antennas. *Biomedical optics express*, 3(11):2937–2949, 2012.

[137] SA Yoon, SH Cha, SW Jun, SJ Park, J-Y Park, S Lee, HS Kim, and YH Ahn. Identifying different types of microorganisms with terahertz spectroscopy. *Biomedical Optics Express*, 11(1):406–416, 2020.

[138] Navid Barani and Kamal Sarabandi. Electromagnetic signaling and quorum sensing within biofilms: Which mechanism is the most probable means of communication? In *2020 42nd Annual International Conference of the IEEE Engineering in Medicine & Biology Society (EMBC)*, pages 2459–2462. IEEE, 2020.

[139] Navid Barani, Kamal Sarabandi, Nicholas A Kotov, J Scott Vanepps, Paolo Elvati, Yichun Wang, and Angela Violi. A multiphysics modeling of electromagnetic signaling phenomena at khz-ghz frequencies in bacterial biofilms. *IEEE Access*, 10:39344–39361, 2022.

[140] Navid Barani, Mani Kashanianfard, and Kamal Sarabandi. A mechanical antenna with frequency multiplication and phase modulation capability. *IEEE Transactions on Antennas and Propagation*, 69(7):3726–3739, 2020.

[141] David A Turton, Hans Martin Senn, Thomas Harwood, Adrian J Lapthorn, Elizabeth M Ellis, and Klaas Wynne. Terahertz underdamped vibrational motion governs protein-ligand binding in solution. *Nature communications*, 5(1):1–6, 2014.

[142] Jing Xu, Kevin W Plaxco, and S James Allen. Probing the collective vibrational dynamics of a protein in liquid water by terahertz absorption spectroscopy. *protein Science*, 15(5):1175–1181, 2006.

[143] Won Jin Choi, Gong Cheng, Zhengyu Huang, Shuai Zhang, Theodore B Norris, and Nicholas A Kotov. Terahertz circular dichroism spectroscopy of biomaterials enabled by kirigami polarization modulators. *Nature materials*, 18(8):820–826, 2019.

[144] Thomas J Piggot, Daniel A Holdbrook, and Syma Khalid. Electroporation of the e. coli and s. aureus membranes: molecular dynamics simulations of complex bacterial membranes. *The journal of physical chemistry B*, 115(45):13381–13388, 2011.

[145] Erik G Brandt, Anthony R Braun, Jonathan N Sachs, John F Nagle, and Olle Edholm. Interpretation of fluctuation spectra in lipid bilayer simulations. *Biophysical journal*, 100(9):2104–2111, 2011.

[146] Anthony R Braun, Erik G Brandt, Olle Edholm, John F Nagle, and Jonathan N Sachs. Determination of electron density profiles and area from simulations of undulating membranes. *Biophysical journal*, 100(9):2112–2120, 2011.

[147] ES Boek, JT Padding, Wouter K den Otter, and Willem J Briels. Mechanical properties of surfactant bilayer membranes from atomistic and coarse-grained molecular dynamics simulations. *The Journal of Physical Chemistry B*, 109(42):19851–19858, 2005.

[148] J Stecki. Variation of lateral tension and a new transition in model bilayers made of chain molecules. *The Journal of chemical physics*, 122(11):111102, 2005.

[149] J Stecki. Note: On the power spectrum of undulations of simulated bilayers. *The Journal of Chemical Physics*, 137(11):116102, 2012.

[150] J Stecki. Correlations in simulated model bilayers. *The Journal of chemical physics*, 120(7):3508–3516, 2004.

[151] Bartosz Różycki and Reinhard Lipowsky. Spontaneous curvature of bilayer membranes from molecular simulations: Asymmetric lipid densities and asymmetric adsorption. *The Journal of chemical physics*, 142(5):02B601_1, 2015.

[152] Chao Yang, Zengyou He, and Weichuan Yu. Comparison of public peak detection algorithms for maldi mass spectrometry data analysis. *BMC bioinformatics*, 10(1):1–13, 2009.

[153] Alan H Lipkus, Krishnan K Chittur, Stephen J Vesper, Jayne B Robinson, and George E Pierce. Evaluation of infrared spectroscopy as a bacterial identification method. *Journal of industrial microbiology*, 6(1):71–75, 1990.

[154] Dieter Helm, Harald Labischinski, and Dieter Naumann. Elaboration of a procedure for identification of bacteria using fourier-transform ir spectral libraries: a stepwise correlation approach. *Journal of microbiological methods*, 14(2):127–142, 1991.

[155] Dieter Naumann. The ultra rapid differentiation and identification of pathogenic bacteria using ft-ir techniques. In *Fourier and computerized infrared spectroscopy*, volume 553, pages 268–269. SPIE, 1985.

[156] Susanne E Horvath and Günther Daum. Lipids of mitochondria. *Progress in lipid research*, 52(4):590–614, 2013.

[157] David J Gonzalez, Nina M Haste, Andrew Hollands, Tinya C Fleming, Matthew Hamby, Kit Pogliano, Victor Nizet, and Pieter C Dorrestein. Microbial competition between bacillus subtilis and staphylococcus aureus monitored by imaging mass spectrometry. *Microbiology*, 157(Pt 9):2485, 2011.

[158] Reg P. Rehal, Helene Marbach, Alasdair T.M. Hubbard, Anam A. Sacranie, Federica Sebastiani, Giovanna Fragneto, and Richard D. Harvey. The influence of mild acidity on lysyl-phosphatidylglycerol biosynthesis and lipid membrane physico-chemical properties in methicillin-resistant Staphylococcus aureus. *Chemistry and Physics of Lipids*, 206:60–70, 2017.

[159] WF Drew Bennett, Stephen J Fox, Delin Sun, and C Mark Maupin. Bacterial membranes are more perturbed by the asymmetric versus symmetric loading of amphiphilic molecules. *Membranes*, 12(4):350, 2022.

[160] David C White and Frank E Frerman. Fatty acid composition of the complex lipids of staphylococcus aureus during the formation of the membrane-bound electron transport system. *Journal of bacteriology*, 95(6):2198–2209, 1968.

[161] CWM Haest, J De Gier, JAF Op Den Kamp, P Bartels, and LLM Van Deenen. Changes in permeability of staphylococcus aureus and derived liposomes with varying lipid composition. *Biochimica et Biophysica Acta (BBA)-Biomembranes*, 255(3):720–733, 1972.

[162] Robert M Gould and WJ Lennarz. Metabolism of phosphatidylglycerol and lysyl phosphatidylglycerol in staphylococcus aureus. *Journal of Bacteriology*, 104(3):1135–1144, 1970.

[163] Sarah Witzke, Michael Petersen, Timothy S Carpenter, and Syma Khalid. Molecular dynamics simulations reveal the conformational flexibility of lipid ii and its loose association with the defensin plectasin in the staphylococcus aureus membrane. *Biochemistry*, 55(23):3303–3314, 2016.

[164] Masaaki Hayami, Akinobu Okabe, Reiko Kariyama, Masufumi Abe, and Yasuhiro Kanemasa. Lipid composition of staphylococcus aureus and its derived l-forms. *Microbiology and immunology*, 23(6):435–442, 1979.

[165] Yuanyuan Xu, Baoping Zhang, Li Wang, Tao Jing, Jing Chen, Xiaogang Xu, Wenhong Zhang, Ying Zhang, and Jian Han. Unusual features and molecular pathways of Staphylococcus aureus L-form bacteria. *Microbial Pathogenesis*, 140(199):103970, 2020.

[166] Yayoi Nishiyama and Hideyo Yamaguchi. Morphological Detection of Filipin-Sterol Complexes in the Cytoplasmic Membrane of Staphylococcal L-Form. *MICROBIOLOGY and IMMUNOLOGY*, 34(1):25–34, 1990.

[167] Erick J Dufourc. Sterols and membrane dynamics. *Journal of chemical biology*, 1(1):63–77, 2008.

[168] Tiffanny Jones, Michael R Yeaman, George Sakoulas, Soo-Jin Yang, Richard A Proctor, Hans-Georg Sahl, Jacques Schrenzel, Yan Q Xiong, and Arnold S Bayer. Failures in clinical treatment of staphylococcus aureus infection with daptomycin are associated with alterations in surface charge, membrane phospholipid asymmetry, and drug binding. *Antimicrobial agents and chemotherapy*, 52(1):269–278, 2008.

[169] Erin Kilelee, Antje Pokorny, Michael R Yeaman, and Arnold S Bayer. Lysylphosphatidylglycerol attenuates membrane perturbation rather than surface association of the cationic antimicrobial peptide 6w-rp-1 in a model membrane system: implications for daptomycin resistance. *Antimicrobial agents and chemotherapy*, 54(10):4476–4479, 2010.

[170] James A Wepy, James J Galligan, Philip J Kingsley, Shu Xu, Michael C Goodman, Keri A Tallman, Carol A Rouzer, and Lawrence J Marnett. Lysophospholipases cooperate to mediate lipid homeostasis and lysophospholipid signaling [s]. *Journal of lipid research*, 60(2):360–374, 2019.

[171] William J Brown, Kimberly Chambers, and Anne Doody. Phospholipase a2 (pla2) enzymes in membrane trafficking: mediators of membrane shape and function. *Traffic*, 4(4):214–221, 2003.

[172] Anna Grzelczyk and Edyta Gendaszewska-Darmach. Novel bioactive glycerol-based lysophospholipids: new data–new insight into their function. *Biochimie*, 95(4):667–679, 2013.

[173] Wei Xu, Fong-Fu Hsu, Eda Baykal, Juyang Huang, and Kai Zhang. Sterol biosynthesis is required for heat resistance but not extracellular survival in leishmania. *PLoS pathogens*, 10(10), 2014.

[174] Alasdair T.M. Hubbard, Robert Barker, Reg Rehal, Kalliopi Kelli A. Vandera, Richard D. Harvey, and Anthony R.M. Coates. Mechanism of Action of a Membrane-Active Quinoline-Based Antimicrobial on Natural and Model Bacterial Membranes. *Biochemistry*, 56(8):1163–1174, 2017.

[175] Stephanie Fulaz, Henry Devlin, Stefania Vitale, Laura Quinn, James P O'Gara, and Eoin Casey. Tailoring nanoparticle-biofilm interactions to increase the efficacy of antimicrobial agents against staphylococcus aureus. *International journal of nanomedicine*, pages 4779–4791, 2020.

[176] Joanne K Beckwith, J Scott VanEpps, and Michael J Solomon. Differential effects of heated perfusate on morphology, viability, and dissemination of staphylococcus epidermidis biofilms. *Applied and Environmental Microbiology*, 86(20):e01193–20, 2020.

[177] Luanne Hall-Stoodley, J William Costerton, and Paul Stoodley. Bacterial biofilms: from the natural environment to infectious diseases. *Nature reviews microbiology*, 2(2):95–108, 2004.

[178] Philip S Stewart. Mechanisms of antibiotic resistance in bacterial biofilms. *International journal of medical microbiology*, 292(2):107–113, 2002.

[179] Bui Thi Hoan, Phuong Dinh Tam, Vuong-Hung Pham, et al. Green synthesis of highly luminescent carbon quantum dots from lemon juice. *Journal of Nanotechnology*, 2019, 2019.

[180] Seokhwan Chung, Richard A Revia, and Miqin Zhang. Graphene quantum dots and their applications in bioimaging, biosensing, and therapy. *Advanced Materials*, 33(22):1904362, 2021.

[181] Fei Chen, Weiyin Gao, Xiaopei Qiu, Hong Zhang, Lianhua Liu, Pu Liao, Weiling Fu, and Yang Luo. Graphene quantum dots in biomedical applications: recent advances and future challenges. *Frontiers in Laboratory Medicine*, 1(4):192–199, 2017.

[182] Nan Zhang, Ling Zhang, Yi-Fan Ruan, Wei-Wei Zhao, Jing-Juan Xu, and Hong-Yuan Chen. Quantum-dots-based photoelectrochemical bioanalysis highlighted with recent examples. *Biosensors and Bioelectronics*, 94:207–218, 2017.

[183] Liang-shi Li and Xin Yan. Colloidal graphene quantum dots. *The Journal of Physical Chemistry Letters*, 1(17):2572–2576, 2010.

[184] Gundam Sandeep Kumar, Umamahesh Thupakula, Piyush Kanti Sarkar, and Somobrata Acharya. Easy extraction of water-soluble graphene quantum dots for light emitting diodes. *Rsc Advances*, 5(35):27711–27716, 2015.

[185] Xu Wu, Fei Tian, Wenxue Wang, Jiao Chen, Min Wu, and Julia Xiaojun Zhao. Fabrication of highly fluorescent graphene quantum dots using l-glutamic acid for in vitro/in vivo imaging and sensing. *Journal of Materials Chemistry C*, 1(31):4676–4684, 2013.

[186] Zhiping Zeng, Shufen Chen, Timothy Thatt Yang Tan, and Fang-Xing Xiao. Graphene quantum dots (gqds) and its derivatives for multifarious photocatalysis and photoelectrocatalysis. *Catalysis Today*, 315:171–183, 2018.

[187] Hassan Y Aboul-Enein and Imran Ali. Chiral resolution of cromakalim by hplc on teicoplanin and teicoplanin aglycon chiral stationary phases. *Journal of liquid chromatography & related technologies*, 25(13-15):2337–2344, 2002.

[188] Alain Berthod. Chiral recognition mechanisms with macrocyclic glycopeptide selectors. *Chirality: The Pharmacological, Biological, and Chemical Consequences of Molecular Asymmetry*, 21(1):167–175, 2009.

[189] JE Claus. Chiral hplc analysis of underivatized amino acid enantiomers. *Reporter*, 29:8–9, 2011.

[190] Yumeng Yan, Huanyu Tao, Jiahua He, and Sheng-You Huang. The hdock server for integrated protein–protein docking. *Nature protocols*, 15(5):1829–1852, 2020.

[191] Mehrnaz Azami-Movahed, Ali Akbar Meratan, Atiyeh Ghasemi, Azadeh Ebrahim-Habibi, and Mohsen Nemat-Gorgani. Acetylation of lysine residues in apomyoglobin: Structural changes, amyloid fibrillation, and role of surface charge. *International journal of biological macromolecules*, 107:626–634, 2018.

[192] Cristina Azevedo and Adolfo Saiardi. Why always lysine? the ongoing tale of one of the most modified amino acids. *Advances in biological regulation*, 60:144–150, 2016.

[193] Matthew W Fields, Paul Sturman, and Skip Anderson. The establishment of the cbe launched biofilms as a field of specialized research. *Biofilm*, 2:100020, 2020.

[194] John J Karnes, Eric A Gobrogge, Robert A Walker, and Ilan Benjamin. Unusual structure and dynamics at silica/methanol and silica/ethanol interfaces: A molecular dynamics and nonlinear optical study. *The Journal of Physical Chemistry B*, 120(8):1569–1578, 2016.

[195] Carlos Escudero and Miquel Salmeron. From solid–vacuum to solid–gas and solid–liquid interfaces: In situ studies of structure and dynamics under relevant conditions. *Surface science*, 607:2–9, 2013.

[196] Jacob Saldinger, Matt Raymond, Paolo Elvati, and Angela Violi. From proteins to nanoparticles: domain-agnostic predictions of nanoscale interactions. *bioRxiv*, pages 2022–08, 2022.

[197] Matthew J McGuffie, Jin Hong, Joong Hwan Bahng, Emmanouil Glynos, Peter F Green, Nicholas A Kotov, John G Younger, and J Scott VanEpps. Zinc oxide nanoparticle suspensions and layer-by-layer coatings inhibit staphylococcal growth. *Nanomedicine: Nanotechnology, Biology and Medicine*, 12(1):33–42, 2016.

[198] Usha Kadiyala, Emine Sumeyra Turali-Emre, Joong Hwan Bahng, Nicholas A Kotov, and J Scott VanEpps. Unexpected insights into antibacterial activity of zinc oxide nanoparticles against methicillin resistant staphylococcus aureus (mrsa). *Nanoscale*, 10(10):4927–4939, 2018.

[199] Xiaohui Zhao, Hao Tang, and Xingyu Jiang. Deploying gold nanomaterials in combating multi-drug-resistant bacteria. *ACS nano*, 16(7):10066–10087, 2022.

[200] Kaiyuan Zheng, Magdiel I Setyawati, David Tai Leong, and Jianping Xie. Antimicrobial gold nanoclusters. *ACS nano*, 11(7):6904–6910, 2017.

[201] Shuaidong Huo, Ying Jiang, Akash Gupta, Ziwen Jiang, Ryan F Landis, Singyuk Hou, Xing-Jie Liang, and Vincent M Rotello. Fully zwitterionic nanoparticle antimicrobial agents through tuning of core size and ligand structure. *ACS nano*, 10(9):8732–8737, 2016.

[202] Amjed Alabresm, Alan W Decho, and Jamie Lead. A novel method to estimate cellular internalization of nanoparticles into gram-negative bacteria: Non-lytic removal of outer membrane and cell wall. *Nanoimpact*, 21:100283, 2021.

[203] Irit Levin-Reisman, Irine Ronin, Orit Gefen, Ilan Braniss, Noam Shoresh, and Nathalie Q Balaban. Antibiotic tolerance facilitates the evolution of resistance. *Science*, 355(6327):826–830, 2017.

[204] Irit Levin-Reisman, Asher Brauner, Irine Ronin, and Nathalie Q Balaban. Epistasis between antibiotic tolerance, persistence, and resistance mutations. *Proceedings of the National Academy of Sciences*, 116(29):14734–14739, 2019.

[205] Theresa C Barrett, Wendy WK Mok, Allison M Murawski, and Mark P Brynildsen. Enhanced antibiotic resistance development from fluoroquinolone persisters after a single exposure to antibiotic. *Nature communications*, 10(1):1177, 2019.

[206] Etthel Martha Windels, Joran Elie Michiels, Maarten Fauvart, Tom Wenseleers, Bram Van den Bergh, and Jan Michiels. Bacterial persistence promotes the evolution of antibiotic resistance by increasing survival and mutation rates. *The ISME journal*, 13(5):1239–1251, 2019.